

LIBRARY Michigan State University

This is to certify that the

dissertation entitled

A THYRATRON - CONTROLLEY, HICH VOLTAGE
SPARK ATOMIC EMISSION DETECTOR FOR
CAPILLARY GAS CHROMATOG RAPHY

presented by

KEITH KENNETH TRISCHAM

has been accepted towards fulfillment of the requirements for

Ph.D. degree in CHEMISTRY

Major prof

Date 11/19/84



RETURNING MATERIALS:
Place in book drop to remove this checkout from your record. FINES will be charged if book is returned after the date stamped below.

A THYRATRON-CONTROLLED, HIGH VOLTAGE SPARK ATOMIC EMISSION DETECTOR FOR CAPILLARY GAS CHROMATOGRAPHY

By

Keith Kenneth Trischan

A THESIS

Submitted to
Michigan State University
in partial fulfillment of the requirements
for the degree of

DOCTOR OF PHILOSOPHY

Department of Chemistry

1984

ABSTRACT

A THYRATRON-CONTROLLED, HIGH VOLTAGE SPARK ATOMIC EMISSION DETECTOR FOR CAPILLARY GAS CHROMATOGRAPHY

Bv

Keith Kenneth Trischan

The construction of a high voltage, dc, nanosecond spark source for analysis described. The atomic emission is source is used for element-selective detection of capillary gas chromatographic effluents. In operation, a high power spark discharge is formed in an argon atmosphere between two thoriated tungsten electrodes by the discharge of a coaxial capacitor. A ceramic, hydrogen thyratron is used to trigger the discharge. This establishes a highly reproducible firing rate. Effluents from a capillary gas chromatograph are transferred through a heated glass interface to the spark where atomization and excitation of the eluted compounds occurs. A microcomputer-controlled data acquisition system allows the acquisition of time-resolved emission intensities. With this method, intense continuum radiation, generated when the discharge is formed, is discriminated against in favor of relevant atomic emissions. Improved signal-to-noise ratios are obtained by acquisition of computer-averaged intensities for several consecutive sparks. A menu-driven software package is described which simplifies the data acquisition process. Characterization studies of the thyratron-controlled spark source are described. The entire detection system is applied to universal and element-selective detection of capillary gas chromatographic effluents.

To my wife, Anna, parents, and brother

ACKNOWLEDGEMENTS

Many people deserve more thanks than I could ever give. Most of all, I wish to thank my wife for all the support, moral and financial, which she has given me. Without her typing assistance this work would be as hard to read as my handwriting.

I also thank my parents and brother for their assistance in this endeavor.

They have always impressed me with the idea that nothing is impossible if you try your hardest and if you persevere.

Dr. Stan Crouch deserves a fair share of the credit for this as well. He has allowed me to develop along paths that I found interesting and which otherwise would have remained unexplored while he still provided direction when needed.

Many thanks to the members of my research group who have always insured that work was full of unexpected surprises. They have made my stay here much more enjoyable than it otherwise would have been. I would like to especially thank Marquerite who has proven that the size of the heart is definitely not proportional to the size of the person.

Finally, I would like to thank the excellent technicians, machinists, and specialist in the department who have helped solve problems which I could not overcome on my own.

TABLE OF CONTENTS

		PAGE	
LIST OF	TABLES	vii	
LIST OF	FIGURES	viii	
СНАРТІ	ER I - INTRODUCTION	1	
СНАРТІ	ER II - ELEMENT-SELECTIVE GAS	4	
	CHROMATOGRAPHIC DETECTORS		
Α.	Introduction	4	
В.	Thermionic Detector	5	
c.	Flame Photometric Detector	6	
D.	Electron Capture Detector	8	
Е.	Atomic Absorption Detector	9	
F.	F. Atomic Emission Detectors		
	1. Microwave Induced Plasma Detector	10	
	2. Direct Current Plasma Detector	12	
	3. Inductively Coupled Plasma Detector	13	
	4. Spark Discharge Detector	13	
CHAPTI	ER III - INSTRUMENTATION	15	
Α.	Overview of the Spark Atomic Emission System	16	
В.	B. Spark Source Design		
C.	Thyratron Controlled Spark Source	23	

			PAGE
]	D.	Capillary Gas Chromatograph - Spark Interface	24
1	Ε.	Solution Introduction System	27
]	F.	Gas Chromatographic Components	32
(G.	Alternate Spark Imaging Scheme	35
СНА	PTI	ER IV - ELECTRONICS AND OPERATION	37
1	A.	The Intel 8085 Based Microcomputer	37
I	В.	3. Minicomputer Facilities	
(c.	Data Acquisition Electronics	42
		1. Device Selection Circuitry	42
		2. Data Acquisition Timing Circuitry	45
		3. Analog Electronics	53
		a. Gated Integrator	53
		b. Baseline Subtraction Circuitry	55
		c. Programmable Gain Amplifier	55
		d. Analog-to-Digital Converter Circuitry	56
		4. Photomultiplier Gate Circuitry	57
I	D.	Monochromator Controller/Microcomputer Interface	59
I	Е.	Spark Detection Circuitry	65
CHA	PTE	ER V - SOFTWARE	67
A	A.	Data Acquisition Software	69
F	В.	Interrupt Service Routine	73
(c.	Buffer Management Routine	74
I	D.	Data Storage Routine	77
F	Ε.	Data Disk Organization	77
I	F.	Minicomputer Programming Language Selection	79
		1. CVT - Data Conversion Software	81

		PAGE
СНАРТ	ER VI - SPARK SOURCE CHARACTERIZATION	83
Α.	Capacitor Charging Characteristics	85
В.	Effect of Gap Voltage on Current Waveform	90
c.	Background Emission Studies	93
D.	Effect of Oxygen on Carbon Emission	99
Ε.	Excitation Temperature Studies	99
F.	Effect of Time on Excitation Temperature	102
G.	Effect of Charging Voltage on Excitation Temperature	102
н.	Electron Density Measurements	108
I.	Determination of Ionization Temperature	110
СНАРТ	ER VII - CHROMATOGRAPHIC EVALUATION	116
Α.	Introduction	116
В.	Evaluation of the GC - Spark Interface	117
c.	Universal GC Detection Capabilties	121
D.	Element-Selective Detection of Lead in Gasoline	127
	1. Lead Calibration Curve	128
	2. Lead Determination in Gasoline	131
СНАРТ	ER VIII - CONCLUSIONS AND PERSPECTIVES	134
REFER	ENCES	139

LIST OF TABLES

TABLE		PAGE
4-1	Monochromator Controller Commands	63
5-1	Data Acquisition Options	71
6-1	Typical Acquisition Parameters	94
6-2	Argon Line Emission Parameters	104
7-1	Jet Fuel Gas Chromatographic Conditions	120
7-2	Carbon Standards Gas Chromatographic Conditions	123
7-3	Lead Standards Gas Chromatographic Conditions	129

LIST OF FIGURES

FIGURE		PAGE
3-1	Block Diagram of the NSS-GC System	17
3-2	The NSS Housing	19
3-3	The Analytical Chamber, expanded view	21
3-4	Circuit Diagram of Thyratron-Controlled Spark Source	25
3-5	GC - Spark Interface	26
3-6	Ultrasonic Nebulizer	29
3-7	Cross-Flow Nebulizer	30
3-8	Miniaturized Desolvation Chamber	31
3-9	Capillary GC Injector	33
3-10	Alternate Lensing Scheme	36
4-1	Block Diagram of Data Acquisition Electronics	38
4-2	Block Diagram of Intel 8085 Microcomputer System	39
4-3	Interface Device-Selection Circuit	44
4-4	Block Diagram of Advanced Micro Devices AM9513	46
	Timing Controller	
4-5	Block Diagram of AM9513 Counter Group	48
4-6	Timer Circuit	51
4-7	Analog Electronics	54

FIGURE		PAGE
4-8	Photomultiplier Gate Circuit	58
4-9	Microcomputer/Monochromator Interface	60
4-10	Photodiode Trigger Circuit	66
5-1	Data Acquisition Software Organization	70
5-2	Flow Chart for Interrupt Service Routine	75
5-3	Flow Chart for Buffer Management Routine	76
5-4	Flow Chart for Buffer Flushing Routine	78
6-1	Gap Voltage as a Function of Repetition Rate	87
6-2	Relative Intensity as a Function of	
	Repetition Rate	88
6-3	Relative Intensity as a Function of Charging Voltage	89
6-4	Discharge Current as a Function of Charging Voltage.	91
6-5	Maximum Discharge Current as a Function	
	of Charging Voltage	92
6-6	Background Emission as a Function of	
	Wavelength (0.3 - 1.0 μs delay time)	95
6-7	Background Emission as a Function of	
	Wavelength (2.0 - 4.0 μs delay time)	96
6-8	Relative Carbon Emission Intensity as a	
	Function of Oxygen Flow Rate	100
6-9	Spectrum of Neutral Argon Emission Lines	103
6-10	Excitation Temperature Slope Plot	105
6-11	Excitation Temperature as a Function of	
	Delay Time	106
6-12	Excitation Temperature as a Function of	
	Charging Voltage	107
6-13	Stark Broadened H _B Line Profile	109

FIGURE		PAGE
6-14	Electron Density as a Function of Delay Time	111
6-15	Calcium Emission as a Function of Delay Time	112
6-16	Ionization Temperature as a Function of	
	Delay Time	114
7-1	Comparison of FID and NSS Detection	119
7-2	n-alkane Chromatogram	124
7-3	Carbon Calibration Curve	125
7-4	Chromatographic Peak Digitization Errors	126
7-5	Lead Standard Chromatogram	130
7-6	Lead Calibration Curve	132

CHAPTER I

INTRODUCTION

Chemists are being required to perform analyses of samples in extremely complex matrices. The main forces behind this demand are the determination of trace level components which impart either a beneficial or a hazardous critical characteristic to the sample. Often such a critical component will contain a functionality or element such as bromine, lead, or other heavy metals which is contained in only a small fraction of the compounds in the sample. When this is true, a detection method which responds only to the critical feature will greatly simplify the identification and quantitation of that compound.

Even when the critical component contains an identifiable, unique species, the matrix effects associated with the sample may interfere with the determination, producing inaccurate results. Both gas and liquid chromatography are quite powerful for separating complex mixtures. Because of the separation, matrix effects are eliminated except for the case of coelution or incomplete separation. The degree of separation is so high, that for complex common samples, in excess of one hundred individual peaks can be readily obtained (1). Identification of each peak is tedious and generally unnecessary since only a few critical components are of interest. Most

detectors in general use have little or no species-specificity; hence, identification of the critical compounds is by comparison of the retention times of standard mixtures to those of the sample. This requires the existence of such a standard. In addition, the chromatographic system must be stable over time, otherwise, repeated injections of the standard would be required. This could quickly become the rate limiting step in the analysis. When a selective detector is used, variations in the retention time are not critical since only the species of interest and a few similar compounds are detected; thus, a simpler chromatogram is produced.

Element-selective detectors are one group of selective detectors. Detectors based on atomic absorption or atomic emission spectroscopy offer high detectability and linearity for several metals. Detection of both metals and nonmetals can be performed with plasma sources. Since atomic carbon emission can be observed in plasmas, these detectors can be used in a universal detection mode. By tuning the observation wavelength, signals for all constituent atoms can be obtained. This allows detection of all species containing the critical element. In addition, when element-selective detection is used for gas chromatography, the empirical formulae of the individual peaks can be determined. Thus, the powerful separation capabilities of chromatography coupled with element-selective detection provides the analyst with a valuable technique.

Plasma sources are, in general, quite expensive to purchase and operate with initial costs an order of magnitude greater than that of the chromatographic system. This is prohibitive and has limited the application of plasma detectors for chromatography. A relatively inexpensive alternate atomic emission source is the nanosecond spark source.

This work describes the construction and characterization of an

electronically-triggered, high-voltage spark discharge. A description of the hardware and software used to monitor the spark and acquire emission intensity data is presented. The spark is also applied to the element-selective detection of capillary gas chromatographic effluents.

CHAPTER II

ELEMENT-SELECTIVE GAS CHROMATOGRAPHIC DETECTORS

A. Introduction

Gas chromatography has become a powerful analytical tool. Since extremely complex mixtures can be separated, identification of all detected components is extremely difficult. Choice of a detector which provides chemical information about the detected species simplifies the identification process. In addition, detection of a specific chemical property or functionality simplifies the chromatogram obtained since only compounds containing the specific characteristic are detected. A final advantage to selective detection methods is a reduction in the chromatographic quality required for a separation, since resolution of only selected components is necessary.

Element-selective chromatographic detection is one area which has received much attention recently. Several elements such as S, N, P, heavy metals, and the halogens are often associated with an environmental hazard; hence, techniques for the analysis of these elements in complex samples are required.

Element-selective detection can be achieved by atomic spectroscopic techniques or by one of several molecular methods which are drastically enhanced by the presence of one or more specific elements in the eluted

component. Atomic absorption and atomic emission techniques are popular atomic spectroscopic methods applied to GC detection. This chapter briefly reviews those element-selective detection methods which have been applied to gas chromatography; a more thorough review of this topic can be found in works of Lantz (2), Koepling (3) and Calkin (4).

Several universal detectors commonly in use demonstrate enhanced response for compounds which contain certain elements. Enhancements between 10 and 1000 are obtained for various techniques.

B. Thermionic Detector

The earliest thermionic detector was developed by Cremer (5,6). The thermionic detector is similar to the flame ionization detector except that an alkali salt crystal is mounted in the flame. In operation, the chromatographic effluent is burned in an H₂-air diffusion flame. conductivity of the flame is measured; hence, changes in the flame environment cause an increase or decrease in the conductivity of the flame. Sevcik (7) has proposed that thermal ionization of the alkali salt establishes a constant current in the flame. Current fluctuations are caused by electron capture processes, the formation of thermally stable compounds, or formation of species with high ionization potentials. Response enhancement is observed for species containing phosphorus (8,9), nitrogen (10,11,12) sulfur (13), and the halogens (14). In early TID designs, the collector electrode was at a negative potential with respect to the alkali salt. As a result, loss of alkali material was observed and the detector sensitivity decreased with use. Kolb and Bischoff (15) reversed the polarity of the collector. In this configuration, no deterioration in performance was observed with time. To account for this, a charge transfer mechanism based on the formation of radicals was developed. In this mechanism, radicals such as CN., PO., PO₂., or X. leach electrons from the alkali to form stable species. In the original design the cation was detected; hence, alkali erosion occurred. However, with polarity reversal, anion detection occurs and the cation is electrically attracted back to the salt. Thus, no erosion occurs. Recent advances indicate improved stability is attained when independent heating of the alkali material is performed. Patterson et al. has successfully designed a ceramic core with a surface coating of alkali (16). The surface coating determines the sensitivity of the detector such that a low degree of coverage and operation in an H₂/air environment demonstrates a preferential response to P and N containing compounds, while a higher coverage enhances the response to compounds containing electronegative functional groups such as nitro groups. In general, the thermionic detector has become well accepted and is not undergoing rapid technological advances as a gas chromatographic detector. Bombick et al. (17) have suggested that a thermionic emission process can be used as a tunable, selective chemical ionization media for the detection of gas chromatographic effluents by mass spectrometry.

C. Flame Photometric Detectors

Flame photometric detectors (FPD) monitor molecular emissions produced by burning the GC effluent in an $H_2/O_2/air$ flame. Molecular emissions are monitored through an optical filter with a photomultiplier. The FPD is commonly used to detect phosphorus and sulfur; however, selective detection of boron (18), nitrogen (18), chlorine (19), iodine (20), and iron (21,22) has been demonstrated. The FPD can also be operated in a universal detection mode by operation in an N_2 atmosphere (23).

One major drawback of the FPD is a nonlinear dependence of the response

on the concentration of the detected species. The most common case is for the detection of S. A rough dependence on the square of the S concentration is observed since an S₂ emission band is monitored (20). When the GC effluent is combusted in the presence of ozone, an SO₂ emission band can be observed; however, the signal obtained is not linear with S concentration (25). Nelson, et al., have obtained a fluorine-induced chemiluminescence response which is linear with the S concentration (26). Detection limits of between 24 and 260 pg/s were found for several compounds. The fluorine-induced chemiluminescence detector had no response to SO₂, COS, H₂S, and CS₂; however, the otherwise good detection limits make this an excellent tool with which to monitor other atmospheric sulfur compounds.

A similar approach has been used for the detection of iodine in iodinated hydrocarbons (20). An alternate analysis for the halogens requires observation of chemiluminescence radiation generated when polyhalogenated hydrocarbons are passed through sodium vapor (27). A number of problems were noted with the containment of the sodium vapor.

A second drawback of the FPD is that the flame occasionally extinguishes when the solvent front elutes. This has been eliminated with a two flame system (28,29). In these designs, the lower flame is used to atomize the effluent and the upper excites the residual species. Improvements in the detection limits for P, N, and S with the inclusion of a quartz sleeve around the upper burner were referenced by Karasek et al. (29).

As with the thermionic detector, the FPD has reached a level of maturity and acceptance as a reliable, well-established chromatographic detector and is used in routine analysis and applications.

D. Electron Capture Detector

The electron capture detector (ECD) is one of the most widely used, extremely sensitive detectors for routine analysis. With optimum operating conditions. detection limit of 90 was found for ag N,N-dipentafluorobenzoylpentafluoranaline (30). In operation, a beta particle emitter, typically ⁶³Ni or tritium, ionizes nitrogen molecules in the support gas and low energy electrons are formed. Application of a potential across the detector causes electron migration to the anode and the generation of a current. When an electronegative species enters the detector, some of the electrons are captured and the current decreases; thus, the detector response is a function of the mass flow of the analyte and its electronegativity. This gives a selective response to the halogen- and oxygen-containing species. Early ECD designs established a constant potential across the detection cell. Poor stability and linear range of two orders of magnitude or less were reported (31). Improvement in the stability and linear range of six orders of magnitude for the ECD have been achieved by pulsing the applied potential (32). Two mechanisms for the response of the pulsed ECD have been proposed by Aue et al. based on his experiments (33). The first mechanism is the accepted neutralization process (34) where one analyte molecule reacts with a maximum of one electron. The second mechanism is a space-charge model where a molecule sequentially combines with several electrons (35). This mechanism is summarized with the reactions:

$$RX + e^{-} \xrightarrow{k_1} R + X^{-}$$

$$X^- + P^+ \rightarrow PX + neutral$$

$$PX + e^{-} \xrightarrow{k_2} X^{-} + P$$

where R is an alkyl group, X is the electronegative species, and P^+ is a positive ion, most likely hydrogen. Reaction A is the conventional electron capture reaction. In the pulsed operating mode, several additional electrons can be neutralized by undergoing reaction C. Hence, when reaction C is kinetically and energetically favorable, an enhanced response is observed for RX.

E. Atomic Absorpbtion Detectors

Several benefits exist for selective detection by atomic spectroscopic techniques. These detectors offer high sensitivity and selectivity. In addition, selectivity for several elements is easily obtained by adjustment of the observed wavelength. Also, atomic spectroscopy has been applied to many types of analyses; hence, the application of these methods to chromatographic analysis does not require the development of an entirely new technique, but rather the extension of an existing one.

Atomic absorption is one spectroscopic technique which has been successfully adapted to chromatographic detection of metal-containing species (36-40,49). Connection of the chromatographic column to both flame and electrothermal AA detectors is trivial. Two approaches have been attempted with equal success. Wolf (39) simply drilled a hole into the side of a burner and connected the column directly to the burner. Other workers (36,37) have used a heated transfer tube as the interface. To minimize absorption of chromatographic effluents, a glass lined burner head (41) and quartz transfer tubes (42) have been developed. Detection limits at the nanogram level for Pb (39,48), Cr (39,42), Hg (40), and Se, Sn, and At (36,47) have been reported. A severe limitation to the application of AA to chromatographic detection

is the inability to determine more than one metal at a time. In addition, the need for a hollow cathode lamp for each element further limits this approach. To circumvent this limitation, Harnly et al. (43) have developed a continuum emission, wavelength-modulated AA method that can be applied to simultaneous, multielement determinations. Recently, a comparison of this method with wavelength-modulated atomic emission detection (44) presents detection limits of 0.09 ng/ml and 0.02 ng/ml, respectively for Cr in urine.

F. Atomic Emission Detectors

Atomic emission detectors are extremely powerful and are rapidly becoming the most popular element-selective detector available. When operated with a suitable light detection device, the atomic emission detector should respond to any element which the source can excite. This includes nonmetallic as well as metallic elements. Hence, atomic emission detectors can be operated in a universal mode or an element-selective mode. Several atomic emission sources have been developed and have been shown to be extremely valuable methods for chromatographic detection.

Use of polychromators for emission detection (45) allows several elements to be simultaneously monitored. This further increases the power of the technique. Atomic spectrometric detectors, particularly those using microwave induced plasma and inductively coupled plasma emission spectroscopy, have been thoroughly reviewed by Risby (46) and Qing-Yu (51).

1. Microwave Induced Plasma

Microwave induced plasma (MIP) sources have been among the most popular atomic emission detectors due to the relatively low cost, ease of operation, and high quality of response. Early MIP designs required the use of helium plasma support gas at reduced pressure (50,52,53). This made the

MIP difficult to use with the gas chromatograph; however, detection limits in the subnanogram range and a linear dynamic range of 3 to 4 orders of magnitude were reported for several elements (54,55). An atmospheric pressure argon or helium MIP was made possible with a major redesign of the resonance cavity by Beenaker (56-58). Using the atmospheric pressure MIP, the chromatographic effluent can be eluted directly into the resonance cavity (59.60).Carnahan and coworkers (61) have presented a review on chromatographic applications of plasma emission techniques and have included details of GC interfaces which have been used. Several workers have demonstrated the usefulness of sequential element-selective detection (57,62-66); however, this technique requires one injection for each element of interest. Hence, sequential detection is slow and subject to errors caused by unstable chromatographic conditions and random variations in the injection Three approaches to simultaneous multielement detection of chromatographic effluents are possible. The rapid scanning detector of Mulligan et al. (62,63) requires adequate chromatographic separation to allow multielement detection. The use of a polychromator to detect MIP emissions has received much attention (67-71). Some of these systems have the capability of detecting 20 to 30 elements simultaneously (51,62). Alternately, an array detector can be used for detection of a wavelength region containing several emission lines. One drawback of the MIP, as with other spectroscopic techniques, is the presence of molecular emissions which occur when carbon and nitrogen compounds elute. Hence, the background level changes as the peak is eluted and accurate emission intensities are difficult to obtain. This interference is particularly acute for detection of Br and Cl. Eckhoff and coworkers (71) have developed a wavelength modulated polychromator as the GC-MIP detector. Packed column detection limits of 86 pg/s and 76

pg/s were obtained for Br and Cl with this system. These compare quite well with values of 67 pg/s and 86 pg/s obtained by Estes et al. (72) with a capillary GC with monochromatic detection of the MIP emissions. A maximum acquisition rate of 3 background corrected intensities per second was obtained for each of the four available channels. While this sample rate is adequate for packed column studies, a faster acquisition rate is preferred for capillary chromatography. Holland et al. (73) suggest that a minimum of 2 and preferably 5 measurements per second be performed to ensure accurate representation of the peak. Finally, stoichiometric ratios of several elements (C, N, F, H, Cl, Br, S, and I) of the chromatographic effluents were determined with polychromatic detection of the MIP emissions (58,74,77-79).

Two disadvantages exist for the MIP. First, the plasma is sensitive to the support gas flow rate and, second, the elution of the solvent front occasionally extinguishes the plasma (80). Both problems arise from the small size of the plasma. Although these problems exist, the MIP has become popular because of its high power and relatively low cost.

2. Direct Current Plasma

The direct current plasma (DCP) source has a higher energy than the MIP; hence, the DCP is less sensitive to the carrier gas flow rate and solvent front elution. The higher energy also makes this a more sensitive atomic emission source. The DCP has been applied as a GC detector with high sensitivity for several elements (64,65,75). The development of three-electrode designs has improved the sensitivity of the source in two ways. Increased source stability has lowered random fluctuations in the location of the plasma and improved signal-to-noise ratios. Also, this design has shifted the location of the analyte emission maximum away from the intense continuum region of the plasma, further improving the sensitivity of the technique (76). Although

the DCP is a more stable and energetic plasma than the MIP, the relatively high cost of the source has limited its use as a chromatographic detector.

3. Inductively Coupled Plasma

Inductively coupled plasmas (ICP) are one of the most powerful plasma sources used for emission spectroscopy. Because of this, the ICP demonstrates superior detection limits and linearity of response. In addition, the high energy available in these sources makes them ideal for analysis of liquid samples where solvent vaporization and atomization processes consume large amounts of energy.

These plasma sources have been applied to many simultaneous, multielement detection schemes for both solution and liquid chromatographic analyses (81,82). Reports of the application of the ICP to gas chromatographic detection are sparse. Brown has successfully determined oxygen (83) and nitrogen (84) containing effluents. Lead as tetraethyl lead in fuel and air has been determined by Sommer (85) with the ICP. Detection limits at the ng Pb/s level were obtained. Detection limits of 0.05 ug with a linear range of greater than 5×10^3 have been found for Cl and Br while monitoring non-resonant emissions (86). The application of ICP detectors to gas chromatography has been limited due to the high cost of the source relative to the cost of the rest of the chromatographic system.

4. Spark Discharge Detector

Single (2) and double (3,4) gap spark discharges have been used as atomic emission sources for the detection of GC effluents. Many elements, both metals and nonmetals, have been successfully detected. Detection limits between 10^{-8} g/s and 10^{-12} g/s were achieved. Response curve linearity over two to three orders of magnitude were typical. Lantz (2) has demonstrated the capacity to determine C/H/N/O ratios for several compounds in an effluent

stream.

Band broadening caused by excessive detector dead volume has been eliminated with the incorporation of a low-volume flow cell. Although the double-gap spark source was allegedly free from affects of variations in the analytical gap environment, this was not the case. Firing rates and emission intensities were dependent on the gap environment. This degraded the analytical usefulness and made the spark source difficult to use. Although these problems existed, the spark source provided several of the desirable characteristics of more expensive atomic emission sources. Hence, the spark source remained an economical alternate plasma source which could excite many elements in an effluent stream. This work describes the construction and characterization of a high power, thyratron-triggered spark source. In addition, a microcomputer-controlled, data acquisition system for the spark source is described. Finally, the spark source is applied to the element-selective detection of capillary gas chromatographic effluents.

CHAPTER III

INSTRUMENTATION

The nanosecond spark source has evolved through several generations as a gas chromatographic element-selective detector (2-4). Spark system designs incorporating three major triggering mechanisms have been attempted. Originally, a single gap system was developed. The electrical breakdown potential and, hence, the energy dissipated in the spark were dependent on the spark environment. Since the observed signal intensity is dependent on the dissipated energy, any variation in the gap environment caused a variation in the signal intensity. The problem was particularly acute during the elution of the solvent front in gas chromatography, often completely extinguishing the spark discharge and causing difficulty in immediate reignition of the plasma. This compromised the value of the single gap system as a gas chromatographic detector.

In an attempt to alleviate the environmental dependency, a double gap system was developed. A high breakdown potential spark gap was used to control the ignition of the lower breakdown potential analytical gap. By maintaining a pure argon atmosphere in the control gap, a reproducible firing rate was to be achieved. This, in turn, was to establish a constant total discharge energy. Although the dependence of the detector on the

interelectrode enviornment was diminished in this design, a constant firing rate and the associated energetic consistency were unobtainable. In spite of this difficulty, the spark discharge system proved to be a useful element-selective gas chromatographic detector.

Most recently, a single gap design incorporating a thyratron tube to control the spark firing rate has been developed. Control over the firing rate is achieved by placing the thyratron in series with the spark gap. Since the thyratron is electronically triggered, a firing rate independent of the gap environment is attained. Preliminary work by Calkin (4) with the thyraton-triggered spark gap indicated that the firing rate was completely independent of the spark environment; however, the ability to hold the electrodes at a voltage greater than the breakdown potential caused uncontrollable arcing to the spark chamber walls.

Additional mechanical and electrical problems arose due to the characteristics and requirements of the thyratron-controlled spark source. This necessitated a redesign of the spark chamber.

This chapter presents an overview of the spark system and a description of the gas chromatographic components. The spark chamber design and spark/GC interface are discussed.

A. Overview of the Spark Atomic Emission System

The spark system is illustrated in Figure 3-1. In operation, gaseous sample is continuously introduced into the spark chamber perpendicular to the interelectrode axis. Spark ignition occurs shortly after the thyratron is triggered into conduction. Once this occurs, the sample is atomized and excited, and radiation is emitted. This radiation consists of an intense continuum emission and characteristic atomic emission from the sample and

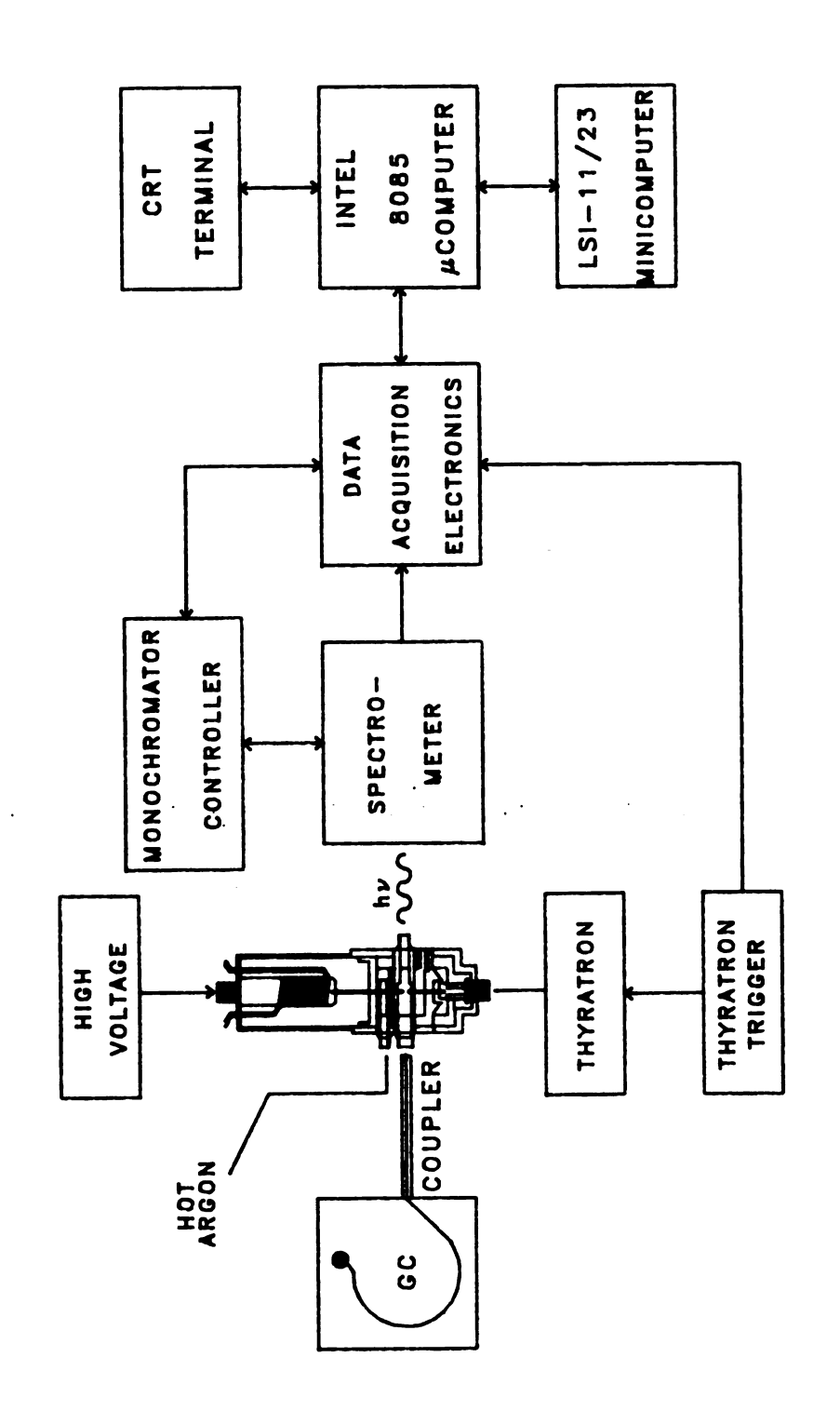


Figure 3-1 Block Diagram of the NSS-GC System

the plasma support gas atoms. The monochromator (GCA-McPherson EU-700) isolates the desired wavelength band. Discrimination against the relatively short-lived continuum emission is accomplished by gating the photomultiplier tube in the spectrometer. Consistent timing relative to the spark ignition is accomplished with a synchronization pulse obtained from the thyratron driver circuitry. After a short delay relative to the spark ignition, the photomultiplier is rapidly gated from a low to a high gain state. The PMT signal is passed into a gated integrator and programmable gain amplifier; it is then digitized by a twelve bit analog-to-digital converter. The digitized signal is then read by the microprocessor and temporarily stored. To improve the signal-to-noise ratio, emission intensities from multiple sparks are averaged by the microprocessor, and stored as a single data point. This data point can be permanently saved on flexible disk media. Alternatively, the averaged signal can be displayed on a strip chart recorder after digital-to-analog conversion; this permits real time observation of the acquired data. Subsequent to the data acquisition run, the data are transferred through a serial line to an LSI-11/23 minicomputer where higher level data manipulation is performed. A CRT terminal is used for operator interaction with the data acquisition software running on the microprocessor and for communicating with the minicomputer. Hard copy plots and printouts are obtained from a dot matrix printer attached to the minicomputer.

B. Spark Source Design

A diagram of the spark chamber is shown in Figure 3-2. The spark chamber consists of three sections: a coaxial capacitor and mount, the analytical chamber, and a cathode mounting stage/high voltage connection. A description of these sections follows.

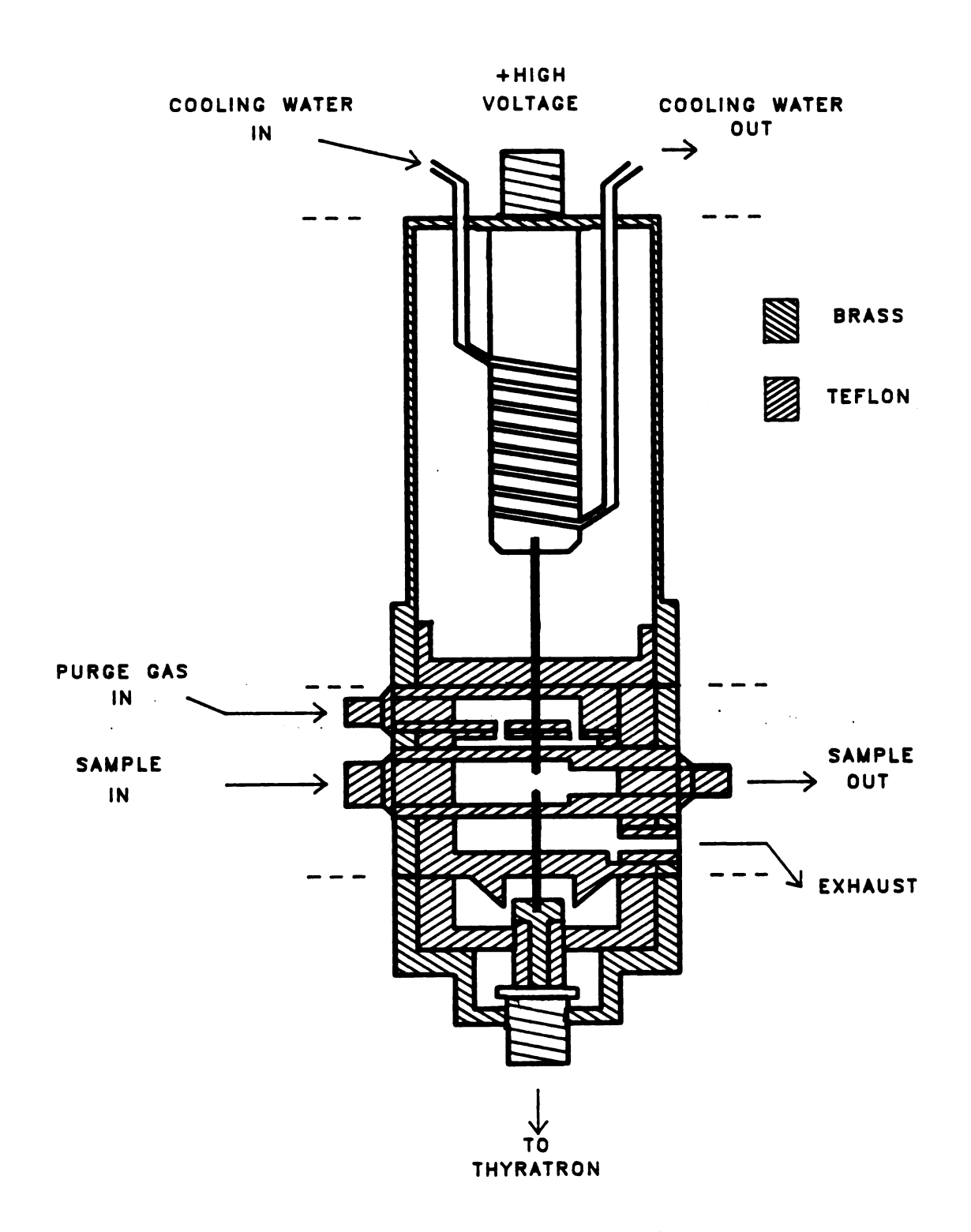


Figure 3-2 The NSS Housing

The coaxial capacitor section is similar to that described by Calkin (4). A few minor modifications have been made. First, the set screw holding the anode into the capacitor has been relocated. Orginally, the set screw was mounted perpendicularly to the electrode axis, causing the sharp edge of the set screw access hole to be located within two millimeters of the dielectric material. Under extreme operating conditions, this generated an electric field of sufficient strength to cause the electrical breakdown of the dielectric material in the area of the set screw access hole. This led to the destruction of the capacitor and to a tedious repair procedure. To eliminate this problem, the set screw was angled into the electrode from the bottom of the central capacitor core. This provides sufficient clearance to avoid capacitor destruction from this cause under all conditions studied.

Secondly, a screw contact to the bottom of the capacitor was incorporated to allow connection of an anode access wire to the capacitor. The wire is passed out of the spark chamber, to provide one contact for a bridging resistor. Incorporation of an external bridging resistor greatly simplified resistor replacement and spark disassembly procedures.

The final modification fo the capacitor section is the incorporation of a Teflon wall between the capacitor section and the spark chamber. This provides a barrier to prevent the sample from contaminating the capacitor section and to improve electrical and thermal isolation of the capacitor section from the remainder of the spark source.

An expanded view of the analytical chamber is shown in Figure 3-3. With thyratron control over the spark breakdown, it is possible to overvolt the spark gap. To eliminate arcing caused by the overvolt condition, the entire analytical chamber interior was insulated with approximately 1/4 inch thick Teflon. Complete electrical insulation was obtained by machining all parts

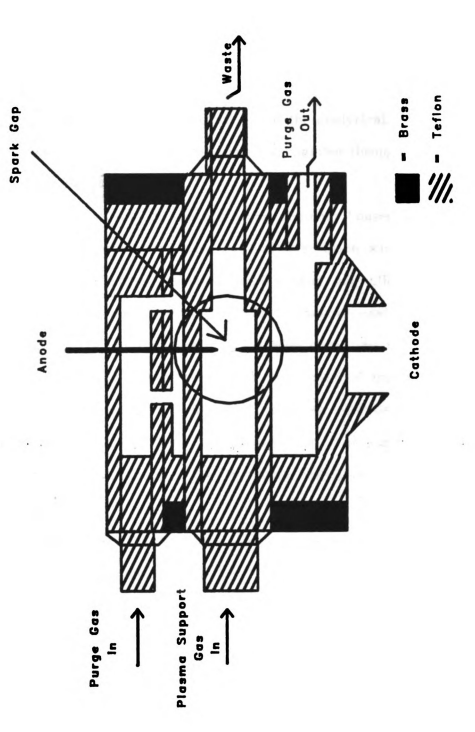


Figure 3-3 The Analytical Chamber, expanded view

to provide a tight, press-fit with adjacent components.

The upper portion of the analytical chamber is fitted with the purge gas inlet. Connection to an external gas line are made with Teflon Swagelok fittings. Gas exits from the purge gas inlet through a series of holes concentrically arranged around the interelectrode axis. This sets up a regular flow pattern from the top to the bottom of the analytical chamber, and purges any extraneous sample. Purge gas exits the chamber through a 3/8-inch opening in the lower chamber wall.

The center section of the analytical chamber houses an interchangeable Teflon flow cell, the spark gap, and an observation window. The flow cell decreases the effective detector dead volume and allows optimization of the detector geometry for a particular sampling environment. A sample stream and heated argon support gas stream enter one end of the flow cell through a Teflon Swagelok fitting. At the center of the cell, the flow path intersects with the spark gap. This region is monitored through 3/8-inch observation port in the flow cell. A one-inch focal length lens, mounted in the chamber wall, focuses the discharge radiation emitted through the observation port.

The two electrodes that form the spark gap are 0.04-inch diameter, two percent, thoriated tungsten electrode (Union Carbide, Linde Division) and are located in the center of the flow cell. The anode is connected directly to the coaxial capacitor. The cathode is electrically connected to the anode of the thyratron. To decrease the severity of spark wander between the two electrodes, the final half inch of the electrodes are electro-polished to a very fine point. Sharpening is performed by placing the end of the electrode into a saturated solution of sodium nitrite and applying approximately 40 volts a.c. between the spark electrode and a counter electrode placed in the

solution. Approximately ten minutes are required for complete sharpening.

The lower third of the analytical chamber contains the purge gas exhause port and a Teflon wall to separate the analytical chamber from the lower electrode mounting stage.

The last section of the spark chamber contains the lower electrode mounting stage. The lower electrode is fastened into the Teflon-covered brass stage with a set screw. A cathode access wire is attached to the stage with a screw connection. The access wire is passed through the chamber wall and soldered to the cathode end of the bridging resistor. A high voltage connector (Amphenol 82-856) is screwed into the base of the stage. The outer threading of the connector is screwed through the base of the spark chamber. Rotation of the connector moves the cathode relative to the anode, to allow adjustment of the gap length. This compensates for erosion of the lower electrode during normal operation. The entire spark chamber is fastened together with four 4 3/8-inch bolts.

The anode and cathode access wires pass through the chamber wall and into the bridging resistor housing. A resistor is soldered between the access wires and an insulated brass cover is placed over the resistor. Since the resistor is externally mounted, it is effectively isolated from the high temperature environment often present in the spark chamber. Because of this isolation, resistor burnout associated with the Calkin design has been eliminated. In addition, spark chamber disassembly procedures have been simplified because of the increased resistor accessibility.

C. Thyratron Controlled Spark Source

Thyratrons have been used successfully in applications which require rapid, reproducible high voltage switching (87-89). these include triggering

a spark discharge (89). The schematic diagram of the thyratron-controlled spark source is shown in Figure 3-4. In operation, a high voltage power supply (Spellman UHR10P100) charges the capacitor through the current-limiting resistor R_L. When the thyratron (EG&G model HY-6 hydrogen thyratron) is non-conducting, both sides of the spark gap remain at the same potential and no spark is formed. When a positive voltage trigger pulse is imposed on the grid of the thyratron, the spark gap cathode rapidly switches to ground. This generates a potential difference between the spark electrodes, causing a spark to form. After the energy stored in the capacitor is dissipated, the thyratron is returned to the non-conductive state, and the charging cycle resumes.

A constant hydrogen atmosphere inside the thyratron is generated by electrically heating a titanium hydride reservoir (90). When an 800 volt trigger pulse is imparted on the grid, hydrogen ionizes, and the thyratron becomes conductive. After the trigger pulse is removed, the hydrogen deionizes, and conduction ceases.

A six-volt, twelve-ampere, DC power supply provides the current for the hydride heater and the thyratron cathode. A DC supply is used to minimize trigger jitter caused by line-frequency modulations (91). Trigger jitter of under ten nanoseconds duration can be obtained by use of a regulated power supply. Thyratron ignition is accomplished with a EG&G TR-27 trigger module. A pulse from the trigger module synchronizes data acquisition timing with spark ignition.

D. Capillary Gas Chromatograph - Spark Interface

The chromatographic interface used with the spark is pictured in Figure 3-5A. The interface design is based on Calkin's (4) packed column interface.

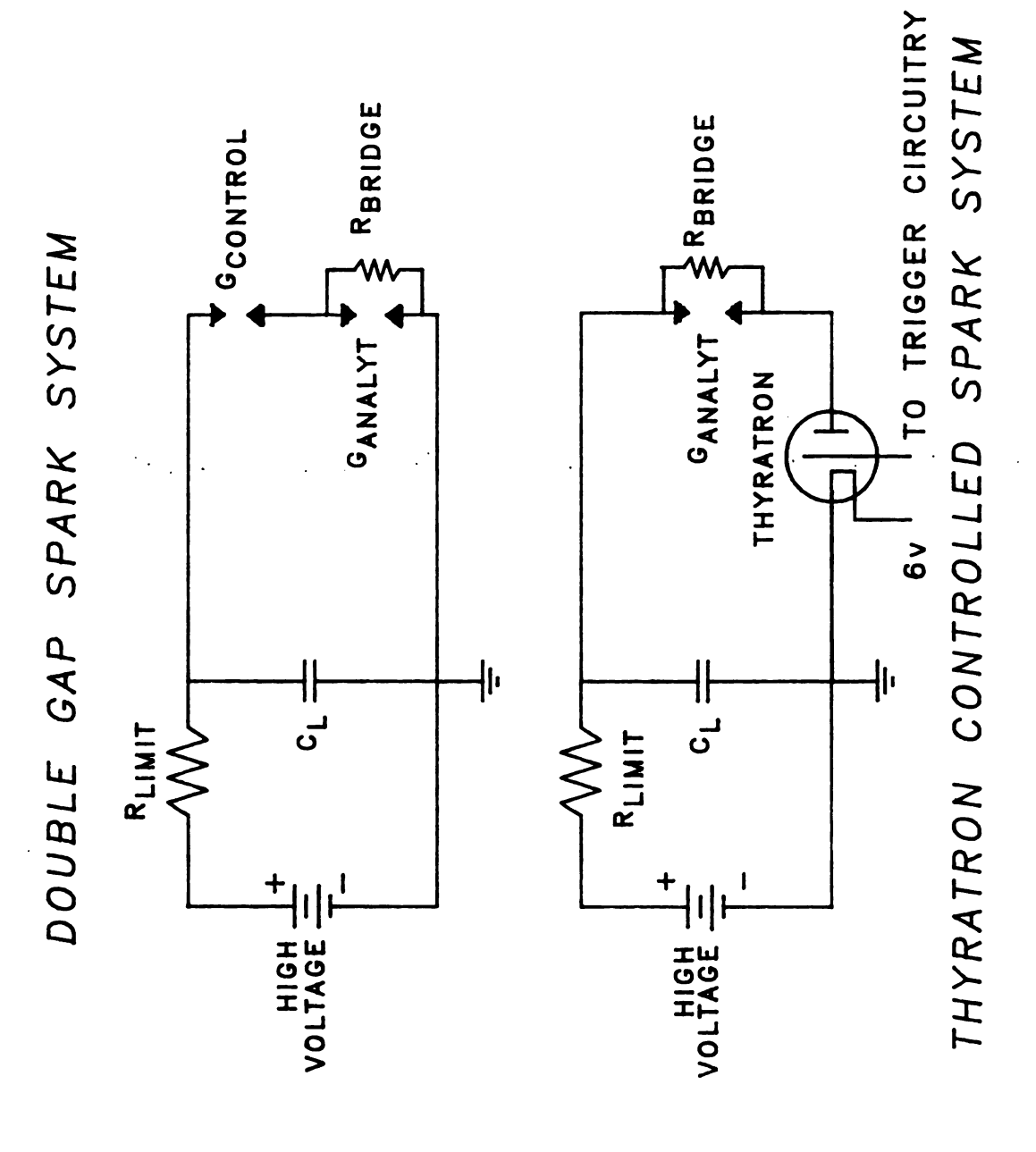
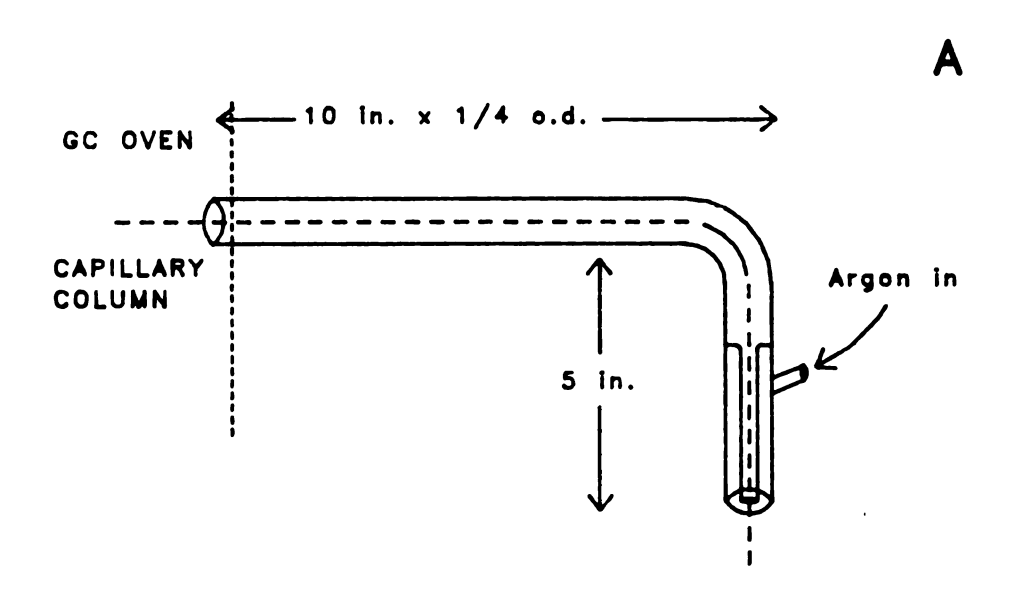


Figure 3-4 Circuit Diagram of Thyratron-Controlled Spark Source



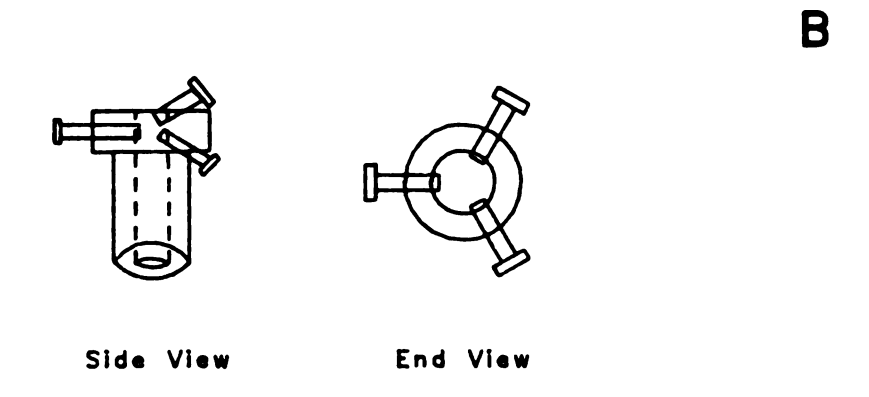


Figure 3-5 GC - Spark Interface

The interface is constructed from 1/4-inch O.D. glass tubing. Since capillary GC flow rates are inadequate to provide sufficient support for the spark plasma, an auxiliary argon support flow is supplied through the sidearm on the interface. The support gas flow rate is controlled with a Lab Crest flow meter. Glass is used in preference to a sturdier metal interface to allow observation of the column as it is threaded through the interface. This minimizes possible column breakage during this process. In addition, the glass interface insulates the equipment and the operator from the high voltage present in the spark gap.

The entire interface is heavily wrapped with a flexible heating cord to prevent condensation of the chromatographic effluent. Measurements with a chromel-constantan thermocouple indicate no difficulty maintaining interfacial temperatures at 280°C, the maximum recommended column temperature. To minimize the detector dead volume, the capillary column is extended past the end of the interface to within two to three mm of the spark gap. Attempts to position the column closer to the gap caused intermittent arcing to the end of the column, and resulted in an excessively noisy signal and destruction of the column coating. The effective detector volume under these conditions is approximately 50 nl.

The Teflon collar pictured in Figure 3-5B is used to connect the interface to the spark chamber. Adjustment of the three radial screws allows accurate positioning of the column relative to the discharge axis.

E. Solution Introduction System

The current spark chamber has been designed to accommodate many sampling environments, including operation in solvent mists as produced by a nebulizer. Two types of nebulizers have been used for solution introduction.

A Plasma-Therm UNPS-1 ultrasonic nebulizer system, pictured in Figure 3-6, was tested for use with the spark system. This setup is commonly used for sample introduction into inductively coupled plasma torches (92). In operation, a ceramic piezoelectric transducer is powered by a radio-frequency (RF) generator tuned to the resonant frequency of the transducer, approximately 1.4 MHz. Frequency adjustment of 10 kHz on either side of this central frequency was possible (93). Cooling water was supplied at a rate of 3 gallons per hour to dissipate heat generated in the transducer. Solution was pumped to the transducer surface with a single channel peristaltic pump (Ismatek AMY8.1-AB2.5SR) at approximately one ml/min. A heated argon gas flow flushed the solution mist from the nebulization chamber to the spark chamber via a five-inch long piece of 1/4-inch i.d. glass tubing. The nebulization chamber and the transfer tube were wrapped with heating tape and heated to approximately 120°C to assist in vaporization of the sample.

The crossflow nebulizer of Donohue and Carter (94) pictured in Figure 3-7 was also used for sample introduction. Two four-inch stainless steel tubes, 0.095-in o.d., are used for solution uptake and argon inlet lines. A 1/4-in piece of 0.029-in o.d. stainless steel capillary column is silver-soldered into the tip of each inlet line. To avoid excessive backpressure, the length of fine bore capillary tubing is kept as short as possible. A high velocity stream of argon across the uptake line aspirates solution into the nebulizer chamber. Proper capillary alignment is required for optimum nebulizer performance. Alignment is obtained by tighening the appropriate nylon mounting screws for each capillary. Earlier nebulizer designs incorporated metal-jacketed glass capillaries or all-glass capillaries which were frequently chipped or broken; this caused erratic, non-uniform nebulization. The incorporation of stainless steel capilaries has eliminated this problem.

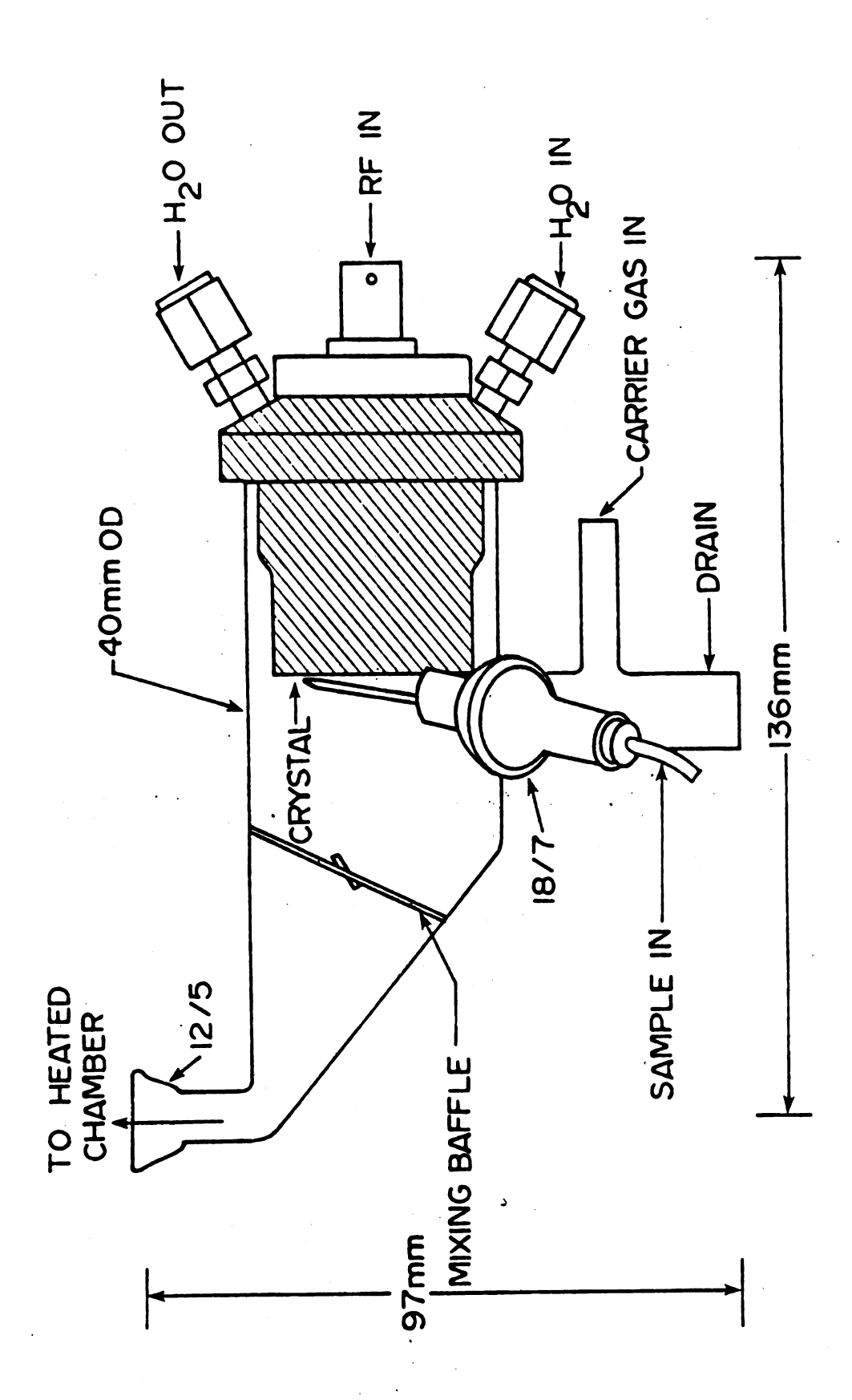


Figure 3-6 Ultrasonic Nebulizer

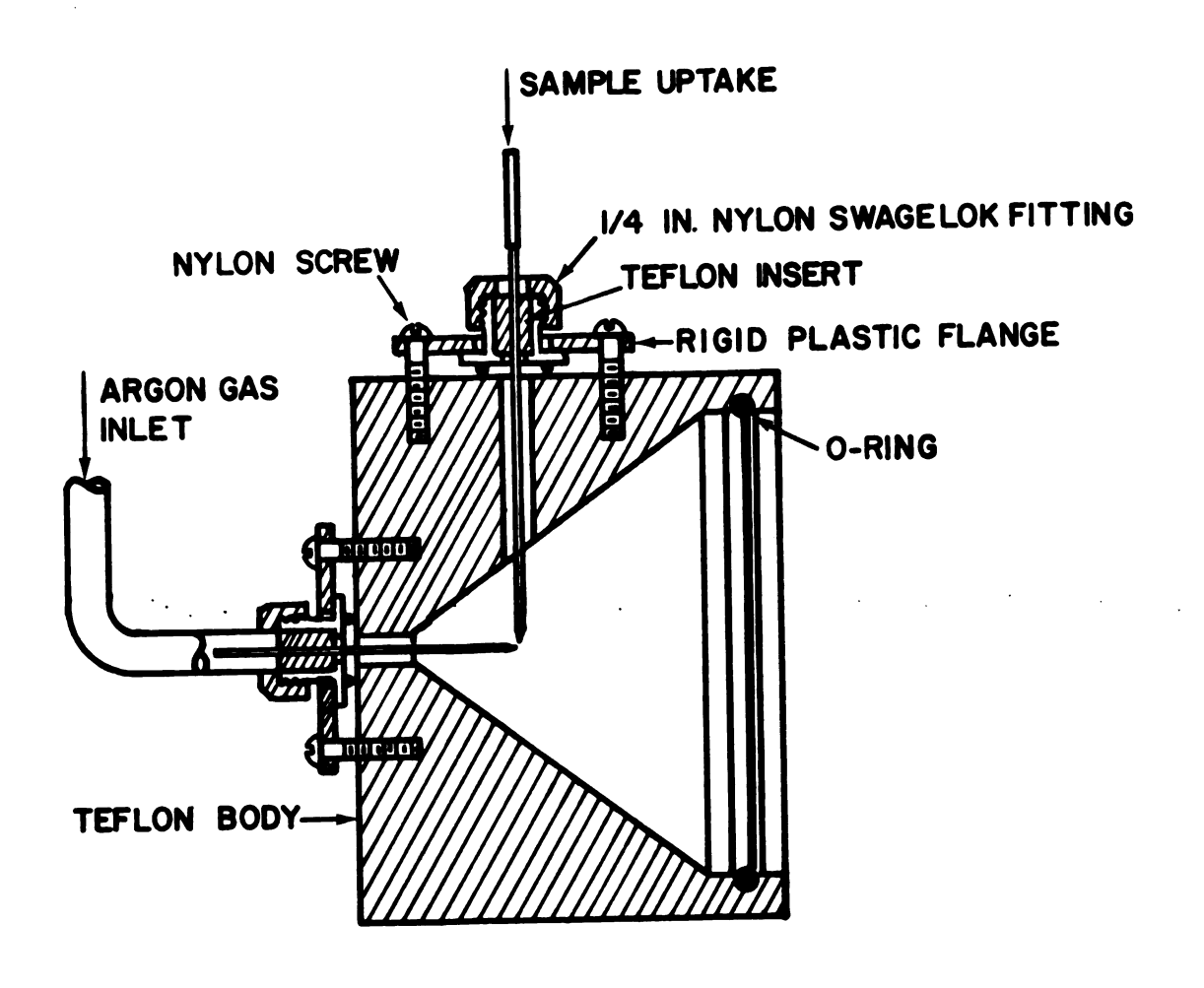


Figure 3-7 Cross-Flow Nebulizer

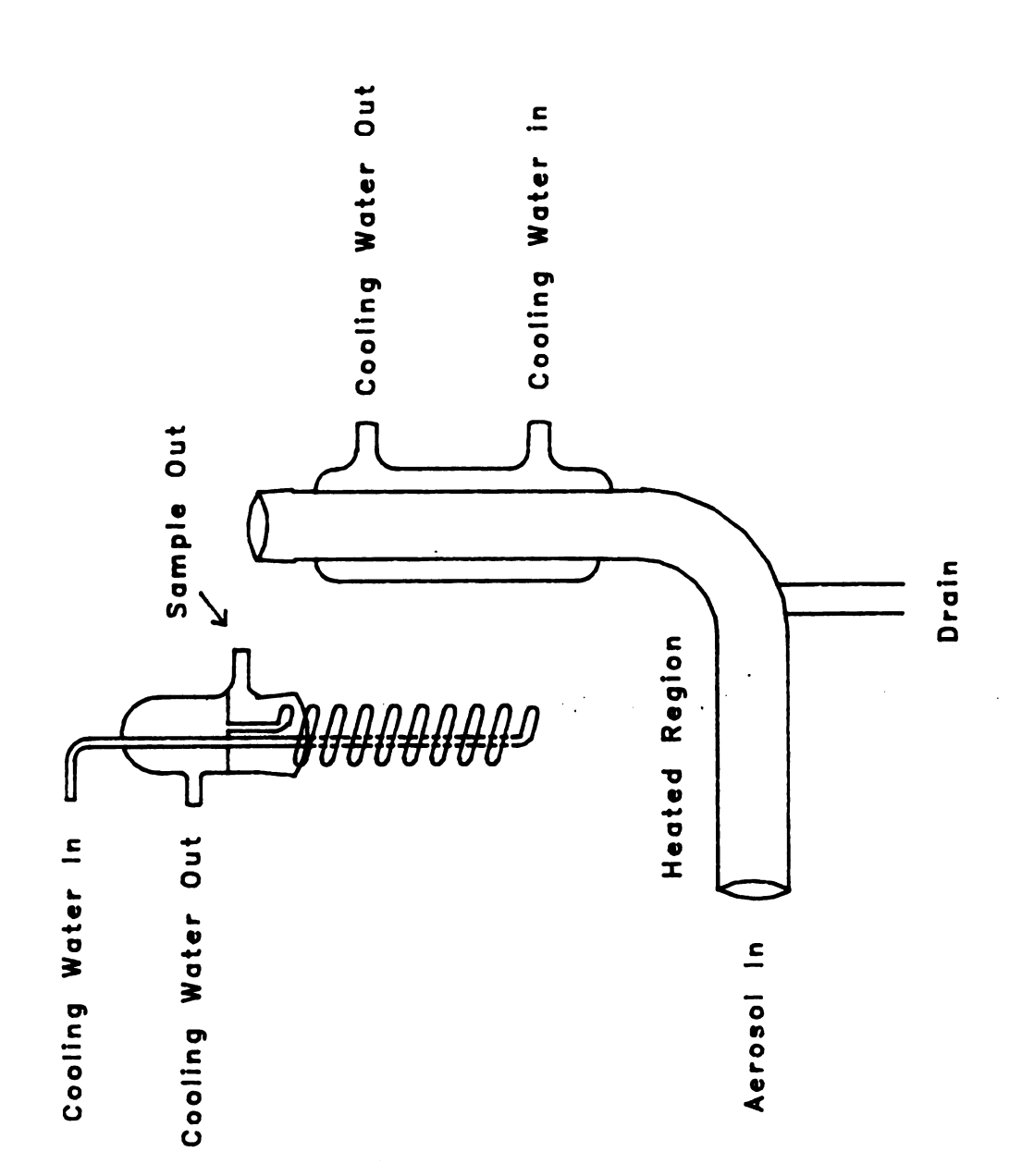


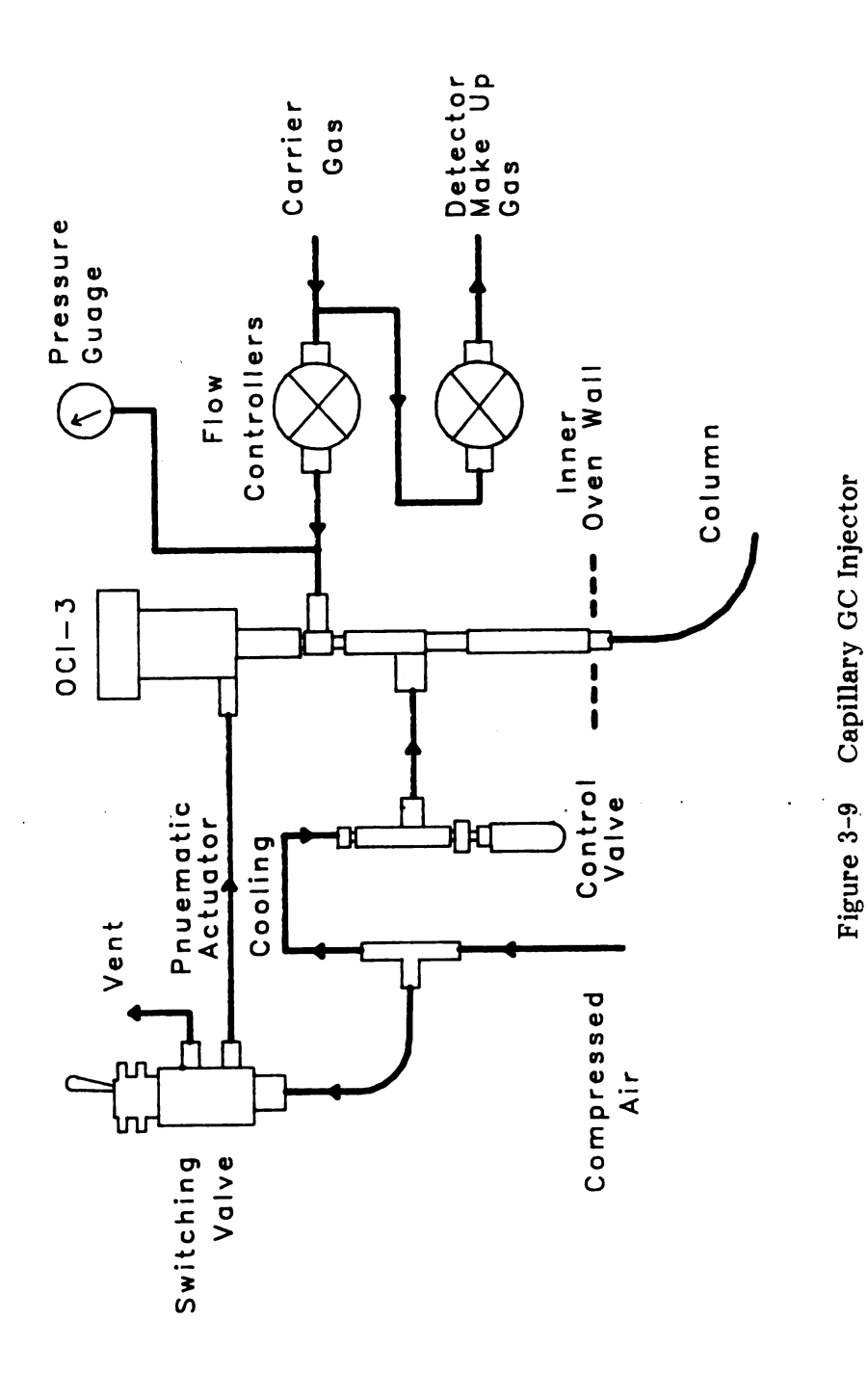
Figure 3-8 Miniaturized Desolvation Chamber

Adequate nebulizer performance was observed above an argon flow rate of 0.5 l/min. Care must be taken to provide a snug fit of all components to insure consistent positioning control during use.

The low-volume mixing/vaporization/desolvation chamber pictured in Figure 3-8 was used to decrease the amount of solvent reaching the spark chamber. The front four inches of the chamber are wrapped with heating tape to vaporize the nebulized solution. The desolvation portion of the chamber consists of a four-inch long condenser with an inner, water-cooled, helical glass coil; this provides a relatively large surface area volume.

F. Gas Chromatographic Components

All gas chromatography was performed on a Varian 1400 series GC. Two capillary columns have been used with this instrument; a 30 meter long, wide bore (250 micron) column with an 0.25 µm thick DB-1, equivalent to SE-30 or OV-1, (Anspec DB-1-30W-.25) and a 25 meter 320 µm bore column with a 5.0 µm thick methyl silicone coating (Quadrex 007-1-25W-5.0F). Both of these columns are similar to an OV-1 column (95). The greater film thickness available in the Quadrex column allows for heavier column loading, up to 1.0 µl, without serious degradation of chromatographic separation. The injector was constructed from Scientific Glass Engineering Inc. on-column injector kit OCI-3 shown in Figure 3-9. On-column injection permits quantitative transfer of the sample onto the front of the column, and is most appropriate for very dilute and wide boiling range samples. High purity helium (99.9999 % pure Linde) carrier gas is passed through a 0.5 ml/min flow controller to provide temperature independent flow rate through the column. Compressed air was supplied at 40 psi to provide injector coolant gas and to drive the pneumatic head seal. Injector coolant gas was required to prevent sample



fractionation in the syringe and to minimize deterioration of the injector seals when the switching valve is opened. Pneumatic pressure is applied to the head seal and the head seal opens. The head seal is closed when the switching valve is closed and pneumatic pressure is released. Proper injection technique was required to provide analytically useful information and to keep the injector in good working order for a long time. To perform an injection, the head was inserted until it touched the silicone head seal. After opening the head seal with the switching valve, the syringe was completely inserted and the head seal was closed. After a three second delay to smooth an inherent pressure surge in the system, the sample was injected. One of two injection techniques were used depending on the sample size. For a sample size of less than 0.4 µl, a rapid injection is preferred. Alternately, for a large sample, a slow injection rate allows the sample to be carried down the column by the carrier gas, preventing sample loss off the start of the column (96). After injection, the syringe was removed without reopening the head seal. When connecting the capillary column to the injector, the end of the column must be cut smoothly and inserted into the countersunk end of the injector and fastened. If the syringe cannot be smoothly inserted into the column, the column should be reconnected. Failure to do this leads to syringe breakage and injector damage. During initial setup of the injector, the final 1/4 inch of the injector was extended into the GC oven to permit heating of the entire column.

A 5.0 µl syringe (SGE 5A-50C-1005) with a 100 mm long stainless steel sheathed fused silica needle (SGE VS170/100) was used for all injections. For adequate injector performance, the final 20 mm of the needle must be unsheathed to ensure proper insertion into the column. Needle breakage is commonly caused by improper allignment of the end of the column in the

injector. When this occurs, the needle should be replaced and the column realligned to insure proper injector performance.

G. Alternate Spark Imaging Scheme

It was found that imaging the spark with a single lens mounted in the spark chamber wall provided less than optimal light throughout. To improve this aspect of the system, an auxiliary adjustable multi-element lens mount shown in Figure 3-10 was developed. The design consists of three concentric tubes and two variable position, one inch diameter lends holders. A third lens can be positioned in the spark chamber wall. One end of the mount replaces the lens retaining ring in the observation port, providing a stable reference point for the lens system. The two lens holders incorporated in the imaging system are each capable of approximately one inch of independent axial movement. Each lens can also be independently rotated to provide for specific angular orientation of radially nonsymmetrical cylindrical lenses. By use of lenses with various focal properties and exploitation of the adjustability of this lens mount, a wide range of spark imaging characteristics is attainable.

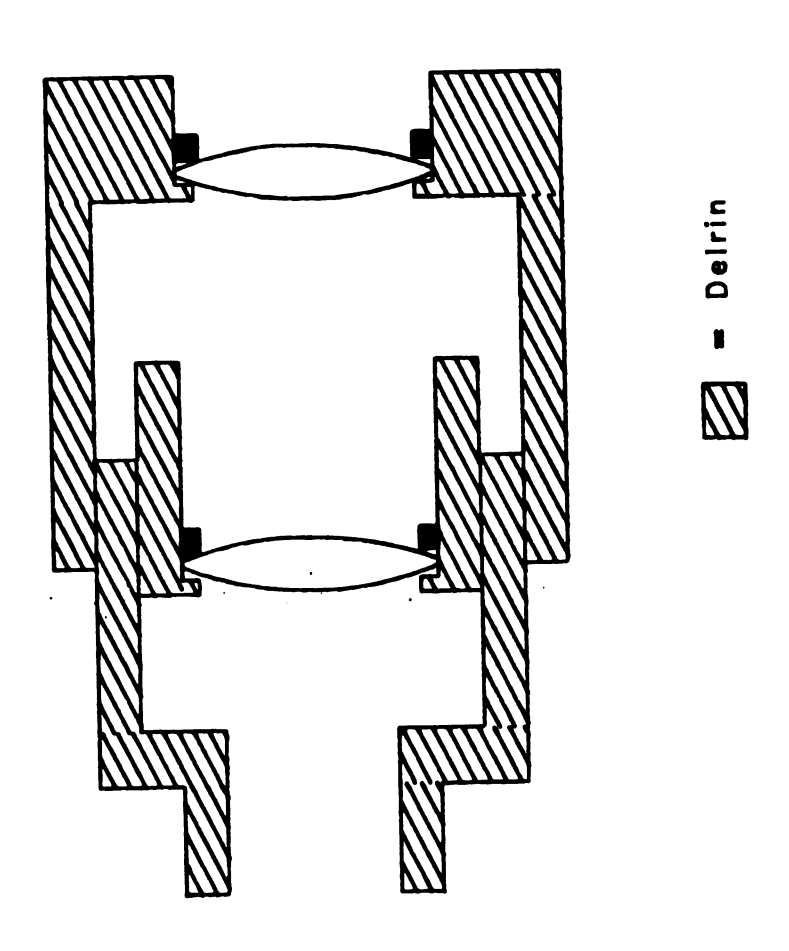


Figure 3-10 Alternate Lensing Scheme

CHAPTER IV

ELECTRONICS AND OPERATION

The data acquisition process is under complete microcomputer control. A block diagram of the acquisition system is presented in Figure 4-1. The Intel 8085 microcomputer designed by Newcombe (97) performs all communication, control, and process coordination between the instrument, mass storage capabilities, the operator, and the multiuser minicomputer. The basic data acquisition scheme consists of microcomputer control of several timing functions, acquisition of digitized emission intensities, and storage of averaged data onto flexible disk media. Subsequent to the acquisition of data from an entire experiment, data are transferred via a serial line to an LSI-11/23 minicomputer where higher level smoothing, plotting, and statistical analysis are performed.

This chapter presents a brief description of the microcomputer system.

The circuitry unique to the spark detector is discussed in depth. A brief discussion of the higher level computing capabilities available on the minicomputer is presented.

A. The Intel 8085 Microcomputer

The block diagram shown in Figure 4-2 illustrates the components of

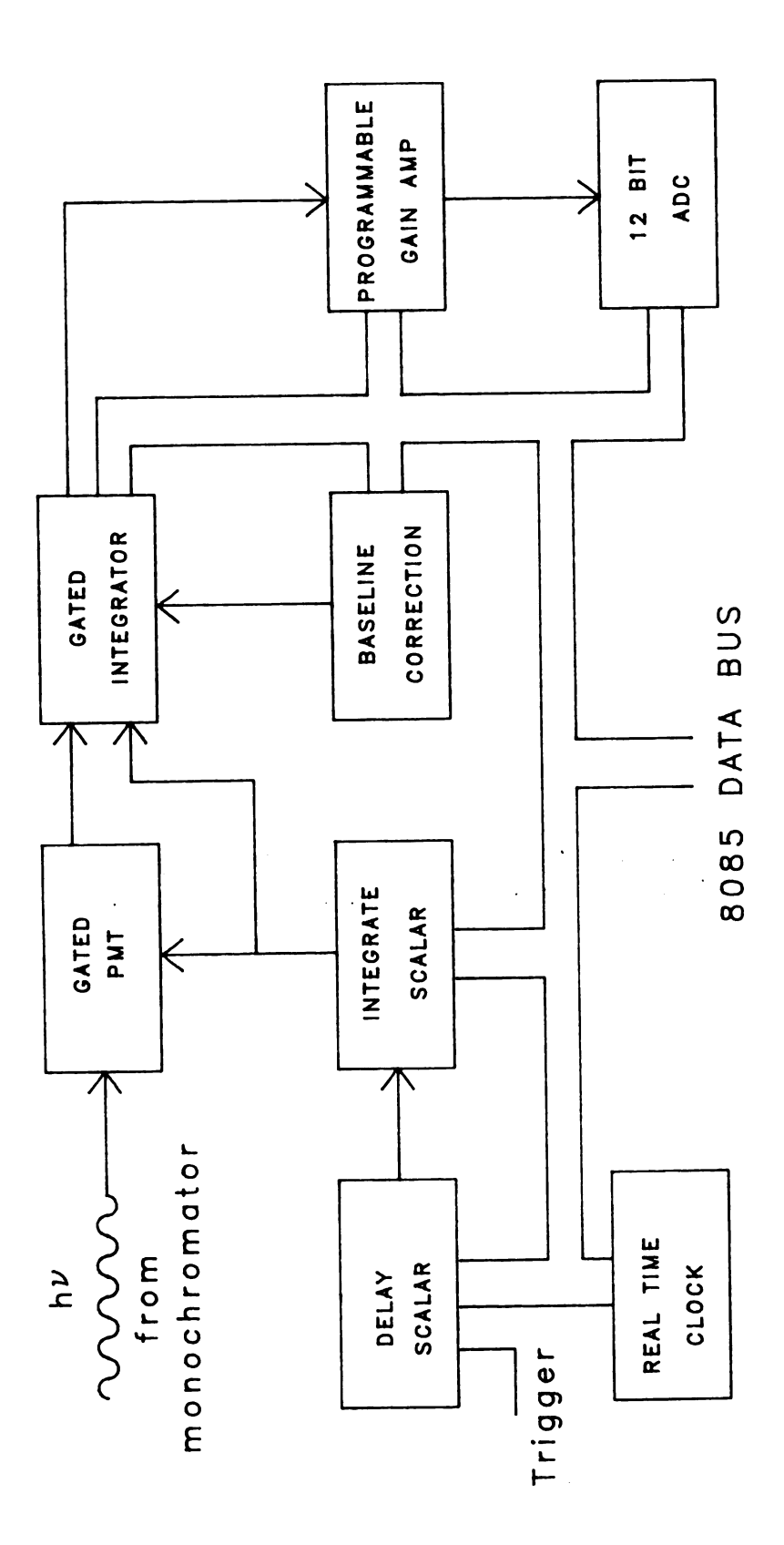


Figure 4-1 Block Diagram of Data Acquisition Electronics

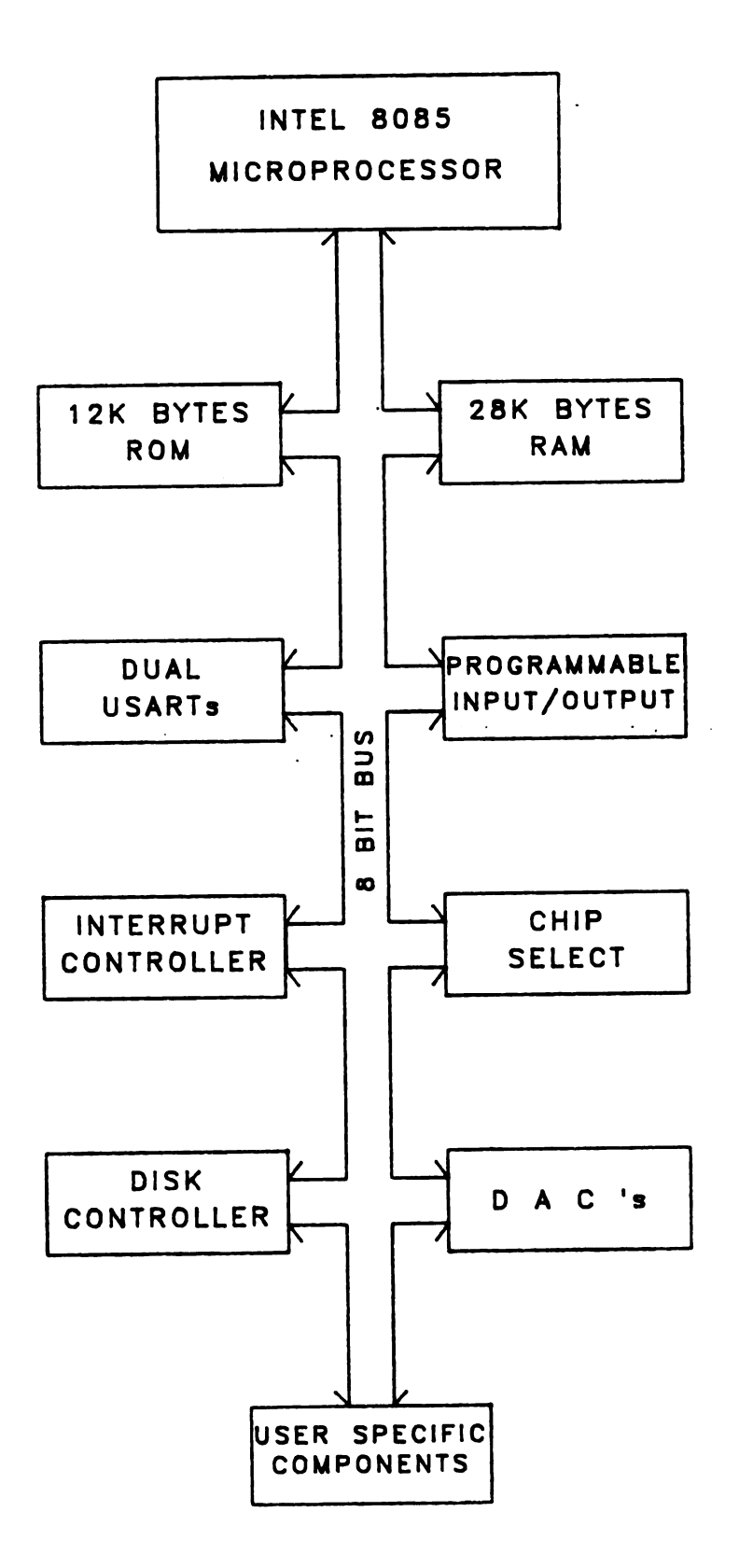


Figure 4-2 Block Diagram of Intel 8085 Microcomputer System

the general microcomputer system used in the spark data acquisition system.

The 8085 microcomputer has an eight-bit data bus and a sixteen-bit address bus which allows for a maximum of 64K bytes of address space. The microcomputer contains 12K bytes of read only memory (ROM) and 28K bytes of random access memory (RAM). The 12K bytes of ROM are used for storage of the system routines such as: communication software, an editor, and the FORTH compiler used on the system. The 28K bytes of RAM are used to store system variables, the screen buffers used in the FORTH system, and user variables, programs, and buffers. Communication to a terminal and the minicomputer is performed with the two universal synchronous/asynchronous receiver transmitter (USART) and the interrupt controller chips provided in the system. The minicomputer USART is hardwired to operate at 4800 BAUD; however, the terminal USART is wired to allow software selection of a 4800 or 9600 BAUD transmission rate. The higher BAUD rate allows for a more rapid printout of help frames during the data acquisition process.

The disk controller circuit is based on the National Semiconductor INS1771-1 floppy disk controller chip. Two Siemens FDD-100-8 single density, 8 inch floppy disk drives are used as the mass storage devices for the system. To accommodate slight differences in the design of the less expensive Siemens drives versus the standard Schugart drives, a 20 ms interval (98) is required between stepping pulses to the drives instead of the standard 6 ms. These changes are accomplished through software configuration of the controller. In addition, these disks require the read/write head to be disengaged when the disk is not active and a 10 ms delay after the head is loaded. Each drive can access a total of 250K bytes or 250 FORTH blocks of storage per disk, which gives a total of 500K bytes of mass storage for the system. In this

application, one of the disks is used for software storage, while the other is used primarily for data storage during an acquisition run. This configuration provides between fifteen and twenty hours of continuous data acquisition per disk.

The final board required for microcomputer operation is the chip select board, which decodes the signals present on the address bus. When an address in the appropriate range is present, an active low pulse is generated. The active range for the board is determined by the hardwired base address on the board. The subsequent 512 addresses are decoded to give eight independent regions of sixty-four unique addresses. In addition, the highest active region is further decoded to provide eight read/write qualified segments of eight bytes each. These segments are selected only if a read or write operation is performed; this provides immunity from erroneous selection due to bus noise. If any of the addresses in a region are present on the bus, the chip select for that region will become active. In addition to providing a centralized way to access system devices, such as the USARTs and floppy disks, this board provides a simple method to address the data acquisition electronics, digital-to-analog converters (DAC's), and other devices.

Two, eight-bit DAC's with selectable output range (Analog Devices AD558) are used in the computer system. One of these is configured for 0 to 10 V full scale and drives a Heath model SR255B chart recorder. The second DAC is configured to output between 0 and 2.56 V and is part of the automated baseline subtraction circuit discussed later.

The final system board is the programmable input/output (PIO) board based on the Intel 8255A programmable peripheral interface chip. This device allows for configuration of three, eight-bit ports for parallel input or output to external devices. For two of the ports, port A and port B, all eight bits

must be dedicated to input or output for a given operation. However, the third port, port C, can be configured as eight bits of input or output, or, four bits of input and four bits of output. The configuration of each port is under software control which makes this a highly versatile interface device. The PIO board is an integral component in the monochromator controller interface which is discussed later.

The above components are mounted on one of two mother boards. The mother boards, in turn, plug into a backplane, thereby connecting the bus between the mother boards. Enough space is available on the backplane to incorporate four mother boards. The data acquisition electronics board occupies one of these slots.

B. Minicomputer Facilities

All high level data reduction routines were performed on a Digital Equipment Corporation LSI-11/23 minicomputer running the RSX-11M multiuser operating system. The minicomputer performs graphical data display and generates high quality plots and figures. File based archival data storage on flexible disk media is available at this level. An Integral Data Systems Paper Tiger IDS-560 printer was used to printout of run parameters and source code listings.

C. Data Acquisition Electronics (DAE)

The data acquisition process for a spark discharge detector system requires the incorporation of several powerful circuits to perform time-resolved atomic emission measurements. These components and the associated interface to the controlling microcomputer are presented in this section.

1. Device Selection Circuitry

Communication to the various devices in the DAE is accomplished by

assigning each device a unique address for access and reading from or writing to that address. To simplify interconnections between the microcomputer and the acquisition electronics, only one chip select line is required in addition to the microcomputer bus available on the backplane. All additional address decoding is performed on the DAE board; hence, the chip select line performs as a board select signal, BDSEL.

The circuitry required for successful address decoding is shown in Figure 4-3. To enable address interpretation, a read or write operation must occur to an address betweeen BFC0₁₆ and BFFF₁₆. This causes two events to occur. First, the output of the XOR gate goes to a high logic level and second, the BDSEL line form the microcomputer is asserted low. These events enable the 3-to-8 decoding of address lines A3, A4, and A5. When these three lines are asserted low, i.e. addresses between BFC0 and BFC7 are accessed; the chip select for the AMD9513 timer chip and its associated bus driver are selected over the $\overline{CS9513}$ line. For addresses between BFC8 and BFCF, the 1 output of the 3-to-8 decoder A is asserted low. This enables the second decoder to demultiplex address lines A_2 , A_1 , and A_0 . In addition, the $\overline{1}$ output is, after inversion, combined in a NAND gate with the least significant address bit (A_0) to enable the gain select latch. The resulting signal is inverted and used to latch the data present on the input of the 7475 four bit latch. The net result of this circuit is that data latching occurs only if one of the four odd addresses between BFC8 and BFCF is accessed. To complete the gain selection logic, the $\overline{1}$, $\overline{3}$, $\overline{5}$, and $\overline{7}$ outputs of the 3-to-8 decoder B are tied to the data inputs of the latch. The outputs of the latch are used to activate the gain selection relays. The latch outputs are connected to the five volt power supply through 0.01 µF capacitors to minimize switching transients and improve switching reliability.

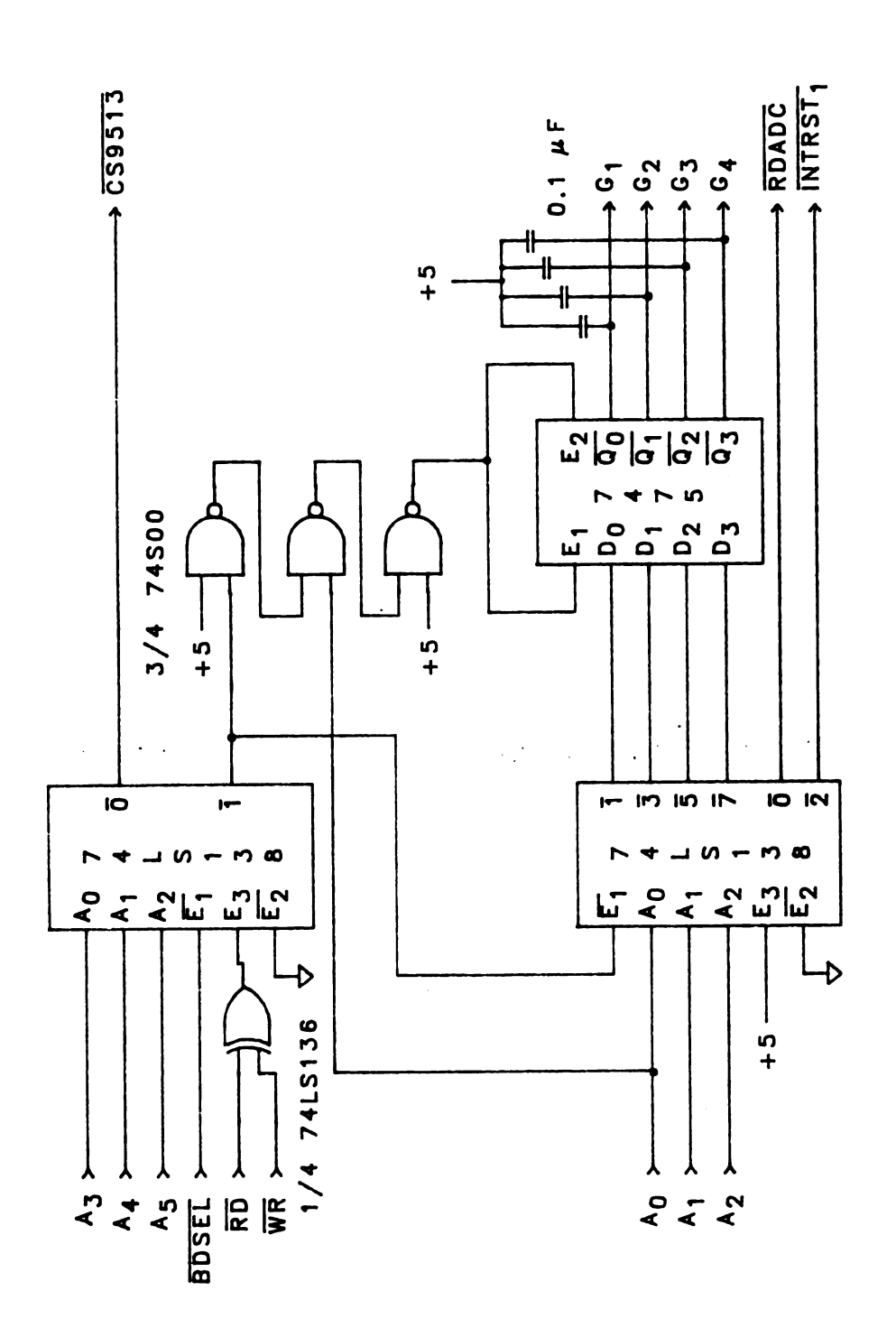


Figure 4-3 Interface Device-Selection Circuit

The $\overline{0}$ output of the second 3-to-8 decoder is used to access the analog-to-digital converter by asserting the \overline{RDADC} line. Finally, the $\overline{2}$ output asserts the $\overline{INTRST_1}$ line, which initializes the integrator reset pulse. These two circuits are discussed later.

2. Data acquisition timing

Several timing functions are required for proper operation of the data acquisition process. After the spark fires, a short delay period is required to allow the initial continuum radiation to diminish. Following this, an integration period elapses during which the photomultiplier output is integrated. These periods are typically a few microseconds in duration and are controlled by the microcomputer. In addition to the rapid timing required, an elapsed time clock capable of operation over the maximum duration of a typical gas chromatographic run is necessary for subsequent reconstruction of the chromatogram. These timing criteria were met and exceeded by a single integrated circuit, the Advanced Micro Devices AM9513. A brief description of this device is required for full appreciation of its versatility and flexibility.

The AM9513 system timing controller shown in Figure 4-4 consists of system control registers, a frequency source, and five independent, hardware and/or software gateable, sixteen-bit counters/timers. The system control registers consist of a data register, a command register, and a master mode register. The command register and the data register send and receive all communications with the microcomputer. The command register receives instructions concerning the loading of data into the various registers, initialization, activation and deactivation of individual counters, and modification of specific system modes. The data register acts as a buffer between the microcomputer data bus and the source or destination register on the AM9513. By design, data are only transferred directly from the data

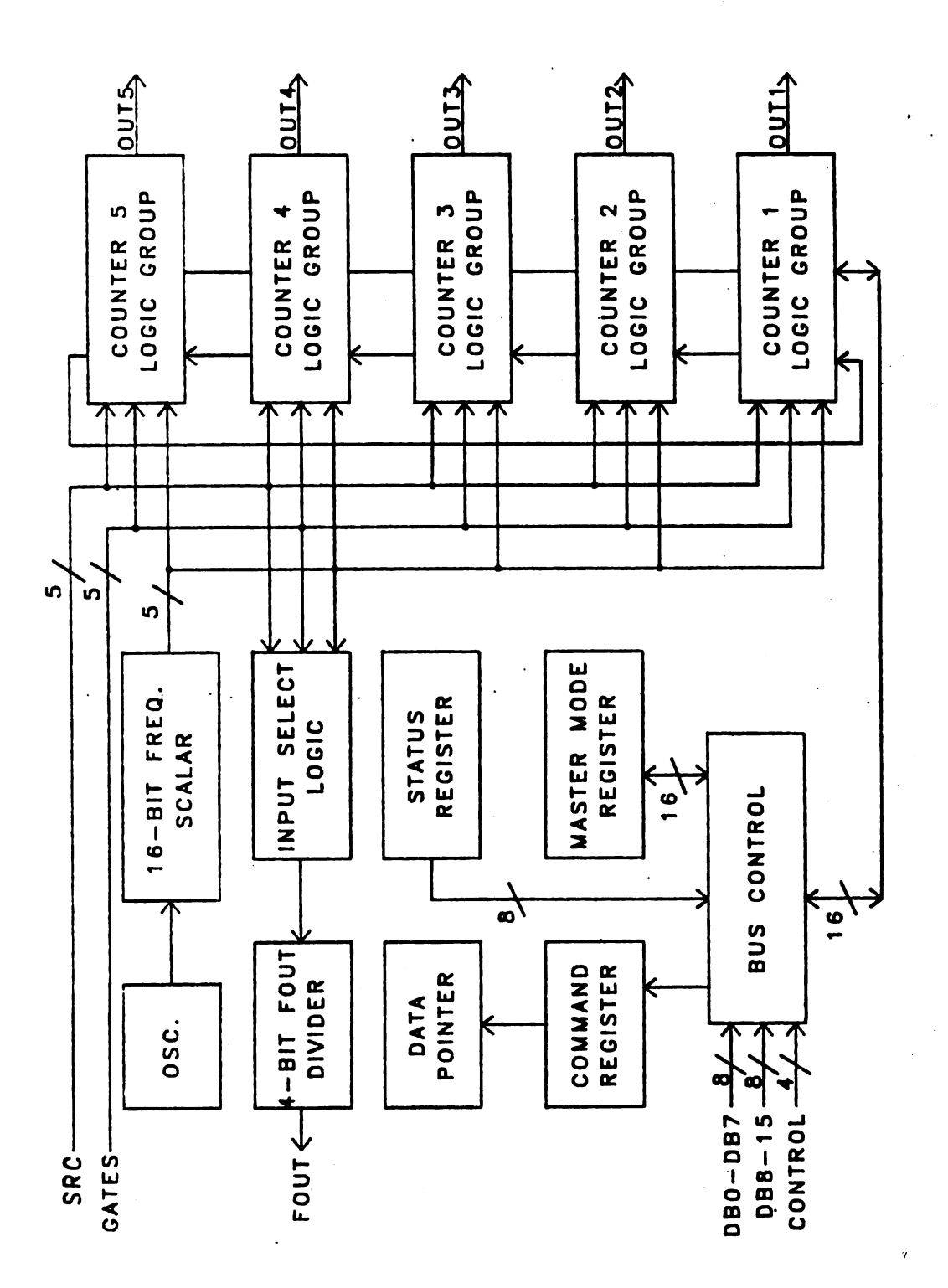


Figure 4-4 Block Diagram of Advanced Micro Devices AM9513

Timing Controller

register or the command register. When information concerning another register is transferred, the command register points to the appropriate internal register, a read/write operation is performed to the data register, and the AM9513 transfers the information between the data register and the appropriate internal register.

The master mode register controls the configuration of the frequency source, the data bus width, and the time-of-day counting mode. The frequency of the internal frequency source is derived from the system clock or any of the source or gate inputs for any of the five counters. A wide range of output frequencies is available by the incorporation of an internal frequency divider.

Each of the five counters diagrammed in Figure 4-5 consist of independent, software-accessible mode, load, and hold registers and hardware-accessible source, gate, and output ports. In addition, software gating of the timers is available. Each counter can be programmed to operate in any one of nineteen different modes. This capability gives this device much of its versatility.

To operate a given counter, the specific mode command must be loaded into the mode register, and starting values for the counter should be written into the load and hold registers as required. A counter-specific load command is then issued to initialize the counter to the appropriate value. If the application requires a specific initial output state, the output state should be set or cleared at this time. When the counter is to be activated, a counter-specific ARM command is issued. Counting/timing then commences as allowed by the source and gate inputs.

The AM9513 chip is used to control the critical timing requirements of the data acquisition electronics. These include generation of delay and integrate times, generation of a pulse stream to drive the monochromator

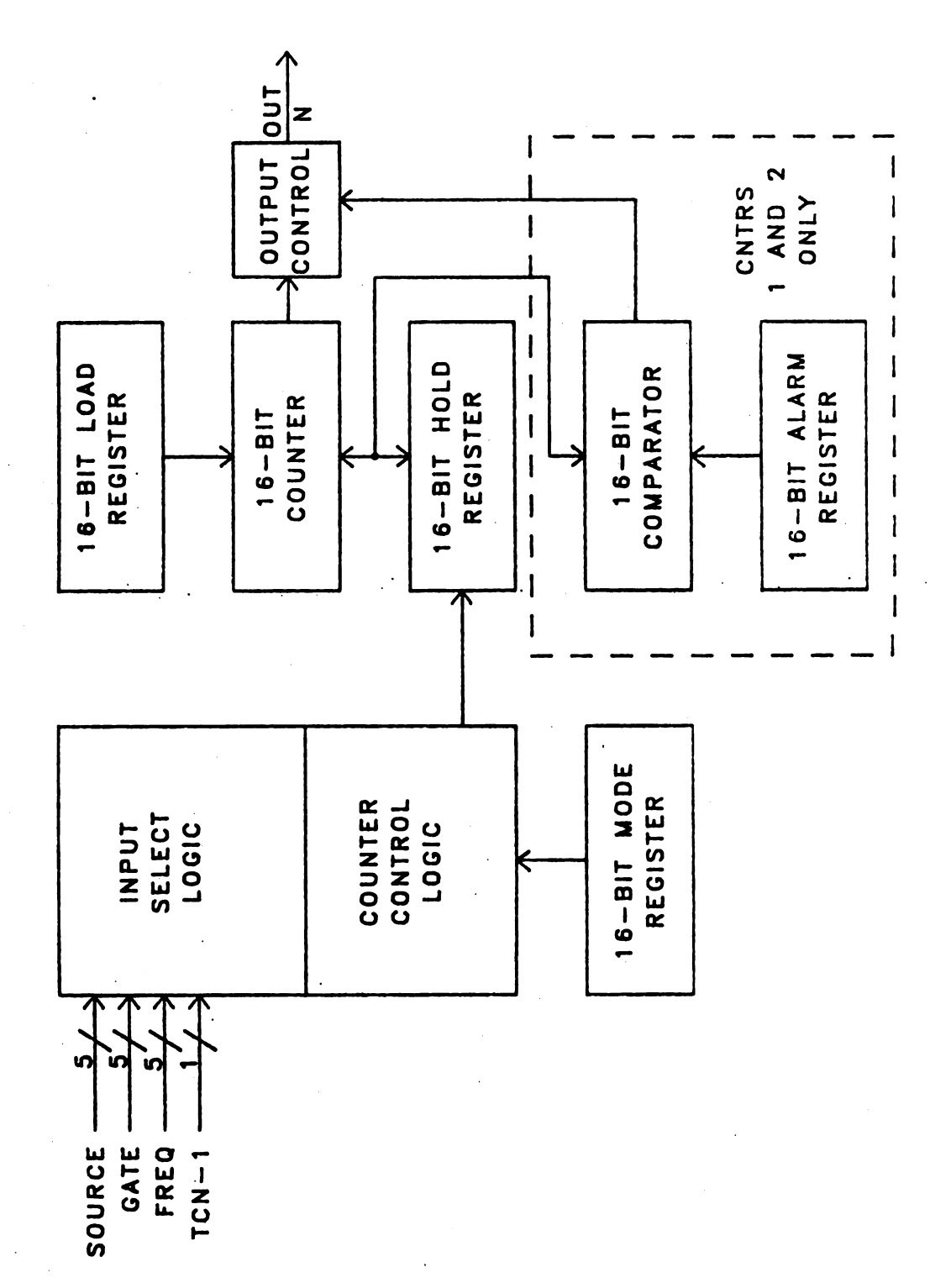


Figure 4-5 Block Diagram of AM9513 Counter Group

scan motors, initiation of the analog-to-digital converter, and operation of the elapsed time clock for time correlation of chromatographic data.

To perform these functions, three of the nineteen operation modes are selected for the various counters/timers. A brief description of these three modes will be useful in understanding the timing circuitry operation.

The first important mode is designated as "Mode A". A counter configured in this mode acts as a simple, one-shot, up or down counter. The counter will count edges occurring at the source input following an ARM command. On reaching the terminal count, i.e. the minimum or maximum values allowed for the counter, the counter disarms itself and inhibits additional counting until another ARM command is supplied. The internal count register is also reloaded with the contents of the load register on the terminal count. One of the two output functions can be obtained in this mode; either a pulse occurring during the terminal count or inversion of the output state following the terminal count. The second of these output modes is called "terminal count toggled output".

Square wave generation is accomplished using "Mode D". In this mode, the counter repetitively counts to the terminal count once it is armed. On the terminal count, the counter reloads itself from the load register. Selection of the terminal count toggled output mode will generate a square wave with a frequency equal to the count source frequency divided by two times the value stored in the load register.

The third mode of importance in this application is "Mode L". After loading the contents of the load register and arming the counters, a rising or failing edge at the gate input triggers the counter. The counter commences counting source edges. On the first terminal count, the counter automatically reloads itself from the hold register and continues counting. On the second

terminal count, the counter reloads from the load register. At this point counting stops until another triggering edge occurs at the gate input. Any gate edges which occur before the counter is armed or while the counter is counting are ignored. Use of the terminal count toggled output option in this mode generates a hardware-triggered, delayed pulse in which the length of delay and the pulse length are proportional to the values in the load and hold registers respectively.

The schematic diagram of the circuitry associated with the AM9513 timer is presented in Figure 4-6. The output of a 20 MHz crystal oscillator (Motorola K1091A) is halved using one stage of a 74S112 JK flip-flop. The resulting 10 MHz signal is supplied to the X2 input of the AM9513 to act as a master clock for the timer chip. Connection of the timer to the microcomputer data bus is made through a 74LS245 line transceiver.

The direction of operation of the transceiver is controlled by the S/R input, which is connected to the \overline{RD} bus signal. Both the transceiver and the timer are enabled with a low pulse on the $\overline{CS9513}$ signal, which is generated in the device select logic circuitry.

Access to the various registers on the timer is controlled by the three inputs \overline{WR} , \overline{RD} , and C/\overline{D} . These inputs are connected to the microcomputer bus lines \overline{WR} , \overline{RD} , and A_0 respectively. In this configuration, a write instruction sends data to the timer and a read obtains data from the timer. The state of the C/\overline{D} input determines whether the command register or the data register is accessed during an operation. Since this line is connected to the least significant address line, an input/output operation to the even address $\overline{CS9513}$ accesses the data register and an I/O operation to the odd address $\overline{CS9513}+1$) accesses the command register.

All five available timers are used in the data acquisition scheme. Timer

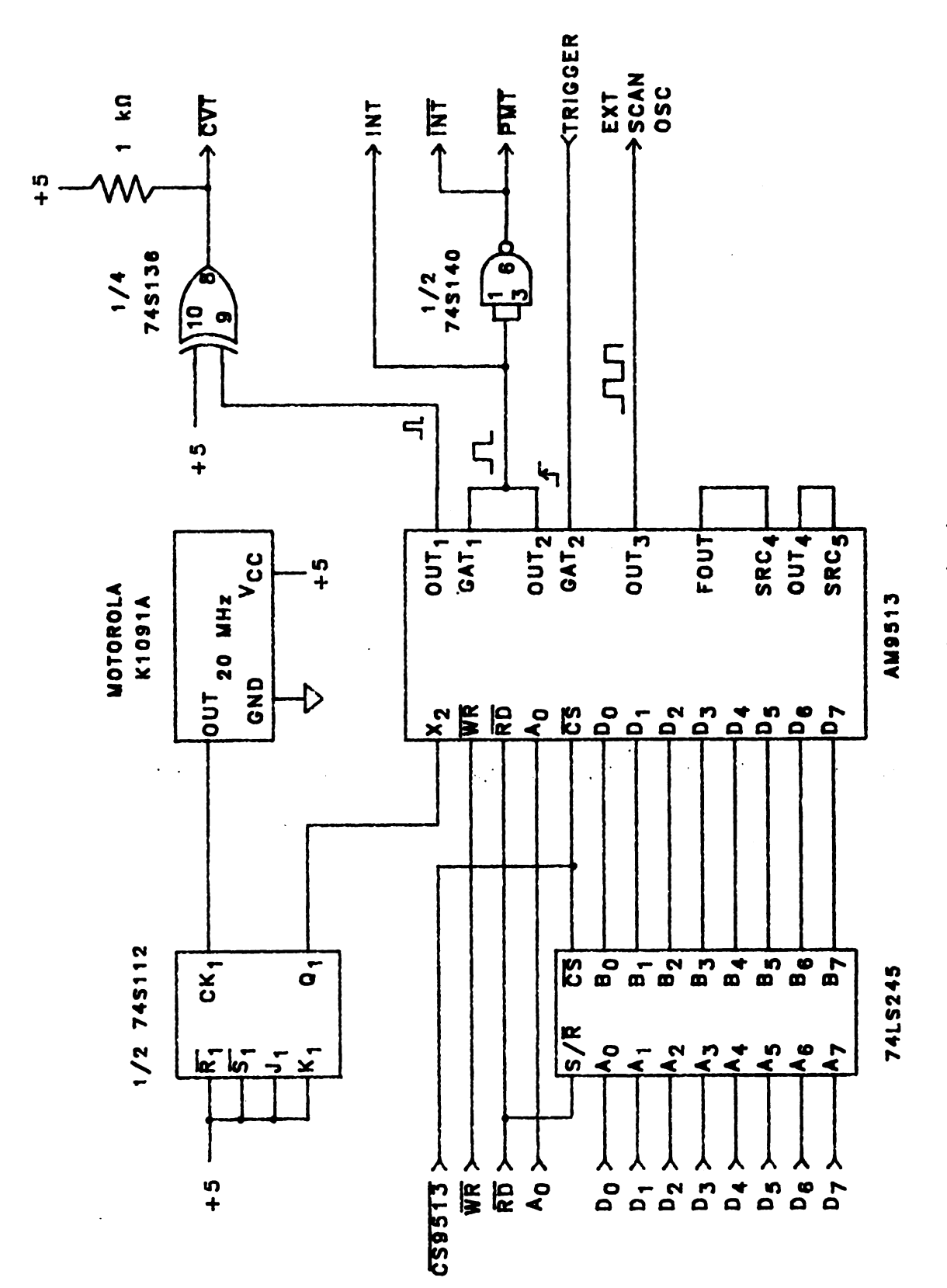


Figure 4-6 Timer Circuit

2 is configured in "Mode L" and controls the delay and integrate times. Use of the 10 MHz clock frequency for the source frequency of the timer allows 0.1 µs resolution of measured intervals. As such, the delay and integrate times, specified in tenths of microseconds, are stored in the load and hold registers. Synchronization of timer triggering with spark ignition is accomplished by sensing the rising edge of the thyratron trigger module synchronization pulse output. Once the delay time elapses, the output of this timer toggles to a high logic level. This signal is passed through a 74S140 NAND line driver. The resultant active low signal enables the gated integrator and switches the photomultiplier tube to a high-gain state. Termination of the integrate time returns the output to a low state, which disables the integrator and returns the photomultiplier tube to a low-gain state. The falling edge of this output pulse is also used to trigger timer 1.

Timer 1 is also configured in "Mode L" and operates with a 10 MHz source clock. This timer provides a 12.8 µs setting time before a 500 ns start-of-convert pulse is sent to the analog-to-digital converter. Following inversion, the low logic level pulse is asserted on the $\overline{\text{CVT}}$ line to initiate conversion.

Timer 3 is configured in "Mode D" to act as a square wave generator. The pulse stream is used as the external scan rate input to the monochromator controller. A software-selected source frequency of either 1 kHz or 10 kHz allows generation of scan rates between 0.001 nm/sec and 2.55 nm/sec with a wavelength increment of 0.01 nm.

Counters 4 and 5 perform as the elapsed time clock for the data acquisition system. Counter 4 is configured in "Mode D". The FOUT divider supplies a 200 Hz source frequency for counter 4. A 4 Hz square wave is generated at the output by repetitively counting to 25 and selecting the terminal count

toggled output option. The output for counter 4 is used as the source for counter 5. Counter 5 is configured as a simple 16 bit counter in "Mode A". Since the input frequency 4 Hz, the accumulated count is simply the number of quarter seconds since timer initialization. At this rate, a total elapsed time is retrieved by issuing a SAVE command for counter 5. The SAVE command transfers the accumulated count from an internal register to the associated hold register without interruption of the counting process. A subsequent read from the hold register transfers the count to the microcomputer.

3. Analog Electronics

The analog circuitry presented in Figure 4-7 performs signal integration, amplification, and conversion to the digital domain. The three major sections of this cirucit are a gated integrator, a programmable gain amplifier, and an analog-to-digital converter.

a. Gated Integrator

An Evans Associates model 4130 gated integrator card performs integration of the photomultiplier signal. Two additional analog inputs are combined with the photomultiplier signal at the summing point of the integrator. A static offset control to set the zero point of the integrator is constructed from a variable voltage source present on the integrator card. The output of the voltage source is available at the V_X output of the card and is connected to the summing point through a $10 \mathrm{k}\Omega$ resistor. The second offset voltage is generated by one of the system digital-to-analog converters (DACs). The DAC output is connected to the summing point through a $33 \mathrm{k}\Omega$ resistor. This input is used as part of the background correction circuitry discussed in the next section.

In addition to the analog inputs, two TTL inputs are required to control

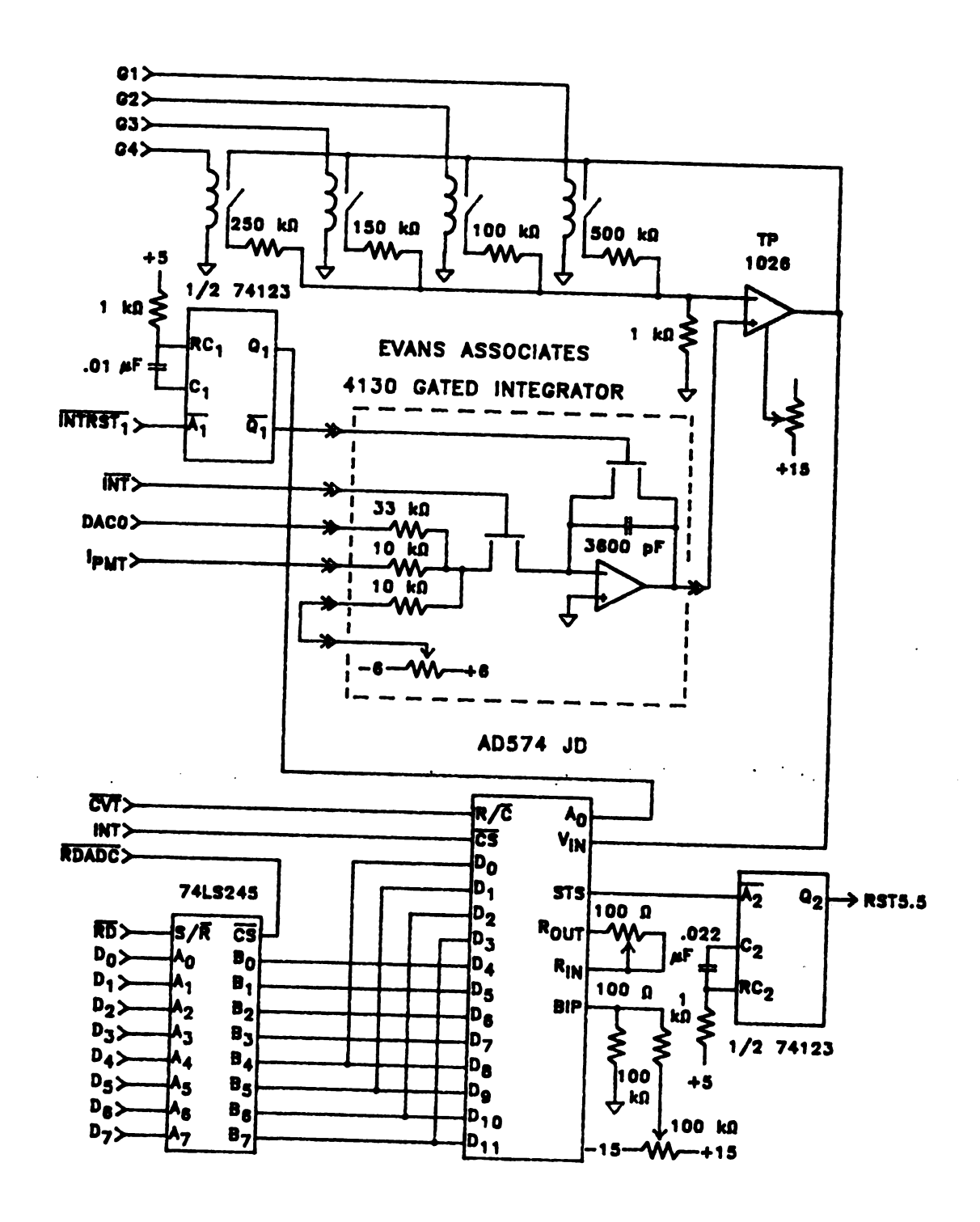


Figure 4-7 Analog Electronics

gating and to reset the integrator. Gating of the integrator is controlled by the active low $\overline{\text{INT}}$ signal generated in the timing circuitry. Integration continues for the duration fo the low pulse. This period is the integrate time. The integrator reset signal is an active low, 2.8 μs pulse derived from the Q₁ output of a 74123 monostable multivibrator. The monostable is triggered by a low pulse on the $\overline{\text{INTRST}_1}$ line. Since the $\overline{\text{INTRST}_1}$ pulse is generated in the device select logic, a software command is required to reset the integrator.

b. Baseline Subtraction Circuitry

In many circumstances, the background radiation signal was found to account for up to 75% of the usable dynamic range of the gated integrator. This was true particularly at high gain settings. To circumvent this problem, a baseline correction circuit was developed. Since the photomultiplier supplies electrons to the integrator, an electron drain or positive voltage source is required to counteract excessive background signal. In addition, for maximum usefulness, a wide range of voltages should be readily and rapidly available with the selected voltage based on the observed background signal. These features are obtained by using a digital-to-analog converter under microcomputer control. Since the microcomputer has access to the intensity level and the current gain setting, an appropriate offset value can be calculated and sent to the DAC. A $33k\Omega$ resistor is chosen to connect the DAC output to the integrator summing point; this provides offset capabilities over the entire integrator output range at all gain settings and integration times typically used.

c. Programmable Gain Amplifier

The programmable gain amplifier consists of four normally-open five volt relays (Magnecraft W107DIP-1), five precision resistors used for gain

determination, and a Teledyne Philbrick 1026 FET operational amplifier. The operational amplifier is wired as a voltage follower with gain. The noninverting input is connected directly to the output of the gated integrator and the inverting input is connected to ground through a $1k\Omega$ precision resistor. A feedback resistor connected between the inverting input and the output determines the gain associated with the circuit. Assertion of a high logic level on either the G1, G2, G3, or G4 inputs activates the corresponding relay and switches the appropriate resistor into the feedback loop. This effectively selects a specific gain. The device select logic assures that only one of the relays is activated at any one time. Reed relays are used in preference to other electrically controlled switching devices because there is no leakage current through the relay. A leakage current would divert some of the signal through each of the feedback resistors, and undesirably alters the gain characteristics of the circuit.

d. Analog-to-digital Converter Circuitry

Signal conversion to the digital domain is performed by an Analog Devices AD574JD analog-to-digital converter (ACD). Power supplies and offsets are wired according to manufacturer's specifications for operation in a unipolar, 0-10 V input mode (99). The analog input is connected directly to the output of the programmable gain amplifier.

Data conversion begins when both the \overline{CS} and the R/\overline{C} inputs are asserted low. This occurs following the settling delay at the end of the integration period. Connection of the \overline{CS} input to the INT line prevents conversion or data access from occurring during the integration period. Control over the conversion precision is governed by the state of the A_0 input. A 12-bit conversion occurs when the A_0 input is low. Since this input is connected to the Q output of the integrate reset monostable and the Q output is low

at this point in the acquisition process, a 12-bit conversion is performed. After the conversion is complete, the STS output line is asserted low. The high-to low transition of the STS output generates an end-of-convert interrupt on the RST5.5 microprocessor input. The interrupt is programmed to initiate a routine to access the digitized signal.

The microcomputer used here is an eight-bit machine; hence, two read operations are necessary to input all twelve bits of information from the ADC. The A_0 line controls what information is available on the ADC data bus. When A_0 is held low, the most significant eight bits are accessible; however, when a high logic level is asserted on A_0 , the four least significant bits are placed on the bus.

The ADC bus and the system bus are connected with a 74LS245 8-bit bus transceiver. Access of the entire 12-bit data word is accomplished in three steps. First, a one-byte read from the \overline{RDADC} address inputs the high eight bits. Following this read, a read or write operation must be performed to the $\overline{INTRST_1}$ address. This triggers the associated monostable to reinitialize the integrator and to assert a high logic level on the A_0 input. Finally, a second read from \overline{RDADC} transfers the low four bits to the microcomputer.

4. Photomultiplier Gate Circuit

Switching the photomultiplier from a low-to a high-gain state is required in the data acquisition scheme to protect the photomultiplier from saturation during the initial intense continuum emission generated by the spark discharge. The high-speed photomultiplier gate circuit used is identical to that described by Calkin (4) and is shown in Figure 4-8. In normal operation, a small potential difference, approximately 20 V, is maintained across the third and fourth dynodes. This keeps the photomultiplier in a low-gain state. A low pulse on the PMT line switches the photomultiplier to the high-gain state by applying

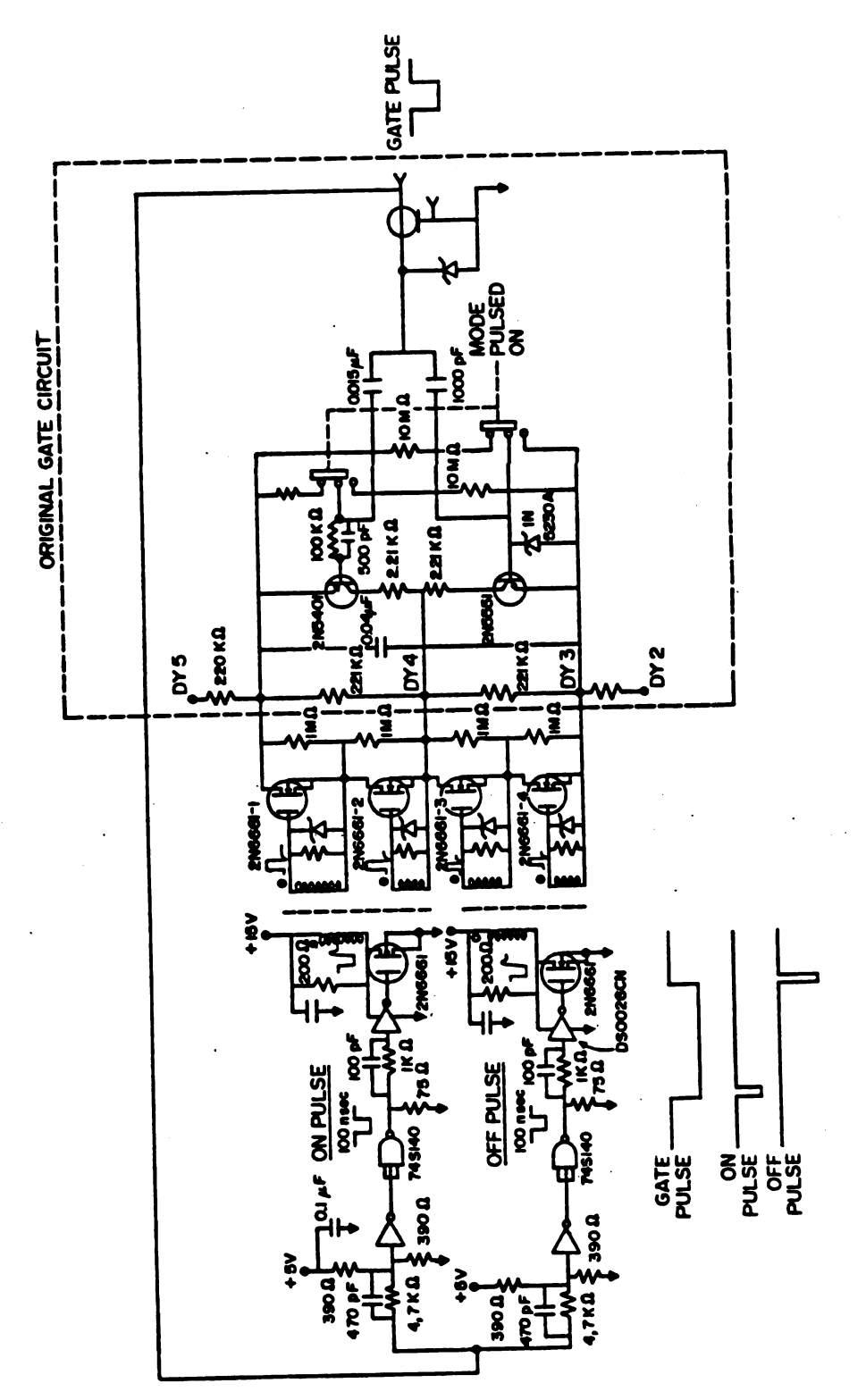


Figure 4-8 Photomultiplier Gate Circuit

80 to 100 V across the dynode pair. The rising edge of the PMT pulse returns the photomultiplier to the low gain state. Switching times of approximately 30 ns are reported with this gate circuit (4).

D. Monochromator controller/microcomputer interface

In the data acquisition process for any spectroscopic technique, information concerning the identity of the sample is encoded by optical signals at specific wavelengths; therefore, the capability for accurate mechanical selection of the appropriate wavelength is an important criterion in the design of a spectroscopic instrument. Wavelength selection with the GCA-McPherson EU-700 series monochromator and controller was manually performed by slewing to within a few nm of the desired location and then scanning slowly to the final wavelength. Unfortunately, due to electrical and mechanical shortcomings in the original design, final wavelength selection often became a matter of trial and error. To alleviate this deficiency, the microcomputer interface to the monochromator controller, shown in Figure 4-9, was designed.

The interface provides microcomputer access to the current wavelength setting and control of slewing and scanning operations. Communication between the microcomputer and the interface is performed with the INTEL 8255 programmable input/output circuit. This provides three, eight-bit ports. Port A is not used in this application. Port B is used as a bidirectional data bus between the microcomputer and the interface. The low three bits of port C select the interface function to be performed, either a wavelength read, or, initiation or termination of a scan or slew operation. External control of the scan rate is accomplished with one output of the AM9513 timer.

In normal operation, a zero is written to port C, which causes the $\overline{0}$ output of the 74LS138 3-to-8 decoder to go low. The signal is inverted and connected

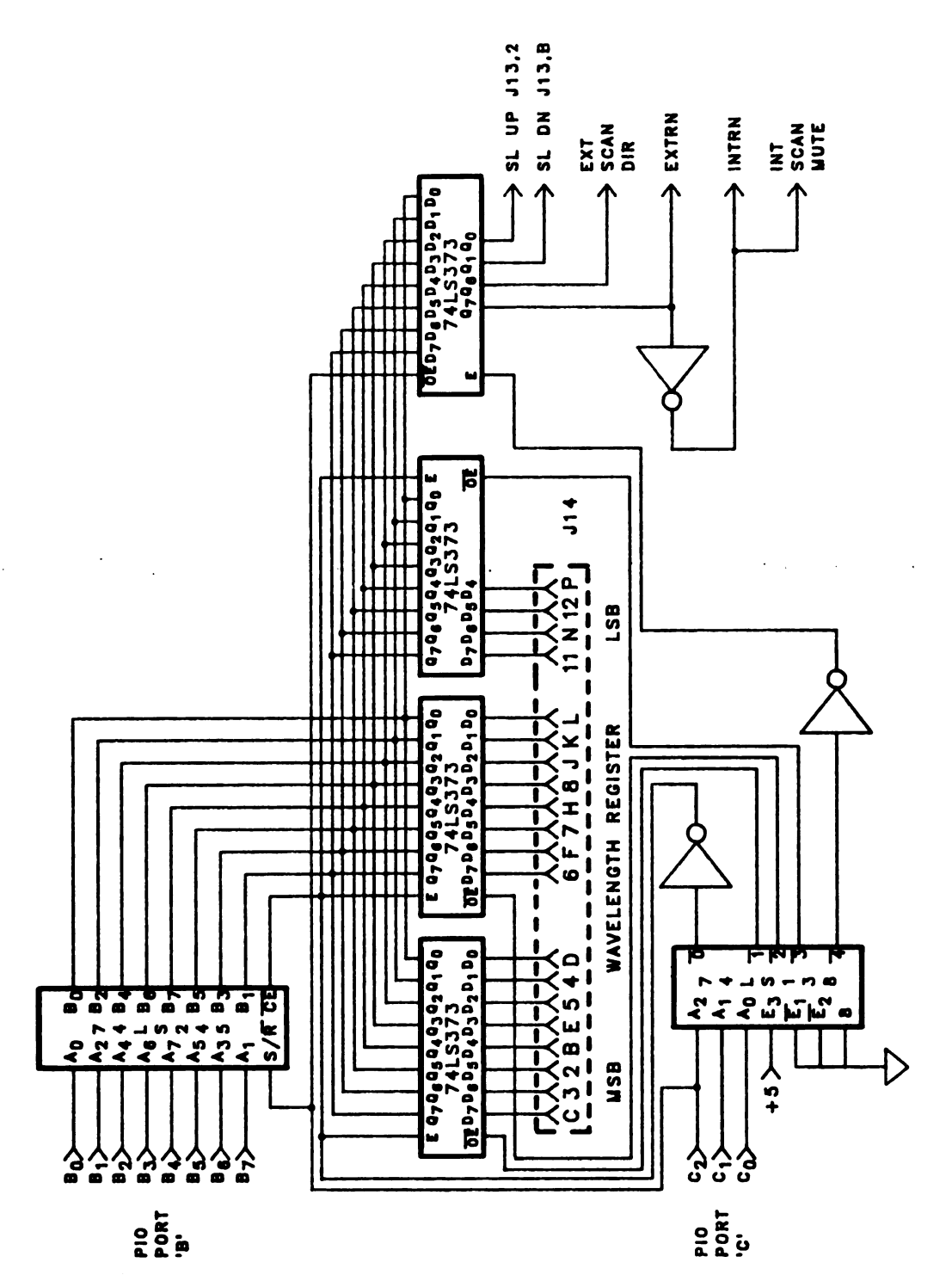


Figure 4-9 Microcomputer/Monochromator Interface

to the $\overline{\text{CS}}$ input of the 74LS245 bus transceiver and the E inputs of the three 74LS373 wavelength latches. This disables the line transceiver and enables the latches to track the current wavelength. The data inputs of these latches are connected to the binary-coded-decimal wavelength signals available in the controller at J14 (100). To accommodate the eight-bit architecture, the five-digit wavelength must be read in three operations. Writing a nonzero value to port C latches the wavelength latches and selects the line transceiver. The state of bit C_2 determines the direction of data transfer, i.e. a low level on C₂ causes data to be transferred from the interface to port B, and a high level reverses the data flow. Writing the value 1 to port C causes the $\overline{1}$ output to attain a low level. This enables the output of the latch which holds the two most significant wavelength digits. The information is then transferred from the latch through the transceiver to the port B inputs, from which a read operation is performed. The next two digits and the final digit are read with the same process, except the values 2 and 3 are written to port C, respectively. Following the complete wavelength transfer, the value 0 is written to port C to return the interface to the monitor level.

To initiate scan or slew commands, data must be transferred from port B to the 74LS373 command latch. This requires port B to be reconfigured via software as an output port. The appropriate command is then written to port B. Writing the value 4 to port C generates a low signal on the $\overline{4}$ output of the 74LS138 three-to-eight decoder. This changes the direction of the bus transceiver and disables the output of the control latch. The $\overline{4}$ output is inverted to enable data tracking on the control latch. Writing the value 5 to port C maintains valid data on the interface bus and latches the control latch. Writing a zero to port C enables the control latch outputs and reinstates wavelength tracking.

The valid monochromator functions controllable with the interface are scanning or slewing in either direction. As purchased, the controller included the logic circuitry required for external control of these functions; however, to permit microcomputer selection of the function, three connections had to be broken. These were the INTRN and EXTRN lines from the hardwired internal/external switch and a direction sense line originating on the front panel and accessible at J13 pin 5 (97). All modifications of the original design were performed on the wavelength circuit board. Manual monochromator control with the front panel switches on the controller is possible, provided in INTRN line is not asserted low.

Microcomputer control of the INTRN and EXTRN signals is provided by the Q_7 output of the control latch. A high Q_7 output asserts the EXTRN line high and the INTRN line low, which selects external monochromator control and inhibits manual operation. Scan direction is determined by the state of the Q_6 output, such that a high level selects a scan to longer wavelengths. Assertion of the Q_0 or Q_1 control bits to a high level initiates a slew command to longer or shorter wavelengths, respectively. Assertion of both bits inhibits all slewing. Since the command is latched, microcomputer intervention is required to terminate a scanning or slewing operation. A summary of inputs required for interface operation is presented in Table 4-1.

Minor modifications were made to the monochromator circuitry to minimize the detrimental effects of radio frequency interference and random voltage spikes associated with spark ignition. These effects included loss of correlation between the actual wavelength and that determined by the monochromator controller and unsolicited activation of the scan stepper motors. Four 0.1 μF ceramic disk capacitors were placed between ground

Table 4-1.

Monochromator Controller Interface Commands

$\begin{array}{ccc} B & & Result \\ O_3D_2D_1D_0 & & & \end{array}$		x x y y Computer control	x x 0 1 Slew up	x x 1 0 Slew down	x x y y Scan down *	x x y y Scan up *	x x y y Manual control	above Latch command
Port C $D_2D_1D_0$ $D_7D_6D_5D_4D_3D_2D_1D_0$		0 0 0 0 0 0 0 0 0 0 0 0 0 0 0 0 0 0 0 0	0 0 0 0 0 0 0 0 0 0 0 0 0 0 0 0 0 0 0 0	1 0 0 0 x x x x 1	1 0 0 0 x x x x y	1 0 0 0 1 x x x x y	1 0 0 1 x x x x y	1 0 1 same as above
PIO Command Port (octal)	Control Functions:	200	200	200	200	200	200	200

Table 4-1 cont.

PIO Command Port (octal)	Port C $D_2D_1D_0$	Port B $\mathrm{D_7D_6D_5D_4D_3D_2D_1D_0}$	Result
Wavelength input:			
202	0 0 0	none	Idle, no transfer
202	0 0 1	-1st2nd-	High 2 digits
202	0 1 0	-3rd4th	Middle 2 digits
202	0 1 1	-5th-	Lowest digit
x ==> either logic level	level		

must have externally applied scan rate

must be same logic level as other 'y'

y ==>

^== *

and the four stepper motor drive lines on the wavelength circuit board. This largely eliminated activation of the stepper motors due to electical noise. To minimize problems with wavelength synchronization, two 0.03 μ F capacitors were placed between ground and the ϕ_A and ϕ_B outputs of the wavelength encoder. Installation of capacitors larger than 0.03 μ F caused valid encoder pulses to fail to trigger the wavelength counters; hence, synchronization was again lost. In addition, a 1.0 μ F tantalum capacitor was installed between ground and the five volt supply used by the encoder to further minimize false triggering of the wavelength monitoring circuitry.

These steps significantly improved the noise immunity; however, during periods of extremely high interference, wavelength synchronization was still lost.

E. Spark Detection Circuit

The synchronization pulse output by the thyratron trigger initiates the data acquisition process; therefore, it is necessary to know the timing relationship between the trigger pulse and actual spark ignition. A photodiode trigger circuit similar to one designed by Seng (107) was used to detect spark ignition. The photodiode circuit is shown in Figure 4-10. The only modification to Seng's design is the omission of a 4.7 k Ω resistor (bold face in the figure) connected between the photodiode anode and ground. Removal of the resistor increases circuit sensitivity and improves the fall time when light strikes the photodiode. An increase in the rise time is also observed; however, since the spark ignition time is of interest, the rise time is not important in this measurement. In operation, fall times of less than 50 ns were observed.

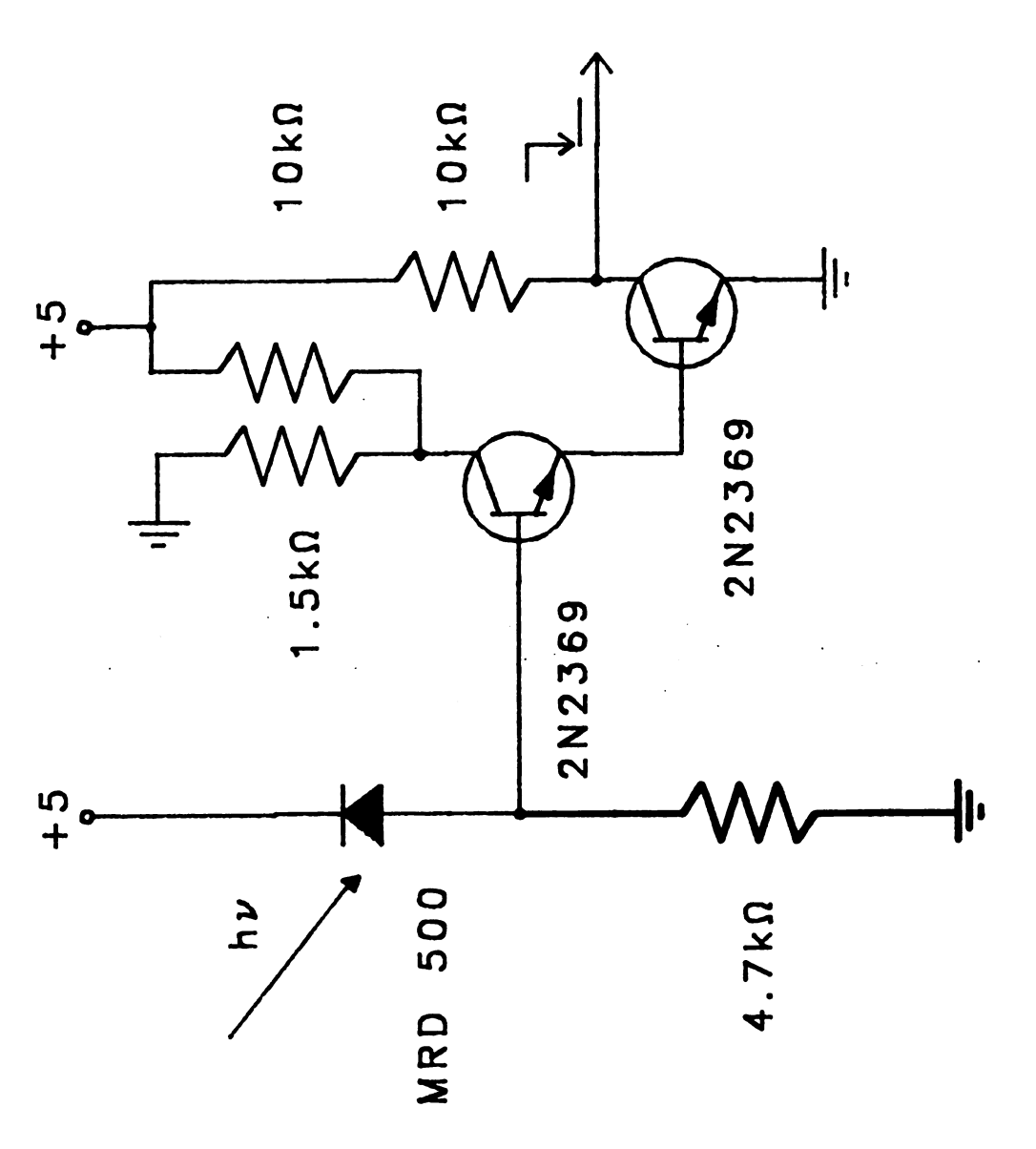


Figure 4-10 Photodiode Trigger Circuit

CHAPTER V

Software

Microcomputer control of instrumentation is a rapidly growing, beneficial process applicable in many areas. Benefits include the rapid synchronization of the many small tasks required for data acquisition, transferral of data between different computer facilities to exploit various capabilities of the different machines, and immediate archival data storage. In addition, microcomputer control permits the incorporation of increased versatility into the acquisition process as the need arises, without necessitating a redesign of the entire system.

Selection of a programming language is based on several considerations associated with the particular application such as, the available memory, the required computation speed and power, and the overall complexity of the control process. Often, the basic instrumental control process requires the repeated manipulation of several parameters and fundamental operations in an identical manner. More complex control structures incorporate several of the fundamental routines in a precise sequence. The function of the software used for a given application is to provide for the development of fundamental acquisition and control routines, and allow development of higher level control structures by linking the fundamental routines in a logical,

useful order. To perform these operations, mechanisms for editing and compiling are required. Instrument control operations are most conveniently performed from the lowest programming level, assembly language; however, data manipulation and process coordination are more conveniently and understandably implemented with a higher level programming language. Thus, the ideal interface control language should provide mechanisms for combining assembly language routines into the higher level programming language programs.

Two languages were available for the microcomputer used here, SLOPS and FORTH. SLOPS or Structured Library Oriented Programming System as developed by Gregg (101) is an assembly language based package. It consists of a set of user-callable subroutines to perform general functions such as multiplication, division, character input, and conversion. Although this vastly simplified coding assembly language acquisition routines, no compilation or editing capabilities were available on the microcomputer. Therefore, program development and compilation were performed on the LSI-11/23 minicomputer and downloaded to the microcomputer. When this procedure was used, program development was a time consuming, error prone, and often futile process. In addition, since all routines had to be written in assembly language, highly versatile programs required long development times. These factors made SLOPS a less than ideal language for this application.

The second language available was FORTH, which offered many advantages over SLOPS. The FORTH installation used is similar to that described by Brodie (102). The base level of FORTH includes a line editor and compiler. This allows program development to be performed on the microcomputer and eliminates the time consuming compilation and

downloading steps required in SLOPS. As a consequence of FORTH's structure, assembly language routines or "words" are easily incorporated into high level FORTH words. This ability makes FORTH an excellent choice for instrumental control operations. Additional benefits derived from FORTH include: double-precision integer math, a multiple-buffer block input/output structure for data transfer, multitasking capabilities, and a threaded programming structure. These features are all exploited in the data acquisition software.

This chapter describes the data acquisition software used on the microcomputer. The programs used to massage the data and convert it to plottable form are also discussed.

A. Data Acquisition Software

The software controlling the acquisition process is hierarchically arranged as shown in Figure 5-1. In this organizational scheme, a menu-drive, monitor routine running as a foreground task, is the general user interface to all levels of the system. All hardware and software acquisition parameters, the monochromator interface commands, and file handling routines are accessed from this level.

The menu organization implements two important features. First, any table entry can be accessed with a single keystroke, and second, a prompt screen that describes all options available on the current page is listed. These features make option selection a quick and easy procedure, minimize the amount of memorization of word names required, and decreases the time required to optimize the system parameters during a particular experiment.

The four, twenty-six entry menu tables shown in Table 5-1 allow selection

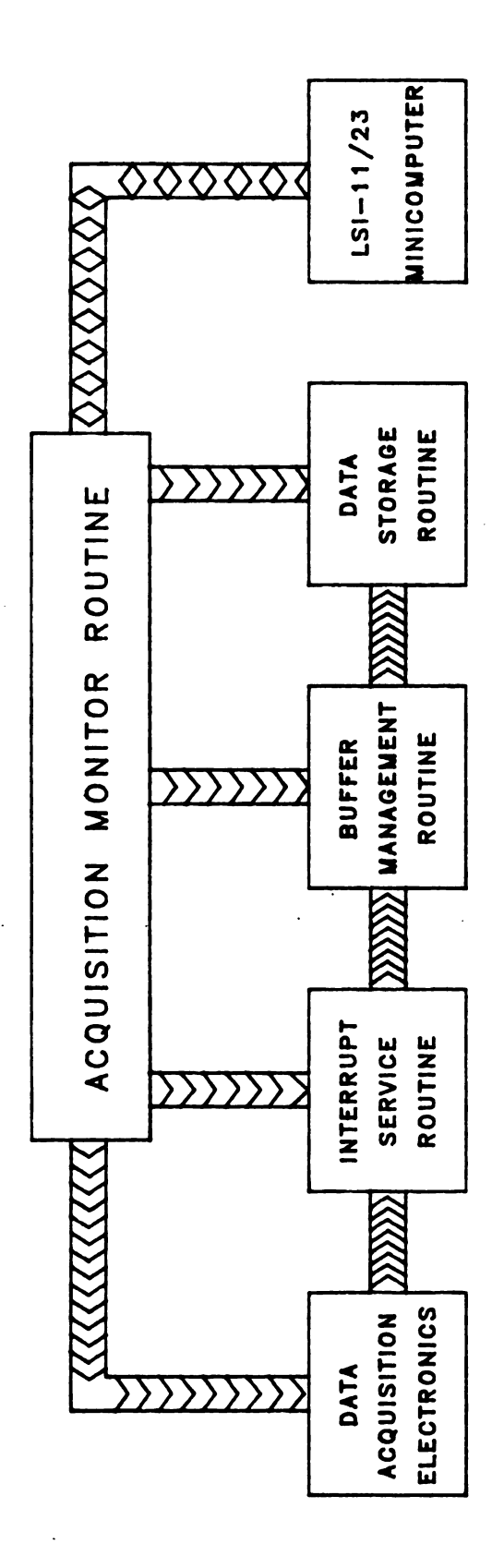


Figure 5-1 Data Acquisition Software Organization

Table 5-1.

Available Acquisition Options

Table	1	2	3	4
Key				
Α	DTBL	SPKPTS	?AVER	AVING
В		BSSET	!BKGND	BSSET
C	CHOOSE	CHOOSE	CHOOSE	CHOOSE
D	DIR	*DLY		DSCAN
E	GTBL	GTBL	GTBL	GTBL
F	FILSAV	FINDPEAK	FINDPEAK	
G	GTBL	GAIN	!PEAKVALUE	
Н	VHD	OBSL	-BKGND	OBSL
I	DDISK-INIT	*ISET		
J		FSTART		
K	VDEL	FSTOP		
L	?LINE	?LINE	?LINE	?LINE
M	MONO	MASK		SCANINC
N	NEWWAVE	CVT	CVT	CVT
О	23LINE	GWATCH		
P	LTBL	PARAMS	PARAMS	PARAMS
Q	GTBL	ABRTRN	ABRTRN	ABRTRN
R	\$DAC	RPAVG	RPT	RPT
S	STBL	ETBL	ETBL	ETBL
Т	TALK	TAKE	TAKE	\$DAC

Table 5-1 cont.

Table	1	2	3	4
Key				
U	HCOPY	UNMASK		
V		>3TBL	>2TBL	
W	>LAMDA	>LAMDA	>LAMDA	>LAMDA
X	>3TBL	TPTS	SVLINE	CNCN
Y	>2TBL	?>1TBL	>2TBL	?>3TBL
Z	>2TBL	>3TBL	?>4TBL	

of options from three major categories. These are microcomputer support functions, general acquisition parameter control functions, and specialized acquisition routines. The first menu consists of routines for disk drive control and communication between the microcomputer and the minicomputer. In the second and third menus, a generalized acquisition routine can be selected. While the experiment is in progress, the user, by appropriate option selection, can modify any experimental parameter, such as delay or integrate times, and can observe the effect of that modification immediately. This greatly simplifies optimization of experimental conditions. The specialized acquisition routines available in the fourth menu are designed to record the effect of a single variable on an observed emission intensity. This is accomplished by synchronizing the change of the parameter with the acquisition of a number of data points. The value of the variable, the average emission intensity, and the standard deviation of the emission are then saved as an X, Y, Z triplet for later analysis. Synchronous delay time, integrate time, or wavelength scans are examples of routines available in this category.

The three control routines which perform the acquisition and data storage process for all acquisition are the interrupt service, buffer management, and data storage routines. The net effect of the three routines is the acquisition of individual emission intensities, followed by the storage of average intensity data to flexible disk media. Since these are interrupt driven routings and background tasks, the monitor routine can be executed concurrently to allow user interaction at any point in the acquisition process.

B. Interrupt Service Routine

The RST5.5 microprocessor interrupt input is triggered by the end-of-convert pulse. When enabled and unmasked, the RST5.5 signal initiates

the execution of the interrupt service routine diagrammed in Figure 5-2. Upon execution, the 12-bit digital value representing the intensity is read from the analog-to-digital converter and summed into a grand sum. the interrupt routine then terminates, and returns control to the monitor task. After a user-selected number of spark intensities are acquired in this manner, the interrupt routine resumes the buffer management background task. The buffer full flag is then checked. If the buffer is marked as full, the data storage background routine is resumed. Following this, control returns to the monitor routine.

C. Buffer Management Routine

The buffer management routine controls the data buffer filling process and normal run termination procedures. The flowchart shown in Figure 5-3 depicts the buffer management background task. Upon initialization, the average intensity of the grand sum for the selected number of points is calculated. If appropriate, this value is sent to the DAC controlling the strip chart recorder. The 12-bit average is then stored in one of the two disk buffers available in FORTH. When only six bytes remain in the current buffer, the elapsed time and current wavelength are read from the elapsed time clock and monochromator interface. These values are then saved as the last six bytes in the data buffer, and the buffer full flag is set. Run termination conditions are checked. If no termination condition exists, the buffer management routine exits. When a termination condition is met, the run-in-progress flag is cleared, all active data buffers and current run parameters are saved to disk, and the disk directory block is updated to reflect the presence of another data file. Finally, the flags indicating an active background task are cleared to prevent inadvertent corruption of

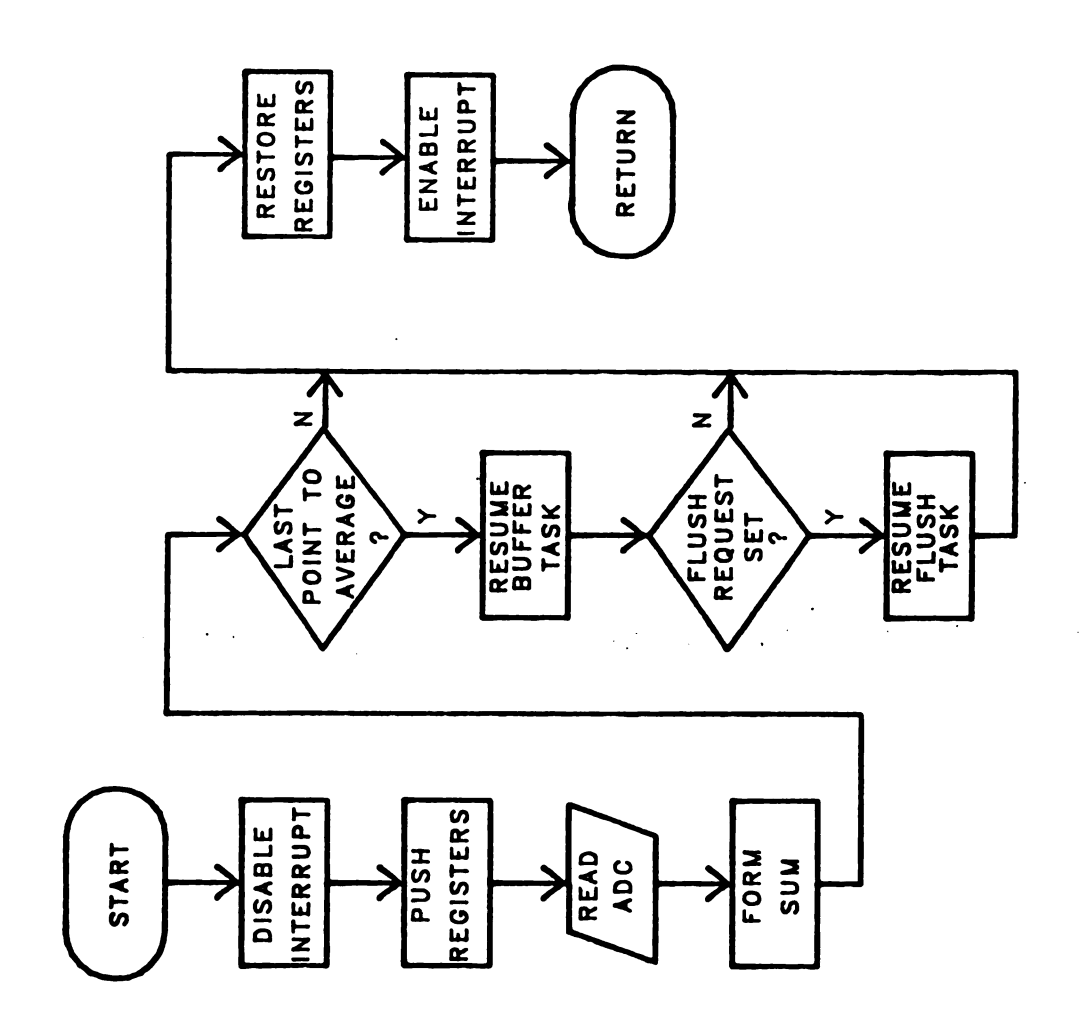


Figure 5-2 Flow Chart for Interrupt Service Routine

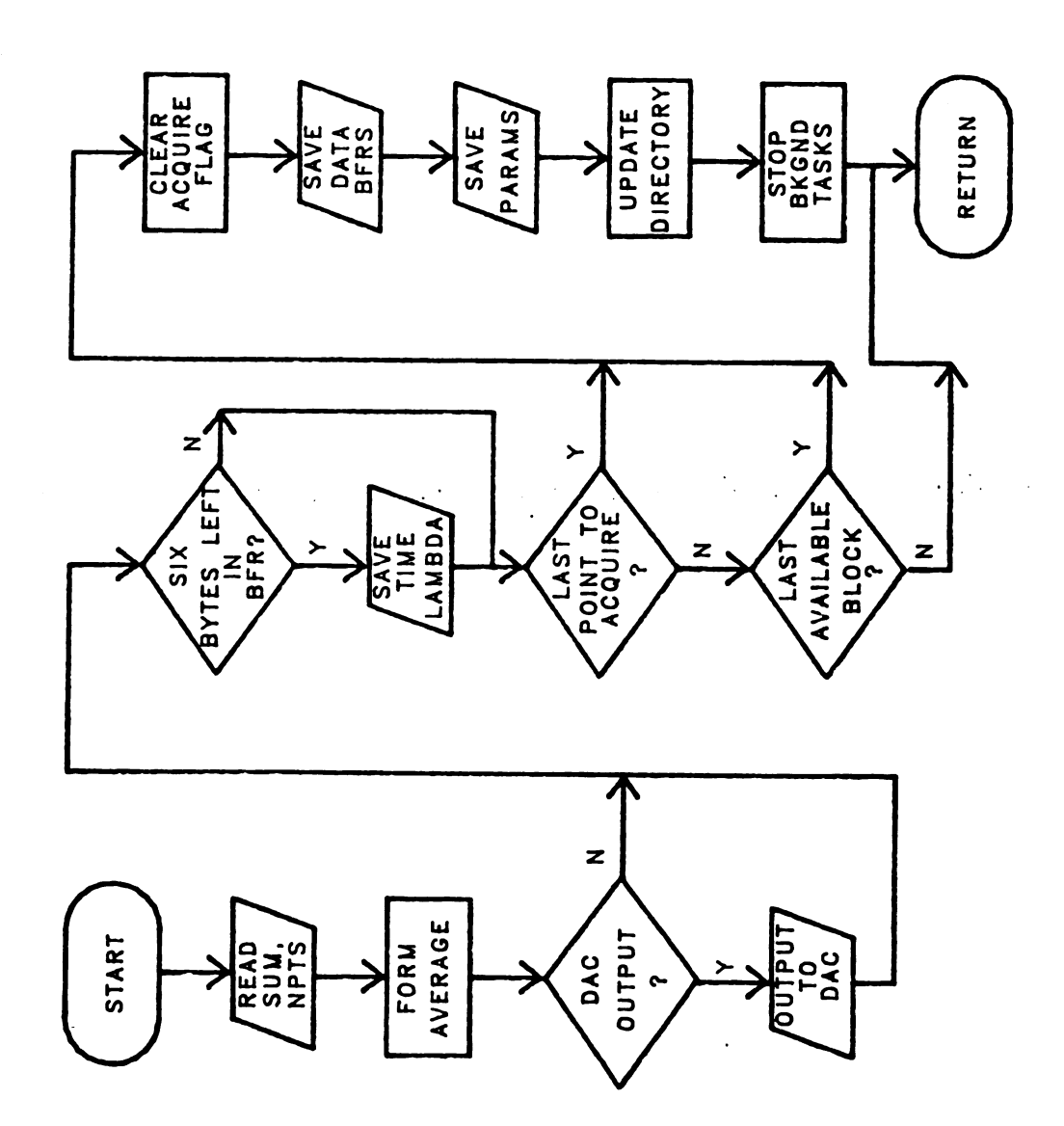


Figure 5-3 Flow Chart for Buffer Management Routine

the disk buffers, and the buffer management routine exists.

D. Data Storage Routine

The data storage background task diagrammed in Figure 5-4 correctly identifies a data buffer for disk storage and executes the FORTH buffer storage routine. To avoid corruption of the disk as a result of unintentional execution of this task, a task-active flag, which is set at the beginning of an experiment, is used. A second flag is set only while the disk save routine is active. After this task exits, control is returned to the monitor routine.

The disk routine has complete control of the microprocessor while information is transferred to disk; therefore, the RST5.5 interrupt must be disabled at this point in the acquisition scheme. This results in the loss of one to five data points whenever the disk routine is executed; the exact number lost depends on the particular disk interleave used. Interleave values of four, five, or six give the fastest block access times on this system and result in the fewest number of lost data points. Since each block contains approximately 500 data points and an acquisition rate of two points per second is obtained, one data point is lost every four minutes.

E. Data Disk Organization

On run termination, all emission data are saved to disk. In addition, a parameter block containing all microprocessor-controlled variables, an eighty character run descriptor, and a time stamp corresponding to the start of the experiment are saved. Information which selects default data conversion parameters, for use on the minicomputer, is also contained in this block.

One of the major drawbacks to using the FORTH programming language

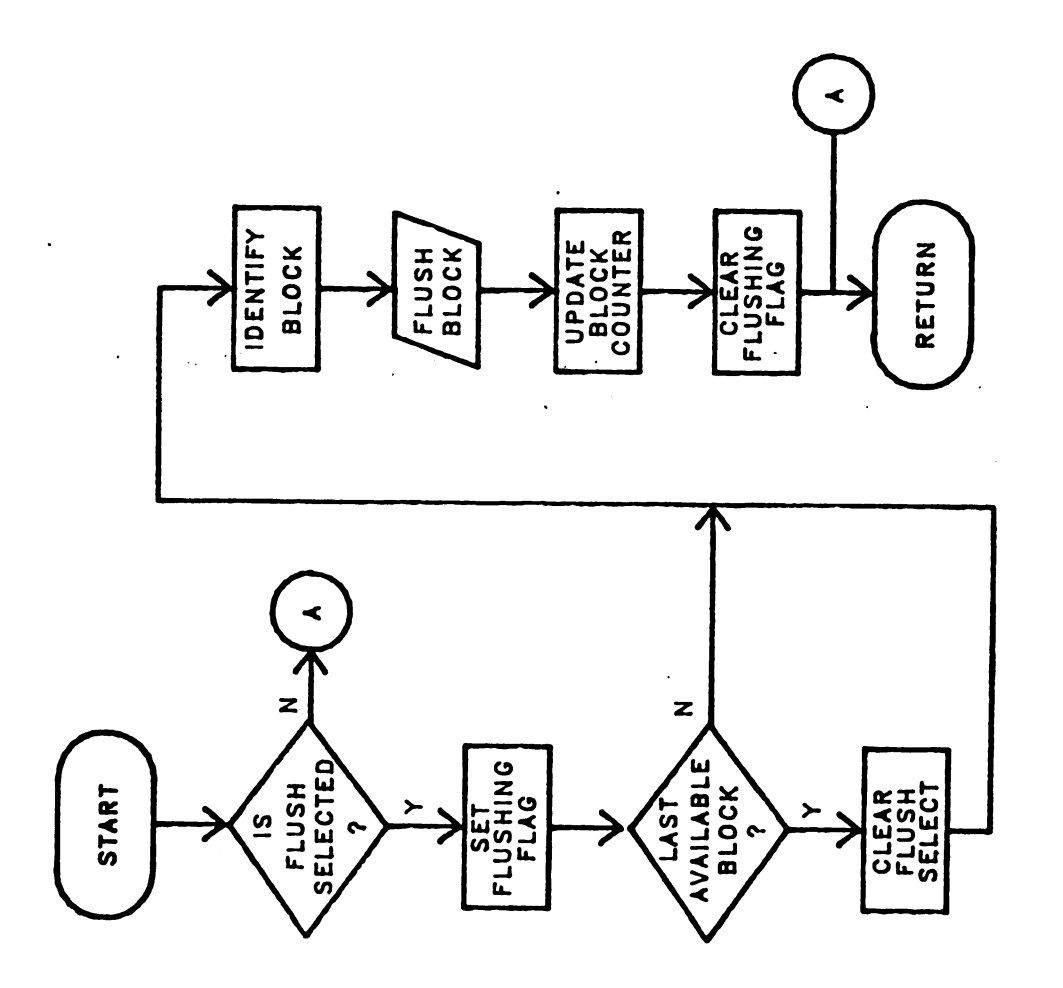


Figure 5-4 Flow Chart for Buffer Flushing Routine

for data acquisition is that by design, all data and software are saved in blocks with no file based organization system; this requires the user to keep track of where information is stored manually. The lack of file structure is a particularly serious problem with data storage, since very little text is present with which to identify related blocks of data and/or experiments. To alleviate this deficiency, a simple file structure for the data storage disk was developed. In this protocol, the second block on a data disk is reserved for directory information, which consists of the total number of blocks used, the number of experiments currently saved on the disk, and a directory entry for each experiment saved. The directory entry includes a nine character file name and the first and last block numbers of blocks which contain data from the corresponding experiment. A maximum of sixty directory entries per data disk are permitted. In addition, the ability to interpret and display the parameter block for an experiment is available. The incorporation of these and similar disk-based routines makes the current system very amenable for use as an immediate archival storage and retrieval method.

F. Minicomputer Programming Language Selection

Since the microcomputer system used does not support any hard copy devices and high level, floating-point operations are difficult to perform using the integer math functions available in the FORTH programming language, data transfer to the LSI-11/23 minicomputer, where these capabilities exist, was required. At this level, hardcopy printouts, high-level computation procedures, and a versatile data plotting program are available.

The ideal programming language for the conversion process should have several critical capabilities, including: floating-point calculation, disk file access, high computation speed, and the ability to execute without repeated

user interaction. The choice of a suitable programming language on the minicomputer was limited to BASIC, FORTH, FORTRAN-77, and MACRO-11. BASIC, although versatile and easily programmed, was judged to be too slow for the high volume of data associated with a typical experiment. The version of FORTH available on the minicomputer did not offer the floating-point math functions required for statistical treatment of the data; hence, FORTH was unsuitable at this level. MACRO-11, the LSI-11/23 assembly language, offers access to all system routines. This includes floating-point capabilities; however, user access to the routines from MACRO-11 is a tedious, error-prone programming exercise. FORTRAN-77 offers all of the features required of the conversion programming language and was chosen to perform all data manipulations.

One weak point of FORTRAN-77 was that user interaction was typically required for entry of several data manipulation parameters. One approach to overcoming this difficulty is to access the command line used to initiate the conversion software. The FORTRAN routines available to access this information are awkward and difficult to use. MACRO-11 supports relatively easy-to-use routines which access and parse the command line; hence, a MACRO-11 subroutine was written to perform this function. Since the MACRO subroutine uses the system routines for parsing the command line, input of filenames and options conforms to the command line standards established for the operating system. This feature allows specification of all data conversion options on a single line. Furthermore, this line can be specified in a command file to allow unsupervised conversion to occur. Because command lines to initiate all programs associated with the data conversion and plotting routines are included, the user simply starts the process and is free from the tedium of waiting for the conversion to terminate.

The user has an option to specify that the entire process be run when computer usage is normally low so that the computer is free for user intensive tasks such as editing and program development.

1. CVT - Data Conversion Software

After experimental data are transferred to the minicomputer, they are converted into a form readable by the plotting package available. In addition, several options exist which select specific, nondefault conversion conditions, display experimental parameters and statistics, and enhance the resultant plot. All options are accessible via the initial command line and are selected by the inclusion of a two character mnemonic. Input and output file specifiers are also entered in the command line; hence, all data manipulation parameters are selected on the single line used to initiate the conversion program.

Data files present on the minicomputer are of two major types. The simpler of the two contains an experimental parameter block followed by data blocks. Each data block contains 509 intensity values followed by the wavelength setting and elapsed time associated with the last intensity value. Enough data blocks are present to contain the entire experiment. This type of data file is generated when the general acquisition routine is used and does not allow for synchronization between data acquisition and variation of a specific experimental parameter. The more complex data structure also consists of the parameter block and data blocks; however, a specific value for the abscissa and the standard deviation associated with each intensity value are present. A synchronized acquisition run, such as a delay or monochromator scan experiment, generates this type of data file.

The parameter block contains data descriptor information used by the

conversion routine to select the default conversion modes most appropriate for the particular experiment stored in the data file; this allows for relatively simple user interaction with the data manipulation software. The data descriptor section indicates whether the file consists of intensity data only or synchronously acquired data, the total number of data sets present, and the length in bytes of each data set. In addition, flags indicating the appropriateness of standard deviation or pooled standard deviation calculations exist in the data descriptor. The parameter block also contains the specific experimental parameters existent during the experiment; these include, delay and integrate times, the initial wavelength, the number of sparks averaged per point, and the gain used for the experiment. This information is displayed on the user's terminal and optionally printed on the line printer to permit complete, rapid experimental identification.

Manual override of the default conversion parameters is accomplished by specifying the desired option in the command line. Other options available include: abscissa selection, description of an appropriate output window, baseline substraction, and inclusion of standard deviation calculations. After the data conversion process was completed, the data sets were displayed by the MULPLT plotting program written by Atkinson (103). Hardcopy plots of the data were obtained at this level.

CHAPTER VI

SPARK SOURCE CHARACTERIZATION

The transient nature of the spark discharge requires the use of time-resolved spectroscopy for discharge characterization. Previous work on a similar spark discharge in argon has shown that the plasma is initiated by the ionization of metastable argon atoms (104). Earlier studies of similar spark discharge designs indicated that the spectroscopically useful time window existed on the microsecond time scale after the cessation of current through the plasma. Therefore, optical and electrical characterization of the discharge were performed on the microsecond time scale.

Since the thyratron trigger synchronization pulse was used to initiate the data acquisition process, the timing relationship between the leading edge of the trigger pulse and actual spark ignition was determined. To determine spark ignition, the output of the photodiode circuit (see Chapter III) was monitored with a Tektronics 5403 single beam oscilloscope equipped with a 5A48 dual trace module and 5B42 time base.

A minimum lag time of approximately 0.3 µs exists for all gap lengths studied. In addition, the charging voltage required to attain the minimum lag time increases slightly with increased gap length. These characteristics indicate the lag time consists of two components. The more significant

component determines the minimum observed lag time and arises from the thyratron breakdown time, the impedance characteristics of the high voltage connection between the spark cathode and the thyratron anode, and nonsimultaneous generation of the synchronization pulse and the thyratron grid pulse. Walters (104) has observed a similar, although shorter, lag time with his equipment and has found the lag time to be independent of anode voltage, but influenced by specific thyratron characteristics. One attribute affecting the lag time is the thyratron hydrogen pressure. Since the pressure decreases with extended use, the lag time is expected to increase with thyratron age. Other characteristics which affect the lag time include thyratron geometry, cathode voltage, and high voltage transmission line impedences.

The second factor determining the timing relationship between the synchronization pulse and the spark formation is the actual breakdown voltage of the spark gap. When a longer gap is used, a higher breakdown potential is obtained. Nasser (105) reported that the rate of gap breakdown is dependent on the amount of overvoltage across the gap. Hence, the longer gap length requires a greater amount of overvoltage to produce the same spark breakdown times. Two mechanisms are responsible for streamer formation and subsequent breakdown. Near the breakdown potential, a Townsend mechanism (105) is active. This requires the formation of a space charge region, followed by electron transfer from the cathode to the anode with subsequent streamer formation. This is a relatively slow process occurring on the microsecond time scale. At higher overvolt potentials, a "streamer mechanism" is present. In this mechanism, support gas ionization occurs near the anode. ionization process continues to self-propagate to subsequent layers of the support gas until a streamer extends to the cathode. At this point, the spark gap breaks down and the plasma is formed. At high overvoltage conditions, this mechanisms occurs in 0.01 microseconds (105), which is negligible in comparison to the constant lag time arising from the external electrical characteristics of the system.

In all experiments, the quoted delay time presented is relative to the trigger pulse.

A. Capacitor Charging Characteristics

In the early, free-running, double gap spark source design, the voltage across the analytical gap and, consequently, the energy available during the discharge, was determined by the breakdown potential of the control gap. Therefore, the repetition rate was a function of the charging time of the storage capacitor, which was determined by external factors such as charging voltage, the current limiting resistance, capacitance, and the longevity of conductive species in the spark gap. With the incorporation of the thyratron switch into the discharge circuit, a constant repetition rate is electronically generated and the charging time became independent of these factors. Under these constraints, the effective spark gap voltage is dependent on the time constant of the charging circuit and the repetition rate.

To obtain optimum performance, the energy dissipated in the spark should be as high as possible. Since the energy available for the discharge is proportional to the gap voltage, knowledge of the gap voltage is useful. The theoretical maximum for the gap voltage is derived from the calculated value of the charging time constant and the experimental repetition rate.

The equation for the capacitance of a cylindrical capacitor is

C = Elr/2d

where E, the dielectric constant, equals 2.26 for polyethylene, I is the length, r is the average radius, and d is the thickness of the dielectric. With this equation, a capacitance of the storage capacitor of 300 pF is found. This value, coupled with the current-limiting resistance, gives a time constant of 300 µs. Hence, a charging time of 690 µs, or a repetition rate of 1.5 kHz, is required to charge the capacitor to 90% of the available voltage. Although this constraint was recognized, a repetition rate of 2.2 kHz was generally used, since this frequency is more conveniently and consistently available from the thyratron trigger circuitry. Operation at this frequency corresponds to a maximum gap voltage which is 78% of the charging voltage. The calculated maximum and the observed gap voltage as a function of repetition rates are shown in Figure 6-1. The slight negative deviation from the theoretical maximum is probably caused by inaccuracies in the calculated values of the electrical components.

Figure 6-2 shows the relation between the repetition rate and the observed signal intensity for a 6000 V spark. The decreased signal intensity at increased repetition rates is caused by the decreased gap voltage associated with incomplete charging of the storage capacitor. The associated decrease in the overvoltage across the gap causes an increase in the trigger jitter of the spark. Since the slope of the charging curve is steeper at shorter charging times, trigger jitter causes a greater variation in the gap voltage at higher repetition rates and an increased noise in the observed signal intensity.

The effect of operation at higher charging voltages is an increase in the energy available for each spark. As shown in Figure 6-3, the signal

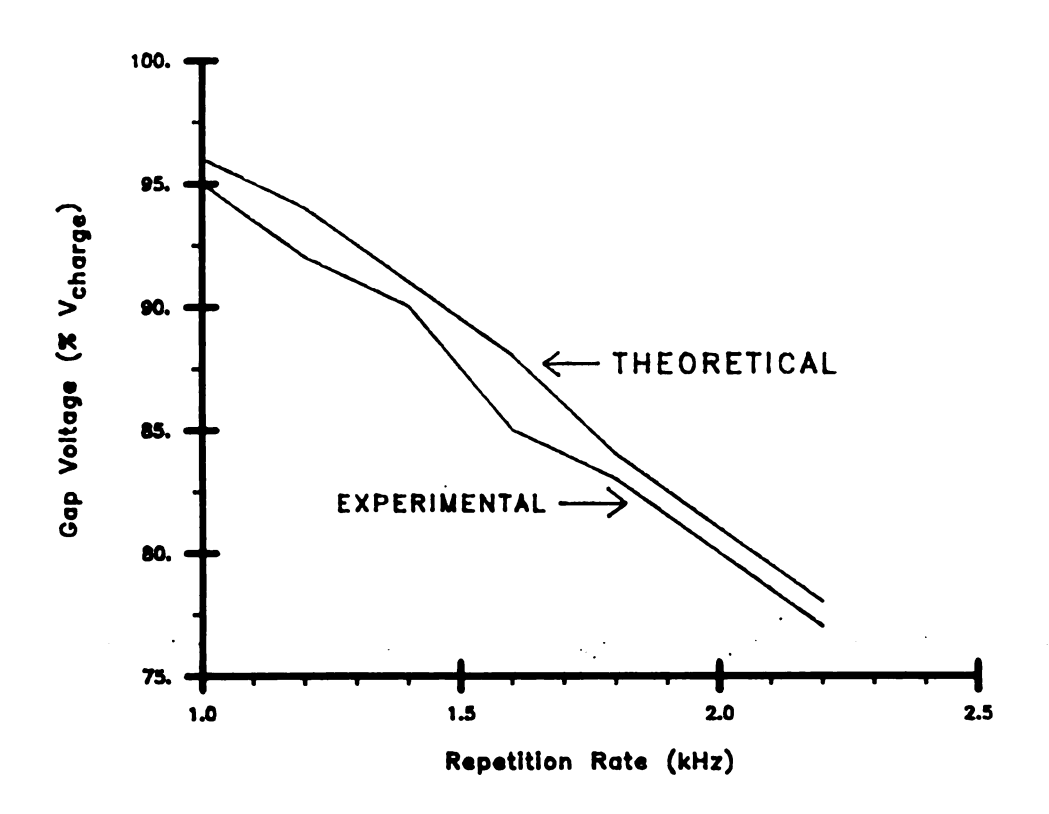


Figure 6-1 Gap Voltage as a Function of Repetition Rate

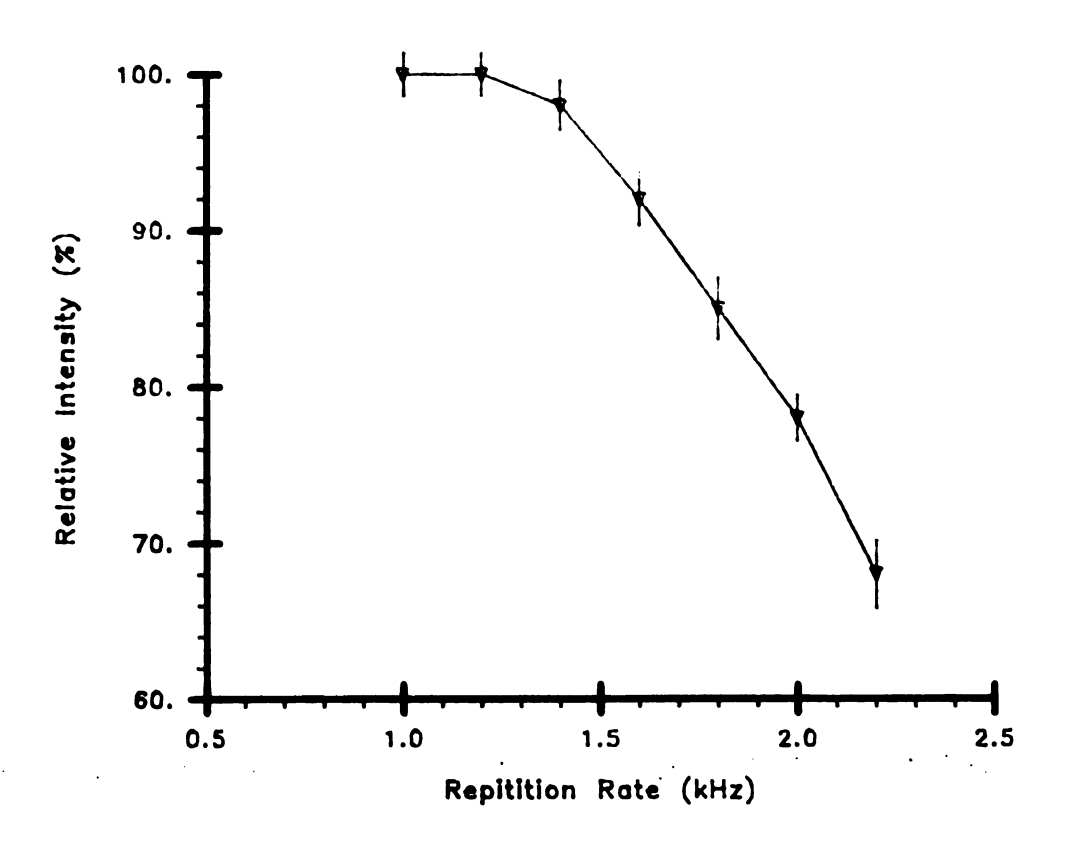


Figure 6-2
Relative Intensity as a Function of Repetition Rate

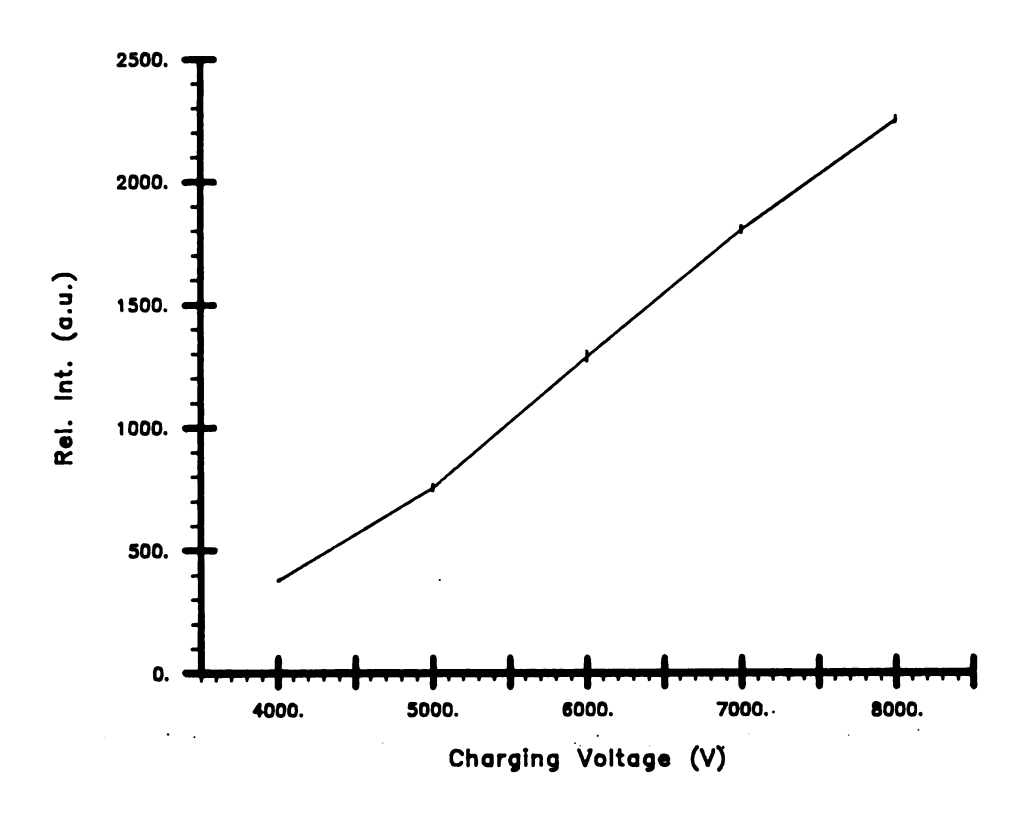


Figure 6-3 Relative Intensity as a Function of Charging Voltage

intensity is proportional to the charging voltage. In addition, a slight decrease in the noise level at 415 nm is observed at higher charging voltages. With the more energetic conditions, a higher overvoltage is present across the spark gap. Under these conditions, the spark fires more consistently relative to the trigger pulse; hence, the same time window is monitored by the acquisition electronics and a less noisy signal is obtained.

B. Effect of Gap Voltage on Current Waveform

Calkin (4) has monitored the discharge current waveform for the thyratron-controlled spark source; however, due to insufficient electrical insulation in the chamber, determination of these waveforms under high overvolt conditions was impossible. The current waveform is dependent on the gap voltage; therefore, it can be affected, with the same result, by modification of either the charging voltage or the repetition rate.

A series of current waveforms obtained at different charging voltages is presented in Figure 6-4. The maximum discharge current as a function of charging voltage is shown in Figure 6-5. The current waveform was monitored with an IPC CM-10-M current monitor which generates a 0.1 V/A response. The monitor output was observed on a Tektronics 5403 single beam oscilloscope with 5A4B dual trace module and 5B42 time base modules. The output was digitized and plotted.

These figures show that as the charging voltage is raised, a corresponding increase in the discharge current is observed. In addition, the duration of the discharge is increased slightly. The main discharge also occurs earlier in time and is temporally more stable for the higher energy discharges. The current waveform of the 8000V spark was reproducible within the limits of oscilloscopic resolution; however, the initiation of the main discharge

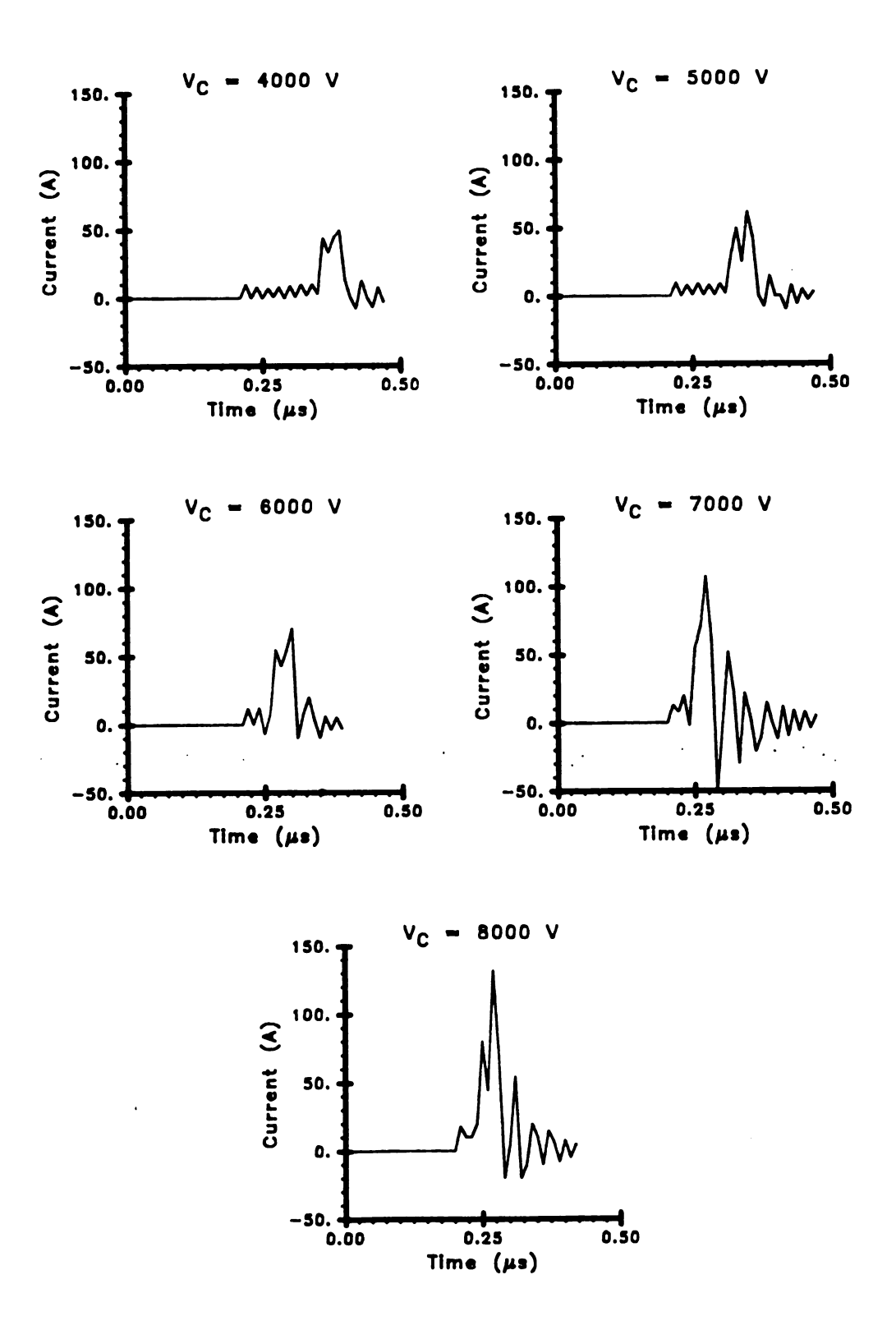


Figure 6-4 Discharge Current as a Function of Charging Voltage

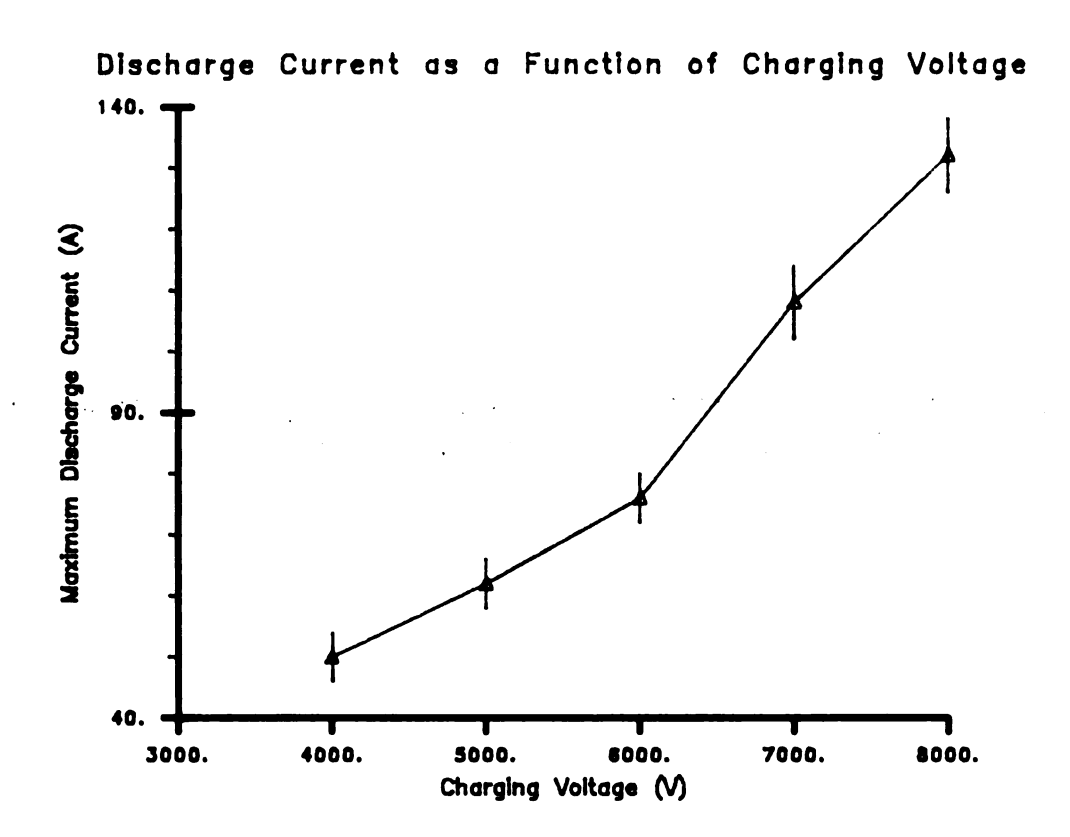


Figure 6-5

Maximun Discharge Current as a Function of Charging Voltage

pulse of the 4000V spark varied by as much a 0.1 µs relative to the initial thyratron conduction. This behavior is understood by the spark formation mechanisms previously presented. The oscillatory behavior of the discharge current is caused by capacitance and inductance characteristics of the high voltage conductor between the spark chamber and the thyratron. Since the thyratron acts as a unidirectional switch, no current is allowed in the reverse bias direction. Walters (104) has performed much work in the area of characterization of oscillatory spark discharges through modification of circuit impedance components. He has found that by manipulation of the discharge circuit impedance characteristics, discharge current waveforms can range from unipolar to oscillatory in nature.

C. Background Emission Studies

To determine regions of possible spectral interference, background emission spectra from 200 to 600 nm were observed at several delay times for an argon discharge. In all studies, except where noted, the parameters listed in Table 6-1 were used. The spectra obtained are shown in Figures 6-6 and 6-7.

The first significant feature observed in the spectra is the emission from neutral carbon atoms at 247.8 nm. This emission was not reported by Zynger (106) or Lantz (2) in the original spark chamber design; however, Koeplin (3) and Seng (107) did report this emission and attributed it to tank impurities. Four possible sources of the carbon background signal are outgassing from the Teflon components, contamination of the support gas from residual oil or contaminants in the argon tank, aspiration of particulate carbon from the gas purifying network, or leakage of atmospheric carbon into the chamber.

Table 6-1

Typical Acquisition Parameters

Charging Voltage	6000 V
Gap Length	3 mm
Flow cell argon flow rate	250 ml/min
Purge gas flow rate	50 ml/min
Repetition rate	2.2 kHz
Slit width	70 μ
Photomultiplier voltage	900 V
Delay time	1.0 µs
Integrate time	4.0 μs
Sparks per point	1024
Gain	various

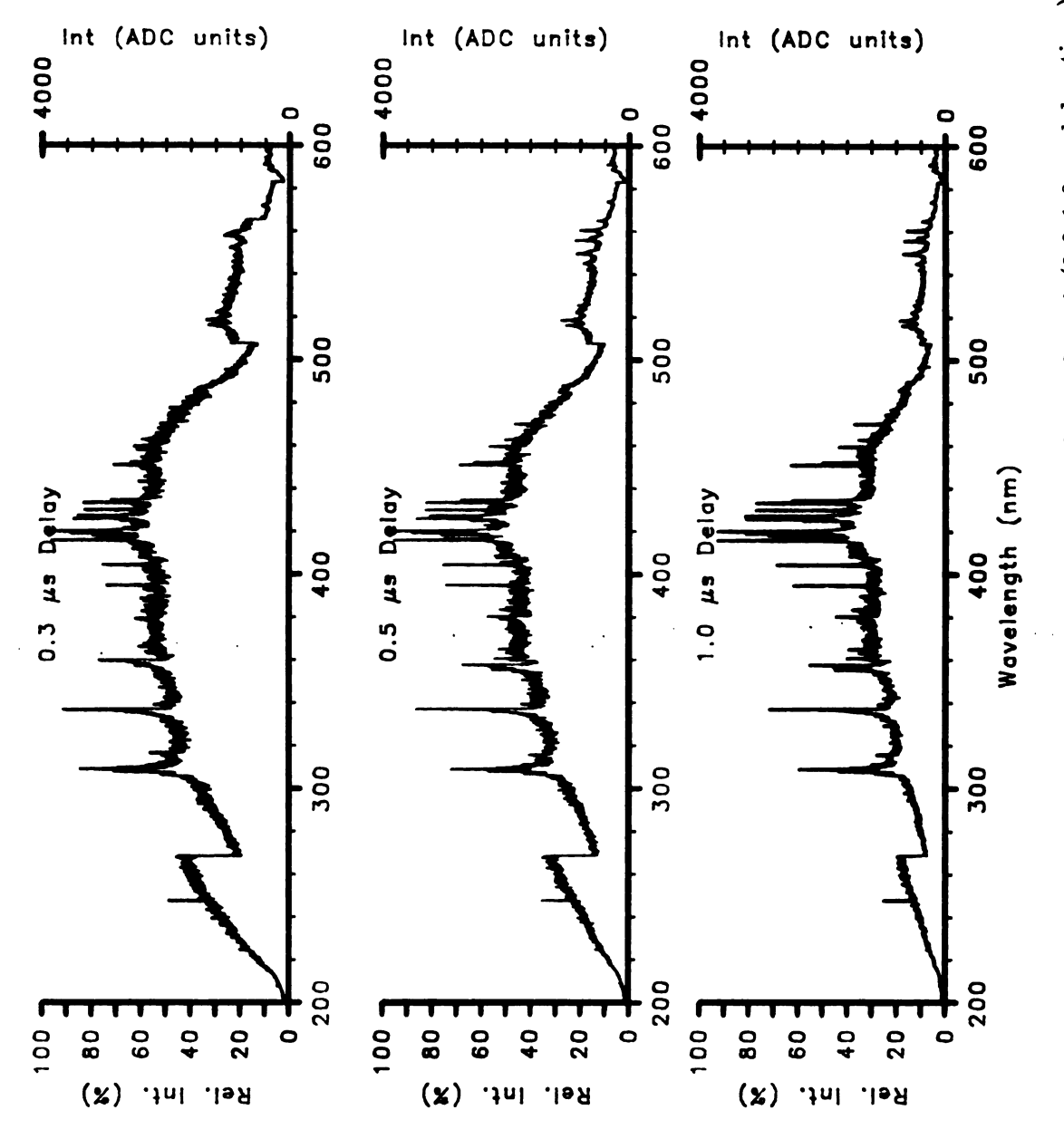


Figure 6-6 Background Emission as a Function of Wavelength (0.3-1.0 µs delay time)

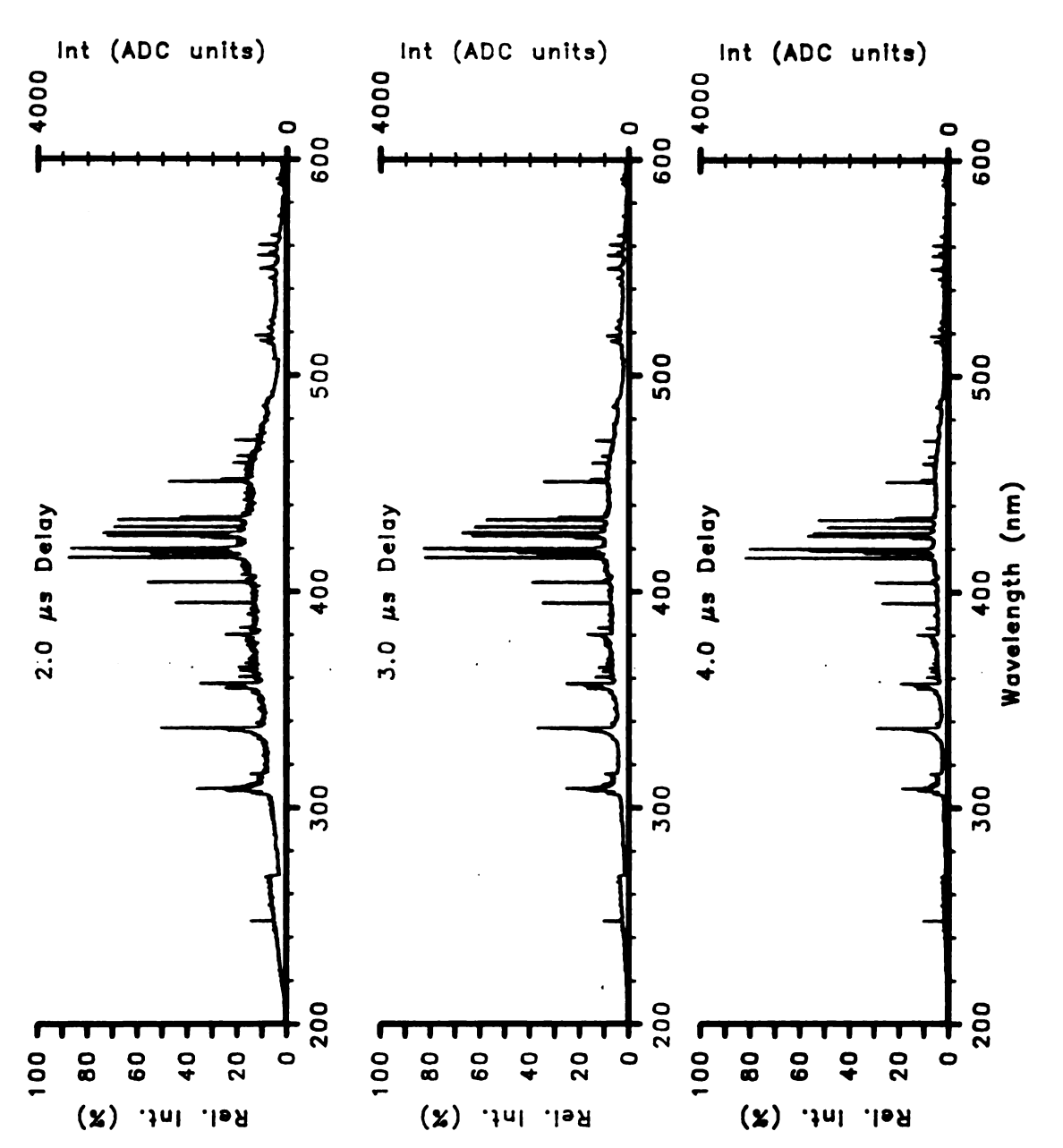


Figure 6-7 Background Emission as a Function of Wavelength (2.0-4.0 µs delay time)

Removal of the purifying network had no effect on the peak intensity; consequently, contamination must occur after the purifying network or the contaminants are unaffected by the network. Since only 99.99% pure argon was used for the support gas; moderate levels of hydrocarbons (maximum 4 ppm (108)) were present. Repeated baking of the Teflon chamber components at approximately 230°C was performed to rid the Teflon of any volatile contamination. During the first hour of baking, a brown substance was formed which was partially volatilized after heat treating for approximately 8 hours. This indicated the presence of unstable volatiles on or in the Teflon, which either originated during the manufacture of these components or was caused by adsorption of organic compounds during normal use. After reassembly, a diminished yet significant carbon background was obtained. Attempts to seal the spark chamber thoroughly from the atmosphere had no effect on the observed background signal; therefore, the carbon background is probably due to outgassing from the Teflon and tank impurities.

Since the spark is most suitable as a gas chromatographic detector, the carbon line is of interest when a universal detection mode is chosen. Therefore, for optimum performance, this interference should be eliminated. A background substraction scheme was used in this work to minimize the carbon interference. Replacement of the Teflon insulation with a glass or ceramic material should completely eliminate one source of this problem.

The second major feature observed in the background spectra is an OH radical emission band centered at 310 nm. This molecular band arises from three sources. The first source is any residual water vapor in the spark chamber from assembly or from solution studies. Since the background spectra presented were obtained approximately one week after some solution work, this is the most likely source.

A second source of water is the possible diffusion of atmospheric water vapor into the spark chamber. Since the spark chamber was well sealed when the background scans were performed, this is probably not the primary source of the background water.

Finally, Ascarite is used as a carbon dioxide scrubbing agent. Due to the hygroscopic nature of NaOH, which is the active agent on the Ascarite, adsorbed water vapor is most likely present. As the dry argon stream is passed over the material, the adsorbed water slowly evaporates into the support gas and is observed by the detector. This process appears to be responsible for the increased hydroxyl emission intensity which was observed when fresh Ascarite was used. Thus, the Ascarite appears to be the major source of water when the detector is operated as a gas phase detector. This problem could be minimized by drying the Ascarite immediately prior to use.

The third and most obvious feature present in the background spectra is the continuum radiation observed between 200 nm and 500 nm. There are two factors which contribute to this continuum: bremsstrahlung radiation and radiative recombination. Zynger has demonstrated, through electron density calculations, that the high energy requirements of bremsstrahlung radiation occur only within the first 0.1 to 0.2 μs relative to spark ignition. The radiative recombination reactions which occur later in time in the spark environment diminish to acceptable levels within approximately 1.0 μs. Prior to this time a high-intensity, noisy spectrum is obtained.

The final feature observed in the spark background is the series of neutral argon lines which occur primarily between 390 nm and 460 nm. These lines have relatively long lifetimes of up to 40.0 µs and are generally quite intense.

D. Effect of Oxygen on Carbon Emission

In an effort to counteract the troublesome background carbon emission and clear the electrode of any carbon buildup, a small amount of oxygen was mixed with the argon support gas. Figure 6-8 shows the effect of added oxygen for several oxygen flow rates at three argon flow rates. In all cases, the emission intensity decreases rapdily to a minimum between oxygen flow rates of 45 and 80 ml/min, after which the intensity increases to levels higher than the original. Oxygen strongly quenches atomic emissions; hence, the initial drop in the signal occurs. Following the decrease, the emission intensity rises again. Since the C emission was due to low level impurities, the emission signal should become constant when a large excess of oxygen is introduced into the instrument. This effect was not observed in this experiment. Three possible molecular species have emission bands in the near vicinity of the 247.86 nm C emission. These are CO, CO⁺, and O₂ at 248.38 nm, 247.42 nm, and 248.0 nm (109) respectively. Since the bandpass of the monochromator was 0.14 nm, the detection of the CO and CO⁺ emissions should be minimized. The O₂ emission; however, falls within the bandpass used. In addition, since oxygen is being added to the spark, the intensity increase observed is due to the increased oxygen levels in the support gas.

E. Excitation Temperature Studies

One useful plasma diagnostic which was performed on the spark was the determination of the excitation or spectroscopic temperature. This calculation requires the derivation of a relationship between the excitation temperature and the observed relative intensities. Line reversal and absorption-emission methods are not used since absorption measurements are much more difficult to perform on the spark. Therefore, a slope method

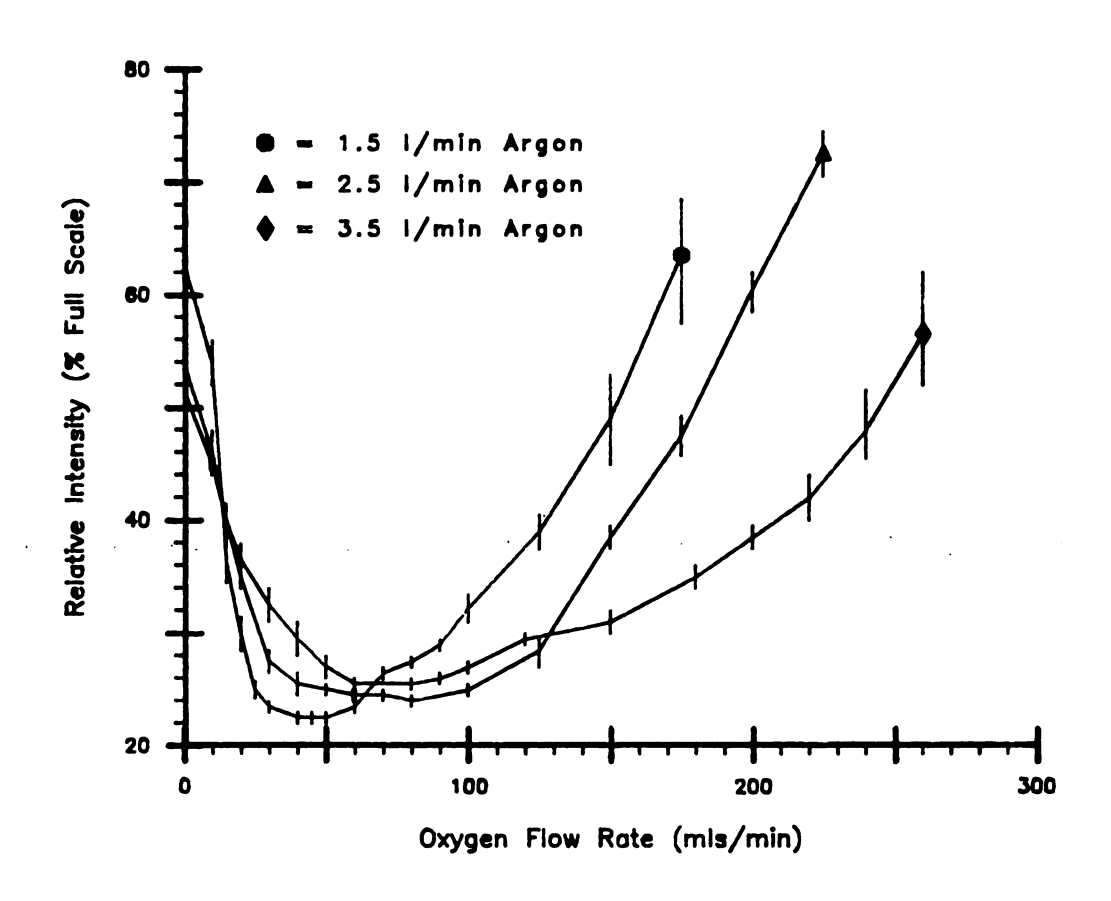


Figure 6-8 Relative Carbon Emission Intensity
as a Function of Oxygen Flow Rate

relating the observed relative intensity and the excitation temperature is used. Zynger (106) among others has derived the equation

$$\log (I \lambda/g_2A_2 \rightarrow 1) = \log C' - E_2/2.303kT_{ex}$$

where I is the observed intensity, λ is the central wavelength for an emission originating in an excited state of energy E_2 with a degeneracy of g_2 and a transition probability of $A_2 \longrightarrow 1$, C' is a proportionality constant, k is Boltzmann's constant, and T is the excitation temperature. This equation states that a plot of the lefthand side of the equation \underline{vs} . E_2 results in a straight line with a slope which is inversely proportional to the temperature. When E_2 is expressed in cm⁻¹ the excitation temperature is given by

$$T = -hc/(2.303k \text{ (slope)})$$

where h is Planck's constant and c is the speed of light.

Reif (110) has shown the validity of the slope method for obtaining the excitation temperature. The requirements of the technique are that no self-absorption occurs and that the spectral response of the optical components are known. A constant spectral response can be assumed over a narrow wavelength range; therefore, selection of a series of spectral lines over a narrow bandwidth circumvents the second requirement. Knopps, et al. (111) and Tourin (112) have found the argon plasma transparent below 650 nm; therefore, the self-absorption criterion is met in the spark.

Two major advantages of the slope technique are that no light source other than the spark is required and there is no theoretical limit on the applicable temperature range.

A series of seven neutral argon atomic emission lines located between 415 nm and 430 nm were chosen for this study. This spectral range is shown in Figure 6-9. The transition characteristics, obtained from tables (113) associated with these lines are presented in Table 6-2.

F. Effect on Time on Excitation Temperature

Spectra from 415 nm to 430 nm were obtained for delay times of 1.0, 1.5, 2.0, 3.0, 4.0, 10.0, and 20.0 µs. A monochromator slit width of 25 µm and a scan rate of 0.05 nm/s were used. After baseline substraction, the peak intensities were measured and plots similar to Figure 6-10 were generated. The excitation temperatures were calculated from the slope of the curve. Estimates of the error in the measurement were derived from the baseline noise observed for the individual runs and the uncertainty in the listed transition probabilities. The results are shown in Figure 6-11. The 0.3 µs measurement appears inordinately high and may be inaccurate due to the random errors associated with the high noise level present in this spectrum. A temperature of 5600 K was found at a delay of 1.5 µs; the temperature steadily decreased over the period studied. The values obtained were approximately 800 degrees higher than those observed by Zynger (106). This is due to the increased energy available in the spark since overvolting of the gap is prevalent in this thyratron-controlled spark.

G. Effect of Charging Voltage on Excitation Temperature

For a second set of data, the charging voltage was varied while a constant delay time of 2.0 µs was maintained. Data were treated in the same manner as outlined in the previous section. The results are presented in Figure 6-12.

Temperatures between 4800 and 5700 K were obtained. The highest

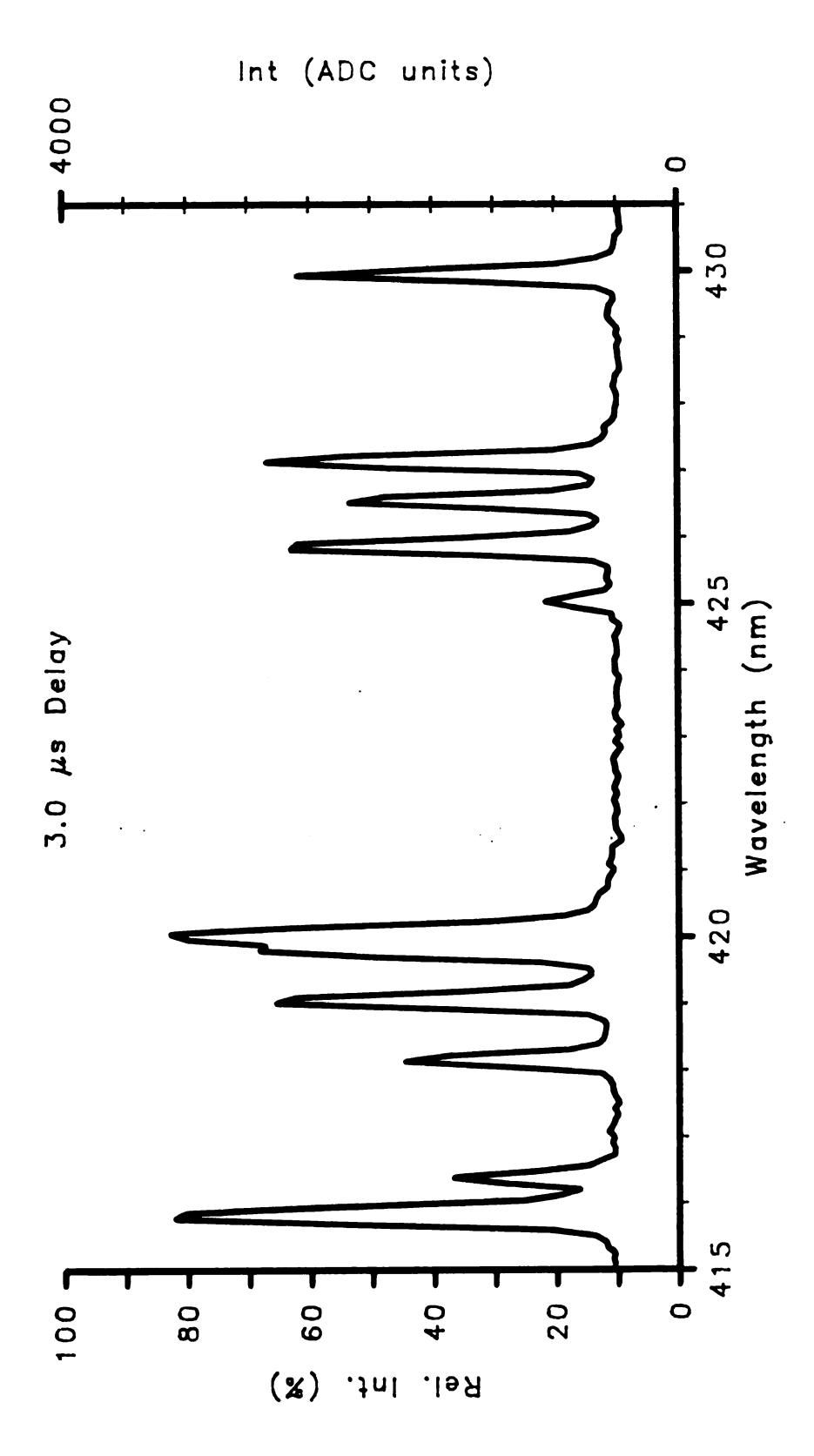


Figure 6-9 Spectrum of Neutral Argon Emission Lines

Table 6-2

Argon Line Emission Parameters (113)

λ(nm)	E ₂ (cm ⁻¹)	g ₂	$A_2 \rightarrow_1 (10^8 \text{ s}^{-1})$
415.9	117184	5	0.0145
416.4	117151	3	0.00295
418.2	118460	3	0.0058
425.9	118871	1	0.0415
426.6	117184	5	0.00333
427.2	117151	3	0.0084
430.0	116999	5	0.00394

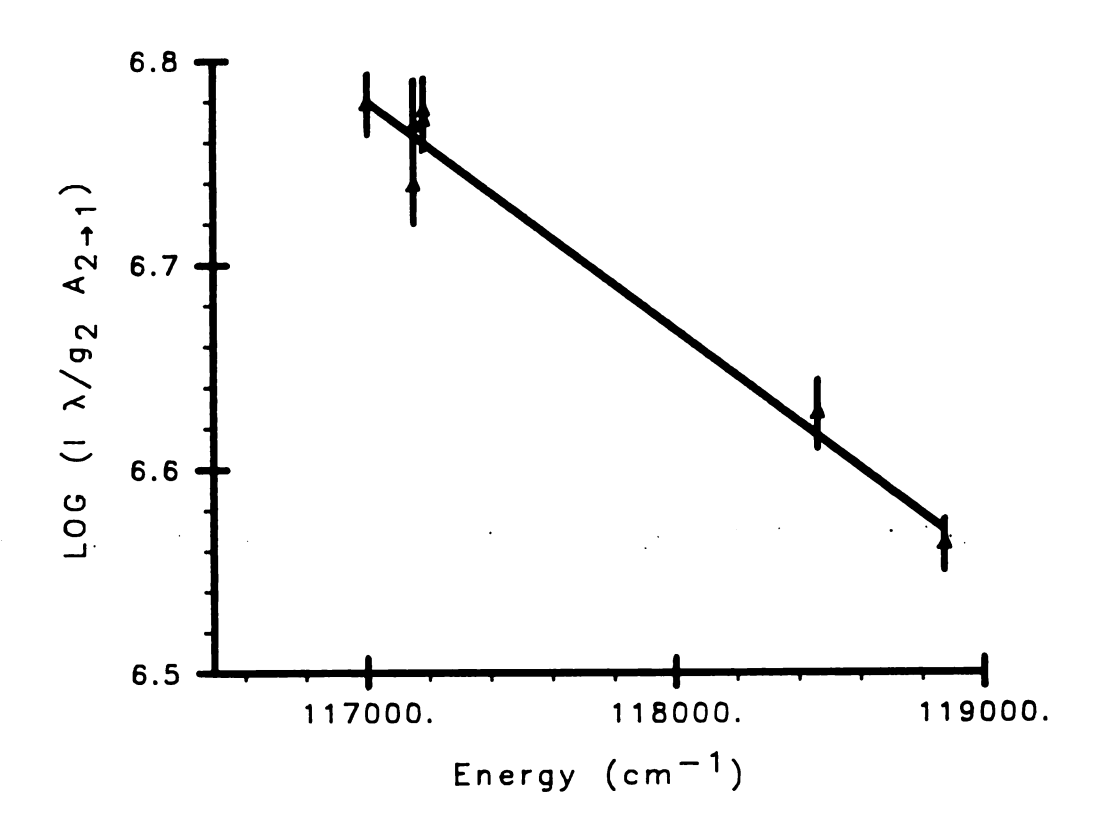


Figure 6-10 Excitation Temperature Slope Plot

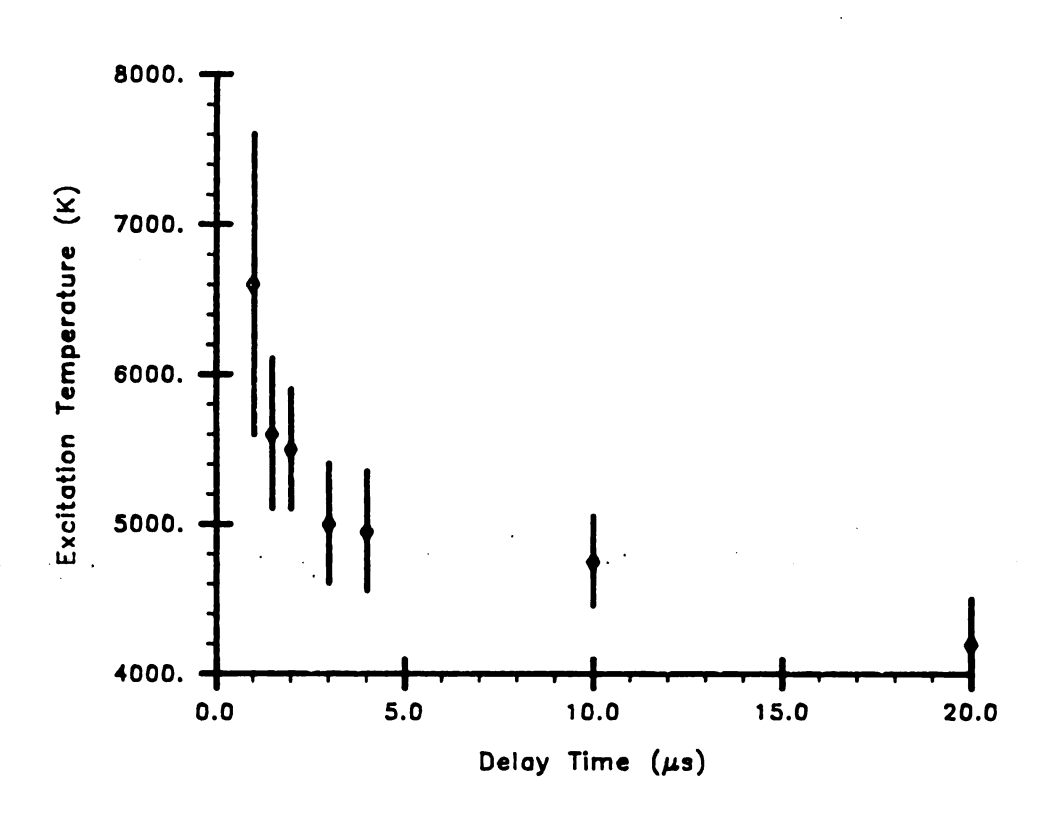


Figure 6-11 Excitation Temperature as a Function of Delay Time

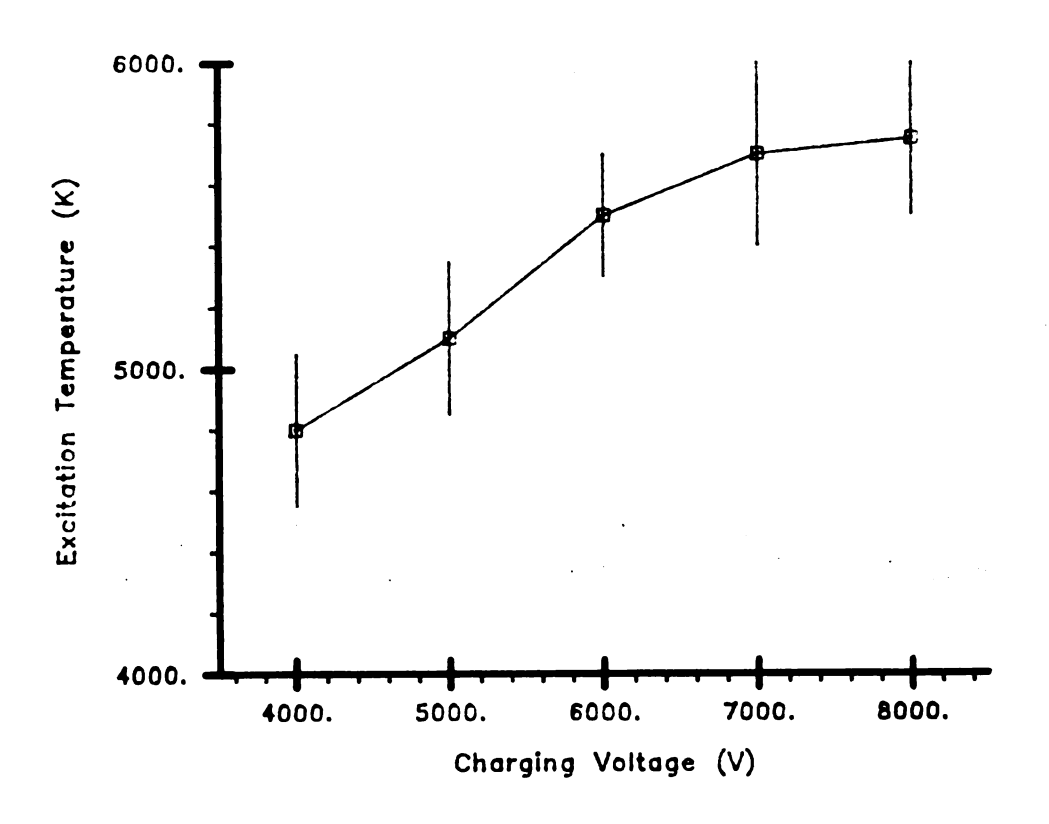


Figure 6-12 Excitation Temperature as a Function of Charging Voltage

excitation temperature was obtained for the highest charging voltage used. Initially, the temperature appears to rise; however, little difference between the 7000 and 8000 V conditions is observed. A higher level of noise in the 7000 and 8000 V spark indicates a more energetic environment; however, this severely compromises the accuracy of the temperature determinations. One explanation for the temperature rise is that the power dissipated in the spark is proportional to the product of the current and the voltage. Since both parameters increase when the charging voltage increases, a temperature rise should be observed.

The excitation temperature obtained from the spark are somewhat higher than the 4850 and 4920 K reported by Taylor, et al. (114) and Fallgatter (115) respectively for an atmospheric pressure microwave induced argon plasma. This indicates that the spark should perform better than the microwave induced plasma as an excitation source for gas phase samples.

H. Electron Density Measurements

Stark broadening is a major line broadening mechanism present in a plasma. This broadening is caused by the electric fields of charged species which surround the excited atom. Hydrogen atomic emission is subject to a linear Stark broadening effect (116). In addition, pronounced broadening on the order of a few nanometers is observed. Since the broadening is caused by charged particles, the electron density in the spark can be calculated from the width of a hydrogen emission line.

Figure 6-13 shows the Stark broadened H_{β} line at 486.1 nm. A delay time of 0.3 μ s, a spark charging voltage of 6000V and a slit width of 50 μ m were used for this spectrum. A total of 8384 sparks were averaged into each data point. The argon support gas was bubbled through distilled water

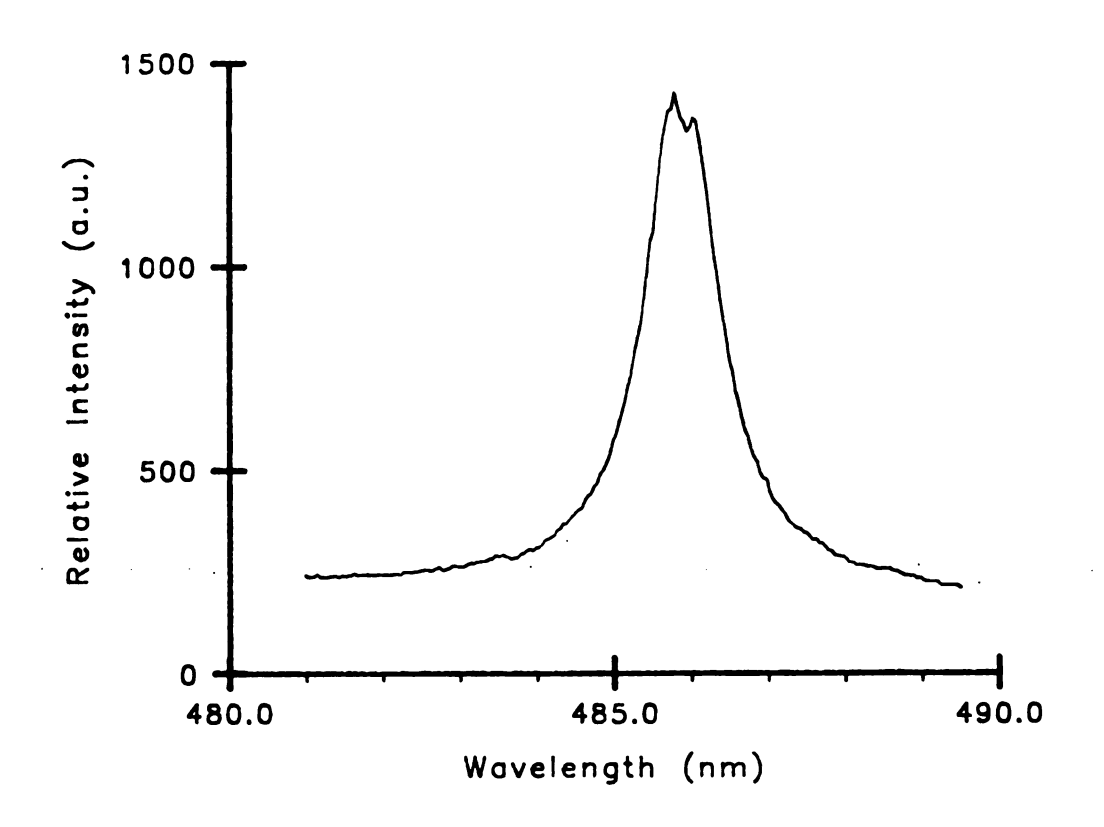


Figure 6-13 $\,\,$ Stark Broadened H_{β} Line Profile

to supply hydrogen to the spark.

Through the Kolb and Griem (117) theory of Stark broadening, the Stark width of a hydrogen line, when raised to the 3/2 power, is proportional to the electron density. The proportionality coefficient is slightly dependent on the electron temperature. Since this parameter is unknown, coefficients tabulated by Griem (116) for several electron temperatures were averaged. The equation

$$N_e = 1.12 \times 10^{16} W^{1.5}$$

expresses the relation between the line width, W, expressed in nm and the electron density, N_e , expressed in electrons/cm³. Figure 6-14 shows the relation between the calculated electron density and the delay time.

I. Determination of Ionization Temperature

To measure the ionization temperature of the spark, the intensity ratio of the 393.3 nm Ca(II) line and the 422.7 nm Ca(I) line was obtained while a 50 ppm solution of Ca was aspirated into the nebulization/desolvation system. Thirty data points were collected at each delay time at both wavelengths and averaged. The standard deviation of the averaged intensity was used as a measure of the error. Figure 6-15 shows the decay of the Ca atomic and ionic emission lines as a function of time.

The Saha equation describes the relation between the degree of ionization, the ionization temperature (T), and the electron pressure (P_e). Using Boumans' (119) notation, the intensity ratio of an ion-atom pair is

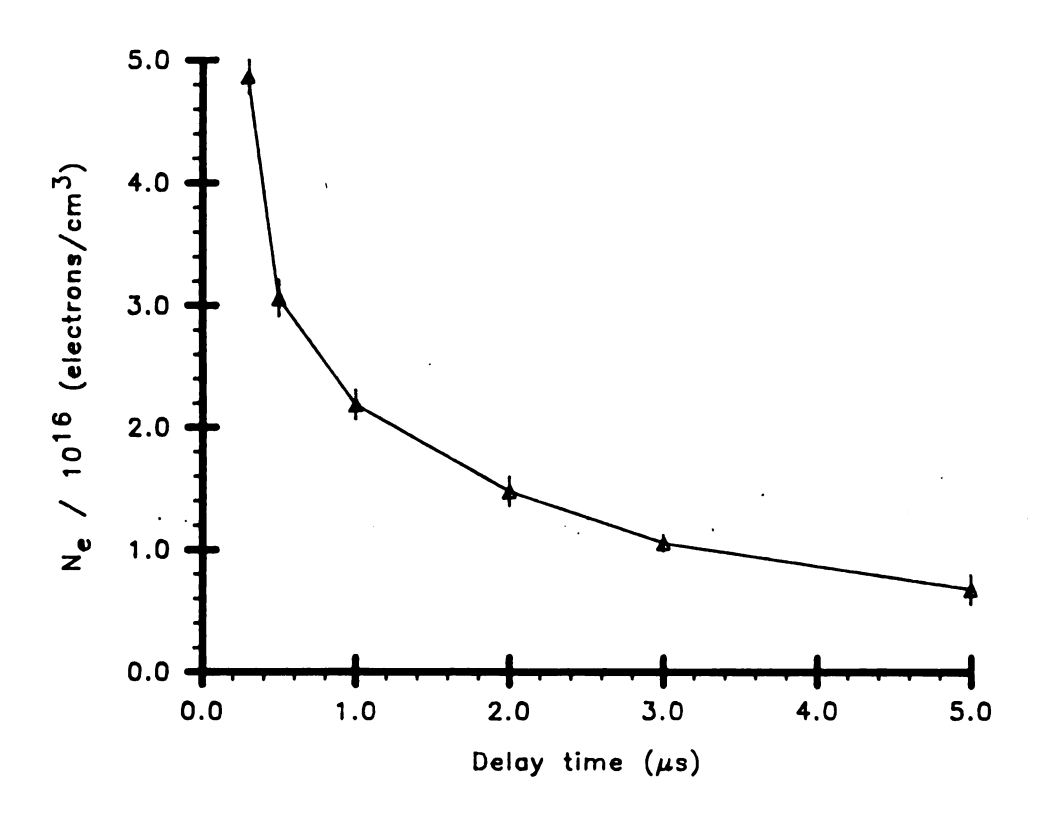


Figure 6-14 Electron Density as a Function of Delay Time

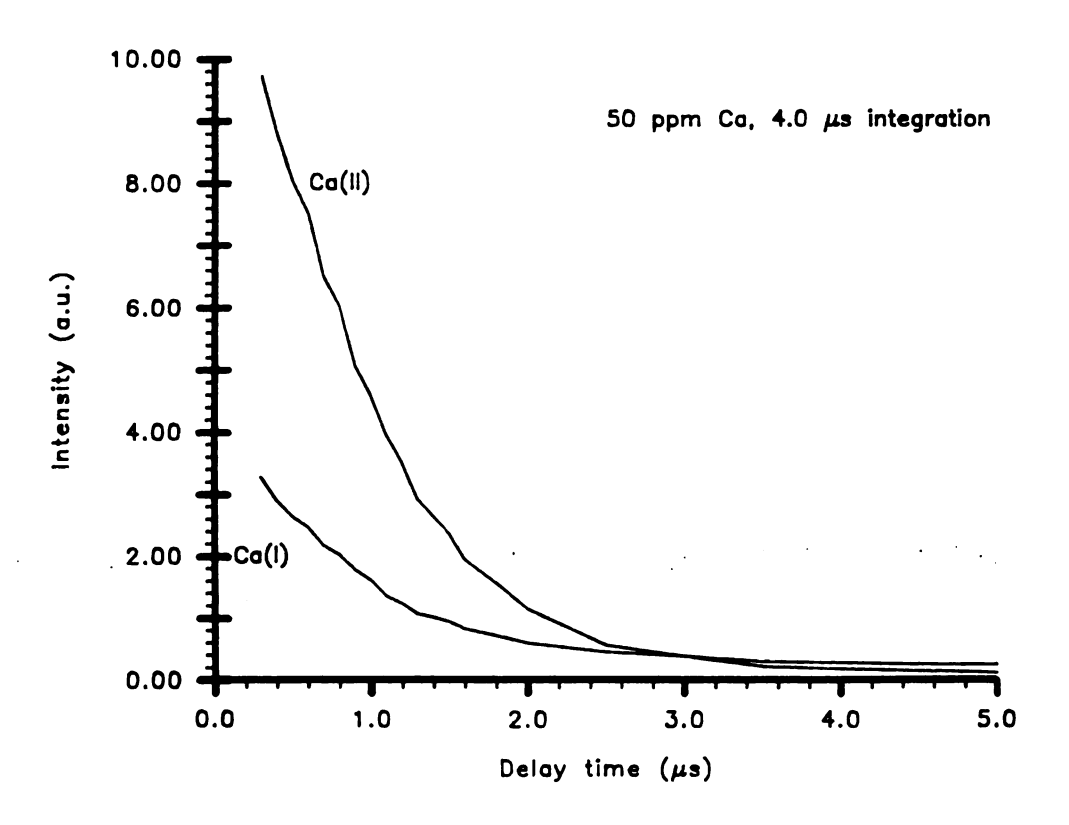


Figure 6-15 Calcium Emission as a Function of Delay Time

$$\log (I^+/I) = -\log P_e + \log g^+A^+_{2\rightarrow 1} \lambda /gA_{2\rightarrow 1}^+$$

$$-5040(V_{ij} + V_{q}^{+} - V_{q})/T + 5/2 \log T - 6.18$$

where the superscript '+' refers to the ions, $V_{\bf q}$ is the excitation level from which the excitation occurs, and $V_{\bf ij}$ is the apparent ionization potential for the atom. According to Boumans, the apparent ionization potential for Ca is 5.83 eV. Values of 1.0 and 0.91 were reported by Corliss and Bozman (120) for the gA values for the atomic and ionic emission lines. Excited state energy levels of 2.93 eV and 3.15 eV for the atom and ion were obtained from spectral tables (121). The electron pressure is

$$P_e = N_e T / 7.34 \times 10^{21}$$

With the electron densities calculated in the previous section, equations 6-5 and 6-6 were solved recursively on the minicomputer for T at each delay time. The results of these calculations are presented in Figure 6-16.

In comparison to Zynger's characterization of the single gap system (106), the time averaged ionization temperature for the present design is approximately 600 degrees lower. This is probably due to more complete desolvation with the desolvation chamber Zynger used. The increase in the quantity of water vapor would require more energy from the spark for desolvation and excitation. This, in turn, lowers the temperature of the spark.

Since the excitation temperature was determined in a pure argon stream and the ionization temperature measurement was performed in an argon

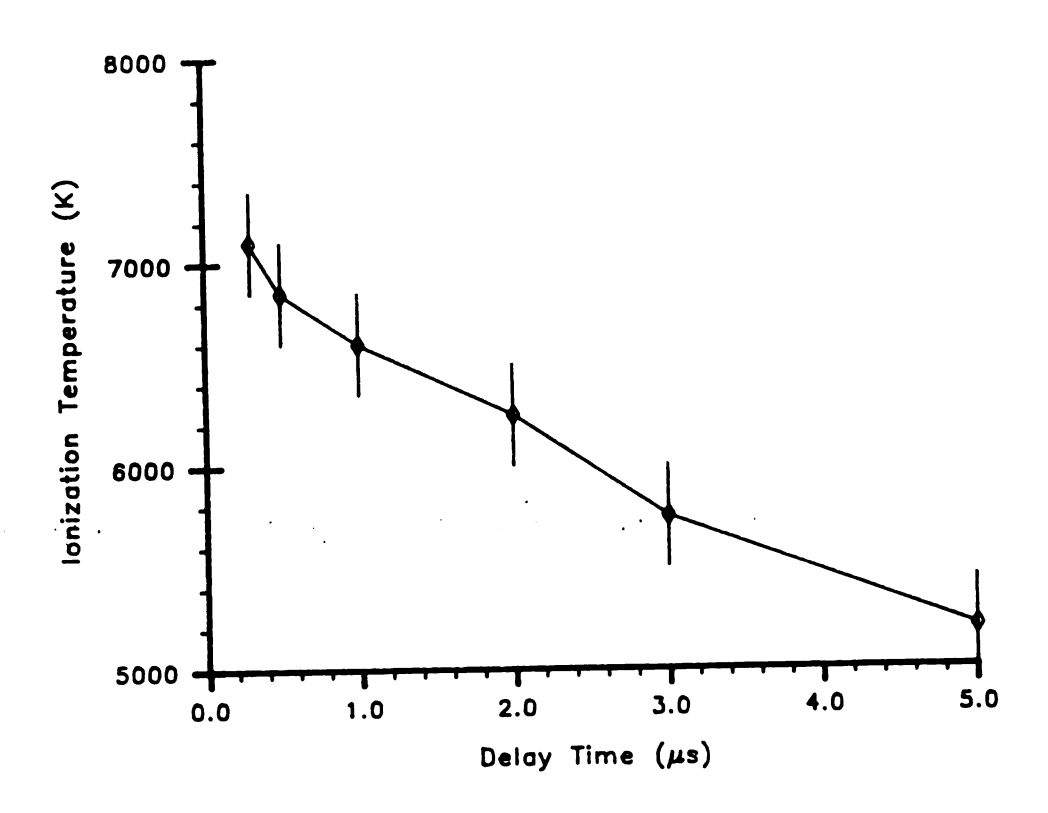


Figure 6-16 Ionization Temperature as a Function of Delay Time

stream which contained some water vapor, a comparison of the two temperatures is difficult; however, some conclusions can still be made from this information. Even under the energetically less favorable conditions, the ionization temperature was found to be approximately 1000 K higher than the excitation temperature. This indicates that thermodynamic equilibrium is not achieved in the spark. Similar characteristics were found in the original single gap system of Zynger.

CHAPTER VII

CHROMATOGRAPHIC EVALUATION

A. Introduction

Lantz, Koeplin, and Calkin (2-4) have demonstrated the element-selective detection capabilities of the spark source for use with packed column gas chromatography. Their work has been concerned with the detection of metallic and non-metallic elements in GC effluent and has demonstrated the visability of spark detection for several elements. Detection limits in the ng/s range were determined for many elements. In recent years, capillary gas chromatography has been applied to a wide range of sample Because the capillary media demonstrates extremely high analyses. theoretical plate counts, the resolution of chromatographic peaks is much higher than with traditional packed column technology. In conjunction with the increased separation power of capillary GC, an increase in the quantity of discernable peaks and, hence, an increase in the complexity of peak identification was inescapable. One approach to simplifying the chromatogram is by use of a detection method which detects only the component(s) of interest. Ideally, the chromatographer could specify the peak of interest and the detector would respond quantitatively to that component and have no response to any other constituent. One method which approaches this ideal is element-selective detection. In this method, the detector responds preferentially to those components which contain the element of interest and remains nonresponsive to other species. By using atomic emission spectroscopy, the element of interest is detected by adjustment of the observation wavelength. Considering the broad range of applicability of emission spectroscopy, the extension of the spark source to the detection of capillary gas chromatographic effluents would simplify the interpretation of complex chromatograms.

This chapter consists of an evaluation of this capillary GC-spark interface, a discussion of the universal detection capabilities of the spark, and an application of element-selection to the analysis of leaded gasoline.

B. Evaluation of the GC-Spark Interface

One of the major advantages of capillary GC is that band broadening is kept to a minimum, since column volumes are extremely small. Hence, one requirement of the detector is that the high resolution not be compromised by the detector characteristics. To this end, the effective volume of the detector must be kept to a minimum. In the detector interface designed for the spark (Figure 3-5), the capillary column is threaded through a 15 in. x 1/4 in. o.d. glass tubing which is wrapped with heating tape. The heating tape was used to maintain temperatures above that required for the particular separation study. One end of the interface protrudes approximately 1/2 in. into the GC oven. The other end of the interface slides through a Teflon positioning collar and protrudes approximately 3/4 in. into the flow cell in the spark chamber. At this end, the interface consists of two concentric tubes. The column passes through the inner, 1/8 in. o.d. tube, and argon plasma support gas is supplied through the outer tube. A low argon flow

rate of 0.25 1/min assures a non-turbulent gas flow out of the end of the interface. This acts to restrict the diffusion of the effluent stream throughout the flow cell. Manual positioning of the end of the column to within 2 mm of the spark gap minimizes the effective detector volume to approximately 1.6 nl for an 0.32 mm i.d. capillary column. Arcing to the end of the column at shorter separations prevented further reduction in the detector volume. An alternate aluminum interface was constructed to take advantage of its increased thermal conductivity and less fragile nature; however, occasional arcing to the interface was observed. This created a potential electrical hazard to the operator and the equipment; hence, the glass interface was preferred.

To determine the effect of the interface on column performance, the resolution of the spark system was compared to that of the flame ionization detector (FID) supplied with the GC. The resolution, $R_{\rm S}$, of two adjacent chromatographic peaks is given by the equation:

$$R_S = (t_{R2} - t_{R1})/0.5(t_{W1} + t_{W2})$$

where the subscripts 1 and 2 refer to the earlier and the later eluted components respectively, t_R is the retention time of the peak, and t_W is the width at the base of the peak (122). For the determination of the resolution, a chromatogram of a jet fuel sample was obtained with both the FID and spark detectors, using the conditions shown in Table 7-1. Figure 7-1 shows the chromatogram obtained with the FID and the spark detector. The two peaks labeled in the figure were used to determine the resolution for each case. Values of 1.4 and 2.2 were obtained for the resolution for the FID and spark chromatograms respectively. This indicates that band

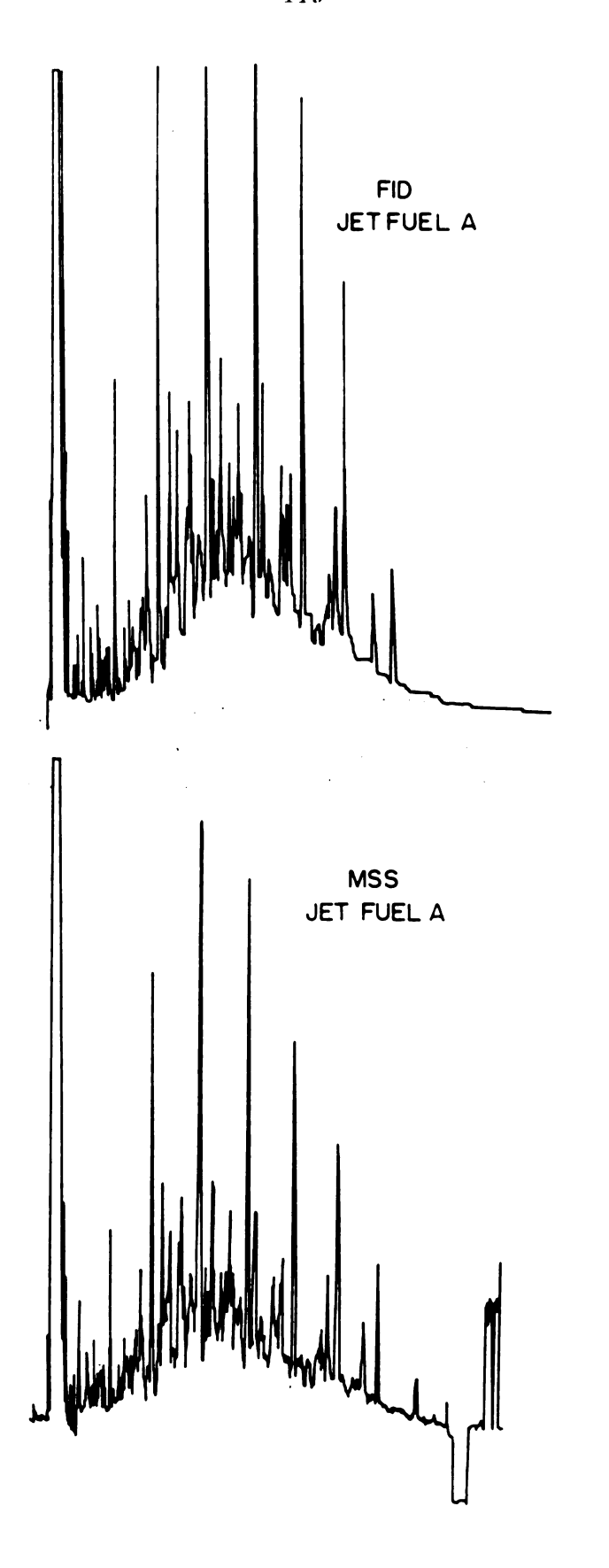


Figure 7-1 Comparison of FID and NSS Detection

Table 7-1.

Jet Fuel Gas Chromatographic Conditions

Column	30 m x 0.32 mm
	0.25 μ DB-1
Sample	1.0 % Jet Fuel
Sample Size	1.0 μ1
Helium Flow Rate	50 cm/sec
Initial Temperature	30°C
Initial Hold Time	0 min
Program Rate	4 deg/min
Final Temperature	150°C
Final Hold Time	10 min
FID Parameters	
O ₂ Flow	300 ml/min
H_2^2 Flow	30 m1/min
Helium Makeup Flow	30 ml/min
Attenuation	16
Range	10 ⁻¹¹ A
Spark Parameters	
Ar Makeup flow	1.0 1/min
Ar Sheath Flow	250 1/min
Interface Temperature	240°C
. Gap Voltage	6000 V
Gap Length	3 mm
Observed Wavelength	247.8 nm
Slit Width	125 μm
PMT Voltage	1000 V
Delay Time	0.9 μs
Integrate Time	4.0 μs
# Sparks per Point	1024
Gain	250

broadening was lower with the spark than with the FID. This is possible since the FID associated with the GC was not originally designed for use with a capillary column. As such, a commercially available detector insert (SCE DC-8) was required for capillary compatibility.

Since the sample inlet for the FID was oriented at right angles and approximately 2 cm below the base of the FID, a relatively large detector dead volume of approximately 18.0 nl was unavoidable. Considering this aspect of FID, the higher resolution of the spark is understandable.

The second important criterion for the interface is the capability to attain acceptably high temperatures to prevent condensation of those components which elute at high temperatures. If condensation were a problem, the detector response would decrease and peak widths would increase for high temperature components. In practice, interface temperatures of 250 ± 10 °C were maintained throughout the chromatographic run. Again a comparison between the two chromatograms shown in Figure 7-1 indicates no loss of chromatographic quality with the spark detector.

C. Universal GC Detection Capabilities

Most GC detectors in general use are classified as universal detectors, since they respond to all compounds with few exceptions. The FID and, in one mode of operation, the electron capture detector belongs in this category. The spark detector can be operated in this mode as well by monitoring the neutral carbon emission at 247.8 nm. Lantz (2) has found detection capabilities for several compounds are independent of the functional groups present in the compound. This includes carbonylic and nitrilic carbon which demonstrate poor detectability in the FID. Detection limits of 2 x 10^{-8} gs⁻¹ with linearity over two orders of magnitude were reported by

Koeplin and Calkin (3,4) for packed column chromatography.

To determine the detection limit for carbon for the capillary system, a series of n-alkanes in hexane was chromatographed with the conditions shown in Table 7-2. A representative chromatogram is shown in Figure 7-2. The undecane peak was digitally integrated. The resultant integrated peak intensities were used to generate the calibration curve shown in Figure 7-3. As in the packed column studies cited, a linearity of two orders of magnitude was observed; however, a detection limit of $4.0 \pm 0.5 \times 10^{-8} \text{ gs}^{-1}$ was obtained.

The presence of the background carbon signal made carbon determination less accurate and sensitive than would otherwise be expected. The high background and the accompanying baseline noise made observation of small analyte signals difficult even though electronic baseline subtraction was enabled.

An alternate explanation for the slight decrease in sensitivity concerns the time scale of capillary GC. Typically, peak widths in packed column chromatography are approximately 20 to 30 s for major components. However, with capillary technology, peak widths of under 5 s are common. Since the spark is a discontinuous plasma, sharp peaks can be undersampled or aliased. Figure 7-4 shows typical peaks obtained with capillary and packed column gas chromatography. The vertical dashed lines indicate possible times when the peak is sampled. For the packed column, this sampling has no effect on the observed peak height since the top of the peak is broad with respect to the sampling rate. However, if the top of the capillary peak is narrow in comparison with the sampling period, loss of accurate peak reproduction occurs. Expressed in terms of the Nyquist constraint for sampling, the Nyquist frequency of the packed-column peak is much lower than that of the capillary

Table 7-2.

Carbon Standards Gas Chromatographic Conditions

Column	30 m x 0.32 mm 0.25 μ DB-1
Sample	Neat C _n H _{2n+2} Mix
Sample Size	1.0 µl
Helium Flow Rate	50 cm/sec
Initial Temperature	25°C
Initial Hold Time	5 mi n
Program Rate	4 deg/min
Final Temperature	200°C
Final Hold Time	0 min
Spark Parameters	
Ar Makeup Flow	1.0 1/min
Ar Sheath Flow	250 1/min
Interface Temperature	250°C
Gap Voltage	6000 V
Gap Length	3 mm
Observed Wavelength	247.8 nm
Slit Width	70 μm
PMT Voltage	900 V
Delay Time	0.4 μs
Integrate Time	10.0 μs
# Sparks Per Point	1024
Gain	250

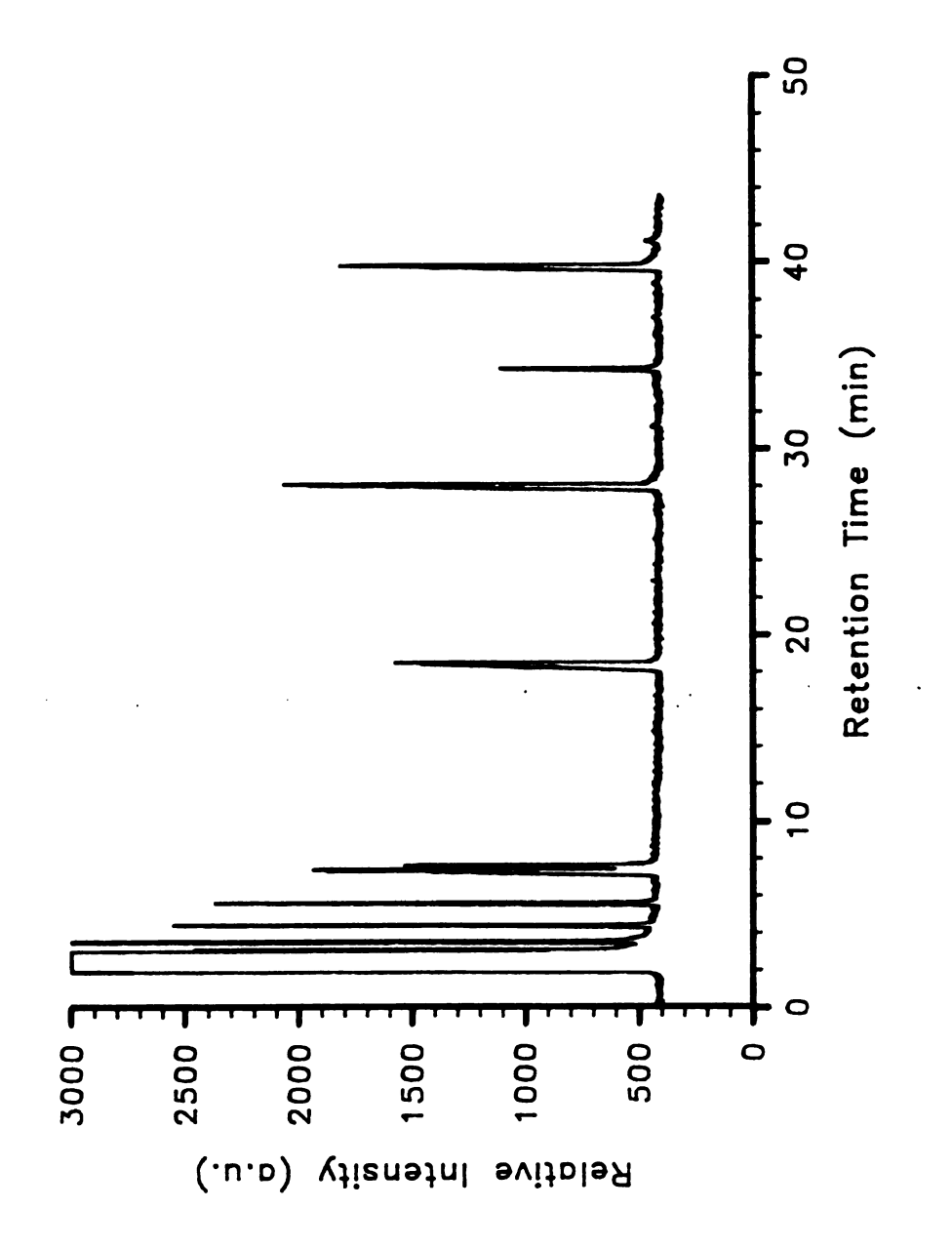


Figure 7-2 n-alkane Chromatogram

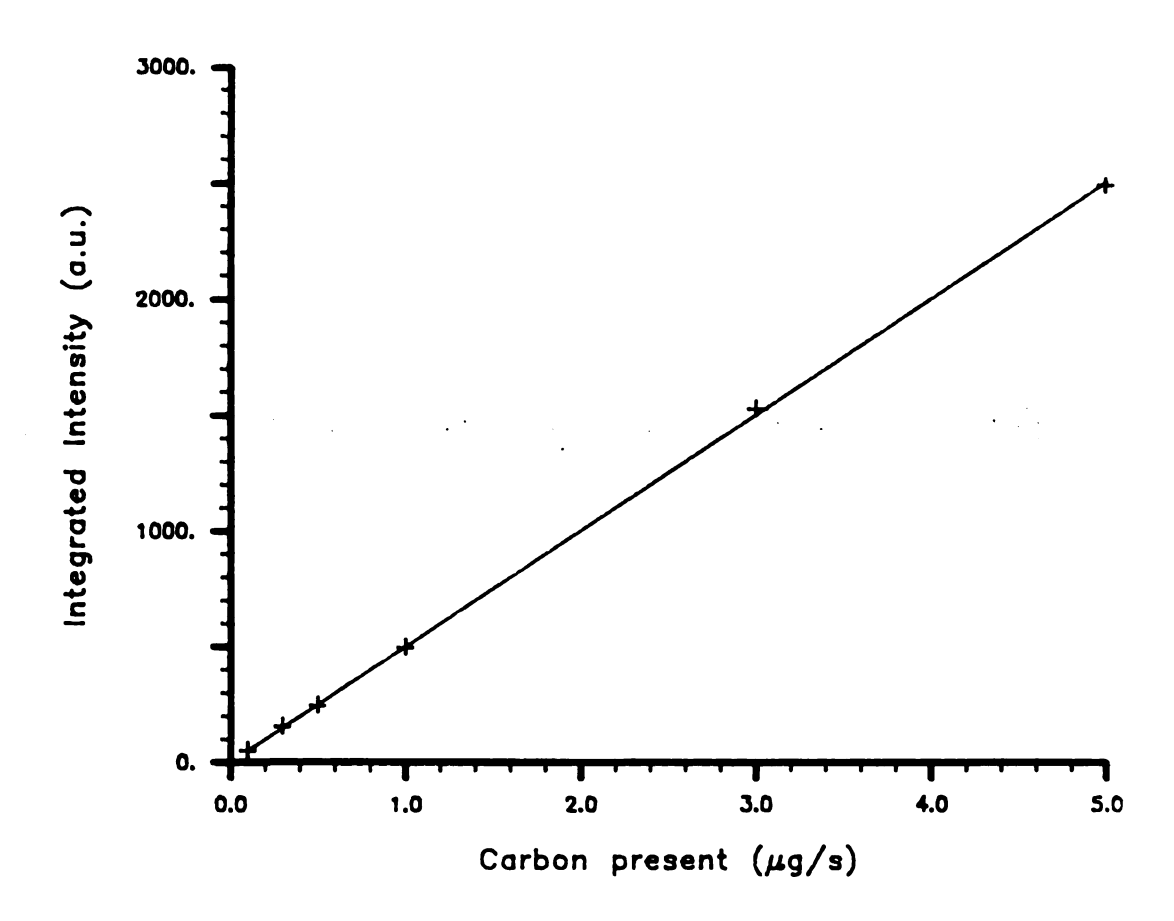


Figure 7-3 Carbon Calibration Curve

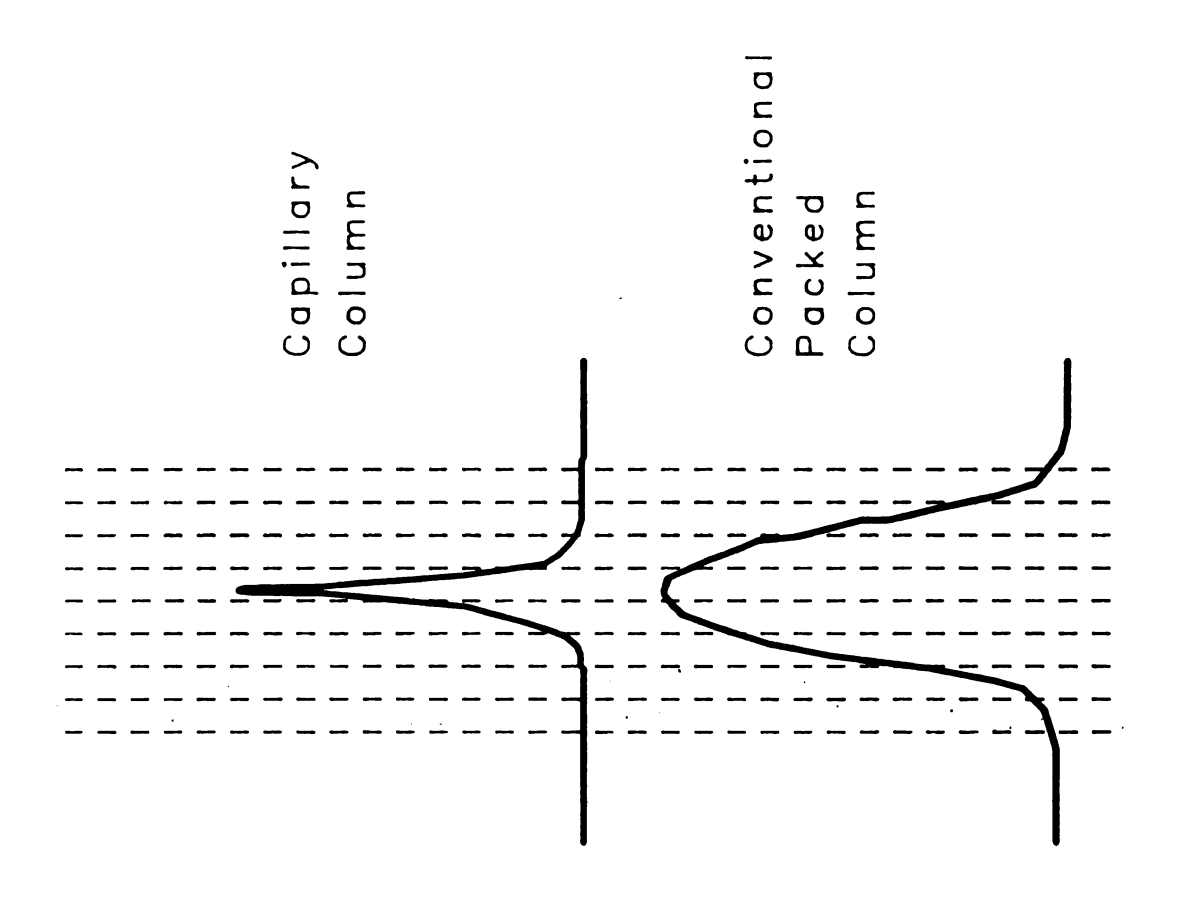


Figure 7-4 Chromatographic Peak Digitization Errors

peak, hence, a higher minimum sampling rate is required for capillary chromatography. Since the sampling rate for the spark was 2.2 kHz, Figure 7-4 exagerates the severity of the problem for data acquisition. However, the data display update frequency is only 2 Hz; hence, some biasing of the chart recorder output does exist. Because of this, the digitized peak areas are accurate representations since they are a time averaged signal over the entire peak even though peak height information exhibits some biasing. A similar evaluation by Holland et al. (61) concerning capillary GC-MS data acquisition concludes that a sampling rate of two and preferably five data points per second is sufficient for regeneration of a chromatographic peak.

D. Element-Selective Detection of Lead in Gasoline

The major benefit of using an atomic emission technique for chromatographic detection is the associated element-selectivity. Previous work has demonstrated the detectability of several elements which include Ca, Si, B, Al, P, Cu, Cr, Br, I, N, and O. The current work applies the capacity for element-selective detection to the analysis of Pb in gasoline.

The currently approved standard method for the determination of lead in fuels consists of a sample preparation step followed by lead detection by atomic absorption. The preparation step consists complexation of the lead with iodine. stabilization of the iodide with alkvl lead tricaprylmethylammonium chloride, and a 10-fold dilution with methyl isobutyl ketone (123). The preparation step is time-consuming since the reaction between the iodine and lead is slow. In addition, it has been reported that the preparation step is not highly reproducible (124). In an attempt to avoid the slow preparation step, gas chromatographic analysis of a neat gasoline sample was performed.

1. Lead Calibration Curve

Gasoline additives, the most common being tetraethyl lead, are used to increase the octane rating of the fuel. An increase in the octane rating decreases the tendency of the fuel to knock or ignite before a spark is fired. One common property among the antiknock agents is that they possess a high boiling point in comparison to the remainder of the fuel components. This information allows chromatographic conditions which simplify and accelerate the determination to be selected. Specifically, a high initial temperature is selected to rapidly elute most fuel components. The chromatographic conditions used for all lead standards and gasoline samples are shown in Table 7-3.

A series of standard lead samples were prepared by dilution of the 0.537 µg/µl (1.994 g/gal) lead reference mixture (NBS standard reference material 1636) with n-hexane. These standards are a mixture of 91% by volume 2,2,4-trimethylpentane and 9% by volume n-heptane (125). Tetraethyl lead supplies the analyte concentration.

A lead standard chromatogram acquired in both the universal carbon mode detection and the element-selective mode for lead is shown in Figure 7-5A and B respectively. The carbon mode shows two distinct features. First, a large signal centered at 2.2 min corresponds to the coelution of the 2,2,4-trimethylpentane and heptane. Second, a smaller peak occurring at 6.1 min is observed; this is the tetraethyl lead. The chromatogram obtained while monitoring the Pb(I) emission at 405.7 nm also shows features corresponding to the solvent front and the lead compound; however, the solvent front in this mode causes a negative deviation in the baseline. This response is caused by cooling of the spark by the entire plug of solvent and has been observed in all previous versions of the nanosecond spark source

Table 7-3.

Lead Standards Gas Chromatographic Conditions

Column	30 m x 0.32 mm
	0.25 μ DB-1
Sample	Neat Pb standards
Sample Size	1.0 µl
Helium Flow Rate	50 cm/sec
Initial Temperature	90°C
Initial Hold Time	5 min
Program Rate	4 deg/min
Final Temperature	140°C
Final Hold Time	0 min
Spark Parameters	
Ar Makeup Flow	1.0 1/min
Ar Sheath Flow	250 m1/min
Interface Temperature	250°C
Gap Voltage	6000 V
Gap Length	3 mm
Observed Wavelength	247.8 nm
Slit Width	70 μm
PMT Voltage	900 V
Delay Time	0.4 μs
Integrate Time	10.0 μs
# Sparks Per Point	1024
Gain	250

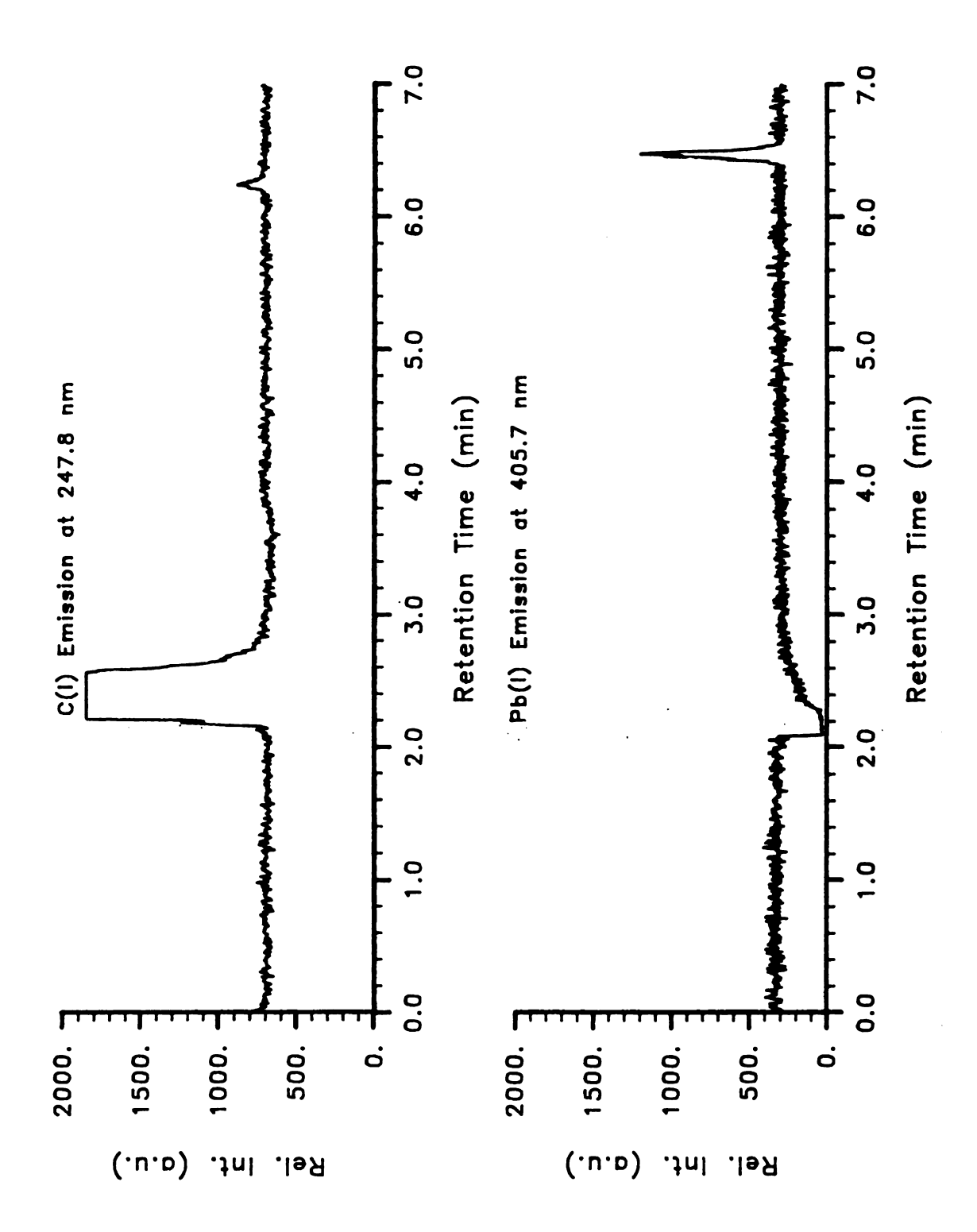


Figure 7-5 Lead Standard Chromatogram

(2-4). The tetraethyl lead peak in the lead mode is shifted approximately 0.1 m relative to the peak observed in the carbon mode. The shift is caused by a lack of reproducibility in the carrier gas flow rate and variation in the temperature program initiation timing.

A series of standard lead mixtures were separated and the lead peak was digitally integrated. The calibration curve shown in Figure 7-6 demonstrates the results obtained. The highest reference concentration available was $0.537~\mu g/\mu l$ lead; hence, the upper limit of the calibration curve was not determined. Under the chromatographic conditions studied, a detection limit of $7.5~\pm~0.8~\rm ng s^{-1}$ was found. At this mass flow value, a signal equal to two times the background noise was obtainable. For the above determination, the detection limit corresponds to a mass of $0.15~\pm~0.06~\mu g$ or a concentration of $0.55~\pm~0.06~g/g a l$.

Figure 7-6 also shows that the calibration curve does not pass through the origin but has a negative y-intercept. An explanation for this characteristic is that the spark is cooled by the presence of the analyte. This lowers the background level as the peak elutes and causes the acquisition of a dimished intensity value.

2. Lead Determination in Gasoline

Carbon mode chromatograms of leaded gasoline are similar to the lead standard chromatogram. However, because gasoline is a complex mixture of several compounds, the early portion of the chromatogram demonstrates a response to a series of components. These components are not well resolved for two reasons. First, the chromatographic conditions were optimized for the determination of high-boiling components; hence, the majority of the gasoline components are rapidly eluted. Second, a large injection volume is required to adequately determine the lead-containing species. This resulted

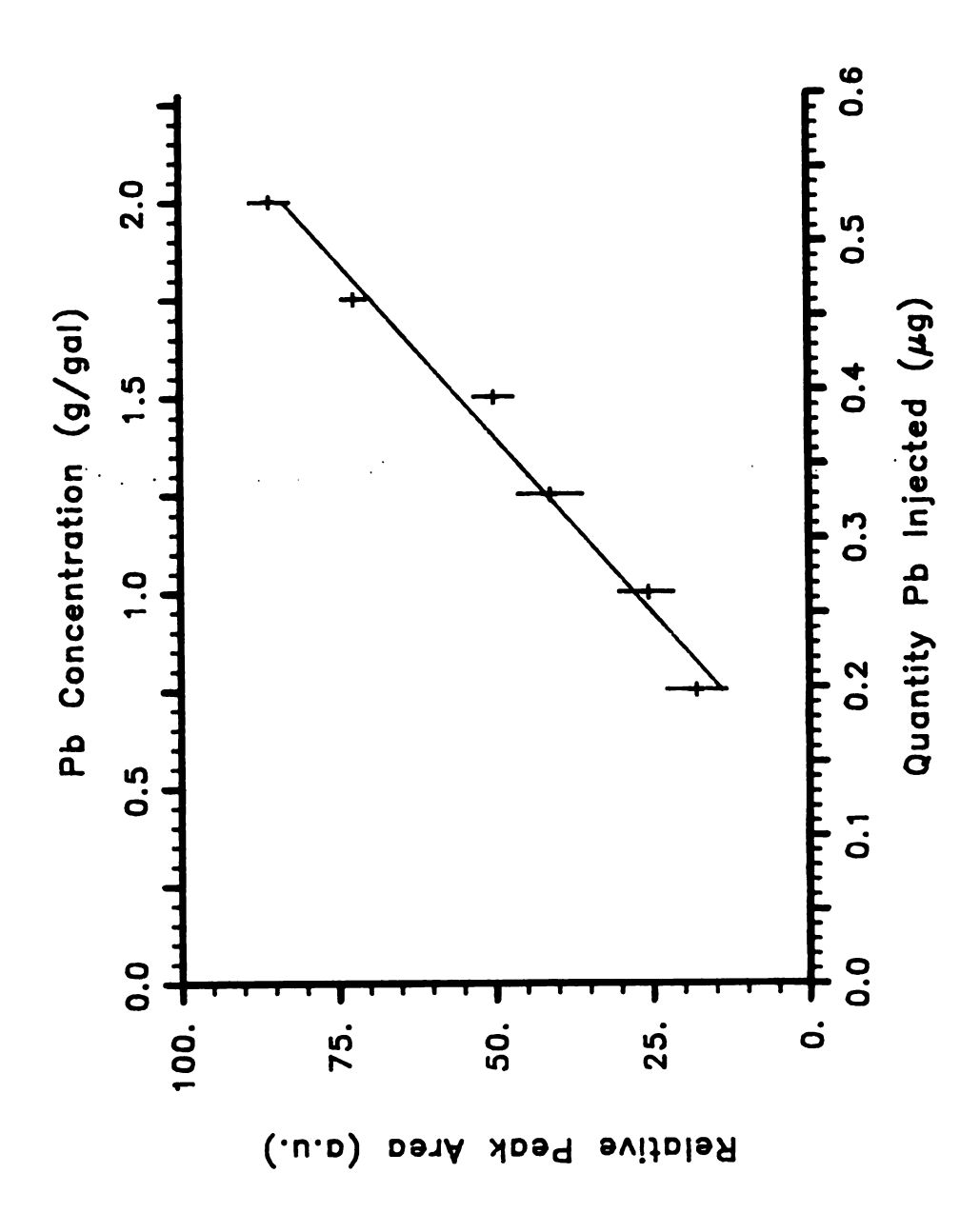


Figure 7-6 Lead Calibration Curve

in a column overload for the low-boiling, major components. In addition to the response for low-boiling components, a single, small peak is observed at the retention time for tetraethyl lead. The chromatogram for leaded gasoline observed while monitoring the lead emission line is similar to that obtained for the lead standards except that the initial negative response to the solvent front is slightly longer-lived for the gasoline studies. This is because a longer time is required to elute all of the low-boiling components of the gasoline. As was true of the lead standards, a single positive response is obtained at the retention time for the tetraethyl lead standard. Digital integration of the peak and correlation with the previously presented calibration curve indicated a lead concentration of 290 \pm 35 $\mu g/g$, or 0.76 \pm 0.09 g/gal. Other researchers (126,127) have reported values ranging from 0.01 g/gal to 1.9 g/gal for gasoline from various sources. In comparison to these values, those determined by spark detection are reasonable.

Although the detectability of lead has been demonstrated in this work, the detection limit obtained with these conditions is not comparable to the $0.002~\mu g/gal$ obtained with the standard method. However, much higher capacity capillary columns have been developed since these experiments were performed. Preliminary experiments with such a column indicate that injection volumes of up to $4.0~\mu l$ do not seriously degrade the chromatographic performance. This would improve the detection limits by a factor of four or more since higher injection volumes could be used.

CHAPTER VIII

CONCLUSIONS AND PERSPECTIVES

The current work has shown that the thyratron triggered spark is temporally stable and reproducible. The arcing problems noted earlier have been eliminated with the present, insulated chamber design. A lower level of radio frequency interference is attained with this design since more complete shielding of the high voltage path was incorporated. This permitted increased microcomputer reliability. These modifications have made spark operation at higher gap voltages possible, and a more energetic plasma is generated. Associated with the higher gap voltages are increased spark currents and improved temporal stability of the discharge, this combination produces larger signals and decreased noise. The coaxial capacitor design allows a rapid discharge to occur; hence, the spark can be classified as a high power discharge. The incorporation of a complete, menu-driven, microcomputer software package for data acquisition, coupled with improvements in the reliability of the spark, have made the spark system significantly easier to operate than previous installations. The implementation of the FORTH operating system for data acquisition and control functions has allowed comparatively rapid development of a complex, versatile software package. In addition, the use of FORTH should allow future software to

build on the current software package. Several complex, high speed timing operations were performed by a single, large scale integration, integrated circuit. This device should be seriously considered in any future microprocessor-controlled timing requirements.

Future work on the spark system itself should center on several areas. The spark is a high power discharge; however, due to the short discharge duration, the energy dissipated is only 60 to 100 W. Development of a high energy spark should give more immunity to solvent effects and permit more reliable background level determinations to be made. With the incorporation of thyratron control over the spark production rate, higher gap voltages have been attained; however, the gap voltage is now, in part, determined by the available charging time derived from the firing rate. Efforts to decrease the time constant for the charging cycle should be made to allow capacitor charging to proceed to at least two time constants. This should improve the signal-to-noise ratio. Further work on improving the positional stability of the spark is required, as this appears to be the major source of noise in the signal. Two possible approaches are increasing the firing rate as described by Coleman and Walters (91) or providing an axial argon flow along the electrodes (128). Both of these methods have met with success. The former again requires modification of the charging characteristics to permit adequate performance. The latter may be accomplished through a redesign of the purge gas inlet and flow cell. The current waveform studies have indicated that triggering of the data acquisition electronics from the trigger synchronization pulse is not particularly precise on a spark-to-spark basis at low overpotentials and demonstrates small time lag until spark ignition. This time lag is expected to increase with the age of the thyratron. As such, a return to the use of the photoiode trigger is appropriate.

The spark was found to perform adequately as a capillary GC detector. The interface which was developed worked well and demonstrated no adverse band broadening characteristics. The ability to position the capillary to within 2 mm of the spark was necessary for minimizing the effective dead volume. The capillary GC detection limit for carbon is comparable to the packed column value obtained with previous spark source designs. To improve this, the carbon background signal must be minimized. The use of ultrahigh purity argon would eliminate most of the background; however, a drastic increase in spark operating expenses would be incurred. Replacement of the Teflon flow cell with one of a non-carbonaceous structure would also improve results.

Element-selective chromatographic detection was shown to be a viable means of simplifying component identification. In addition, coupling of chromatographic techniques with element-selective detection can be used to minimize or eliminate time-consuming sample preparation procedures in some cases.

Improvements in the capillary GC/spark detector should focus on ways to increase the quantity of analyte sampled in each spark. Preliminary work with a currently available high-capacity capillary column indicates that sample volumes can be 4 to 10 times greater than those used with the original column. This will cause a corresponding increase in the detectability of individual components. Axial introduction of the effluent instead of the current transverse introduction mode may further increase detection capabilities (107) since the entire gap could be filled with effluent.

Studies with partially desolvated aerosol streams indicate that sufficient energy to desolvate, atomize, and excite many species at low levels is present.

The major problem with this is that too much energy is required to atomize

the large excess of solvent molecules. This effectively cools the spark to an analytically marginal level. More complete desolvation than the miniaturized nebulization/desolvation chamber was capable of producing is necessary for a solution interface to the spark. To attain the goal of an HPLC interface, a very low effective dead volume must be obtained. One promising technique involves an introduction scheme based on isolated droplet generation developed by Hieftje (129). In this technique, a liquid stream is forced through a fine bore capillary. The capillary is physically attached to a bimorph transducer which is electrically oscillated. oscillation imparts a longitudinal wave onto the emerging stream. mechanical perturbation of the stream causes it to break into a series of equally spaced droplets. Once the droplets are formed, no mixing with adjacent drops can occur. Thus, the dead volume is limited to the volume of a single droplet, or a few nanoliters. By electrically charging some of the droplets and applying a voltage across a pair of deflection plates it is possible to remove selected droplets from the stream and reduce the introduction rate.

In this scheme, a single drop could be selected to pass into the gap, and nonselected drops could be deflected to a trap. Synchronization of spark firing to the presence of a droplet would then vaporize, atomize, and excite only the molecules in the droplet. Since a droplet pulsing rate of approximately 20 kHz is common, 90% of the solvent and analyte are immediately eliminated. Additional desolvation steps could further minimize the amount of solvent reaching the spark. In preliminary work by Wiegand (130), individual droplets were successfully passed through the spark gap. This droplet generation may prove to be the long-sought HPLC interface.

The present detector is limited in practicality since only a single emission

at a time can be acquired. Implementation of an optical multichannel analyser (OMA) on the spark system would vastly improve the throughput of multielement detection. Rapid gating of the detector is necessary to reduce the background continuum. This criterion is met by the Princeton Applied Research OMA III (131).

KEKEKENCES

- Grimmer, G; Jacob, J.; Manjack, K. Anal. Chem. 1983, 55, 2398-2404.
- Lantz, R.K. Ph.D. Thesis, Michigan State University: East Lansing,
- **1261** IW
- Koeplin, S.M. Ph.D. Thesis, Michigan State University: East Lansing,
- 8261 IM
- Calkin, C.L. Ph.D. Thesis, Michigan State University: East Lansing,
- .1861 IM
- Cremer, E.; Krans, T.; Bechtold, E. Chem. Ing. Tech. 1961, 33, 632.
- Cremer, E. J. Gas Chrom. 1967, 5, 329. .9
- Sevcik, J. Chromatographia 1973, 6, 139-148.
- Guiffrida, L.; Ives, N.F.; Bostwick, D.C. JAOKC 1966, 49, 8. .8
- Hoodless, R.A.; Sargent, M.; Trible, R. J. Chrom. 1977, 136, 199. •6
- Hartman, C.H. J. Chrom. Sci. 1969, 7, 163. 10.
- Aue, W.A.; Gehrke, C.W.; Tindle, L.C.; Stolling, D.L.; Ruyle, C.D.
- Lubkowitz, J.; Glajck, J.; Semonian, B.; Rogers, C. J. Chrom. 1977, J. Gas Chrom. 1967, 5, 381.
- Dressler, M.; Janak, J. J. Chrom. Sci. 1969, 7, 451.
- Karnen, A.; Kelly, E.L. Anal. Chem. 1971, 43, 1992.
- Kolb, B.; Bischoff, J. J. Chrom. Sci. 1974, 12, 625.
- Patterson, E.L.; Gatten, R.A.; Ontieros, C. J. Chrom. Sci. 1982, 20,

97-102.

.78, 881

- 17. Bombick, D.; Pinkston, J.D.; Allison, J. Anal. Chem. 1984, 56, 396-402.
- 18. Aue, W. J. Chrom. Sci. 1975, 13, 329.
- 19. Versino, B.; Vissers, H. Chromatographia 1975, 8, 5.
- 20. Getty, R.H.; Birks, J.W. Anal. Lett. 1979, 12, 469-476.
- 21. Aue, W.; Flinn, C.G. J. Chrom. 1972, 142, 145.
- 22. Jackson, J.A.; Blair, W.R.; Brinckman, F.E.; Iverson, W. P. <u>Envir.</u> Sci. Techn. **1982**, 16(2), 110-159.
- 23. Sutton, D.L.; Westberg, K.R.; Melger, J.E. Anal. Chem. 1979, 51, 1399-1401.
- 24. Burnett, C.H.; Adams, C.F.; Farwell, S.O. <u>J. Chrom. Sci.</u> 1978, 16, 68-73.
- 25. Kelly, T.J.; Gaffney, J.S.; Phillips, M.F.; Janner, R.L. Anal. Chem. 1983, 55, 135-138.
- 26. Nelson, J.K.; Getty, R.H.; Birks, J.W. Anal. Chem. 1983, 55, 1767-1770.
- 27. Yamada, M.; Ishiwada, A.; Hobo, T.; Suzuki, S.; Araki, S. <u>J. Chrom.</u>
 1982, 238, 347-356.
- 28. Patterson, P.; Howe, R.; Abu-Shumays, A Anal. Chem. 1978, 50, 339.
- Karasek, F.W.; Onaska, F.I.; Yang, F.J.; Clement, R.E. <u>Anal. Chem.</u>
 1984, 56, 174R-199R.
- 30. Corkill, J.A.; Joppich, M.; Kuttalo, S.H.; Giese, R.W. <u>Anal. Chem.</u>
 1982, 54, 481-485.
- 31. McNair, H.M.; Bonelli, E.J. "Basic Gas Chromatography", Varian Instruments: Berkeley, CA, 1969; p. 118.
- 32. Karasek, F.W.; Field, L.R. Res/Dev 1977, 42.
- 33. Aue, W.A.; Siu, K.W.M. J. Chrom. 1982, 239, 127-144.
- 34. Sullivan, J.J.; Burgett, L.A. Chromatographia 1975, 8, 176.

- 35. Grimsrud, E.P.; Knighton, W.B. Anal. Chem. 1982, 54, 565-570.
- 36. Parris, G.; Blair, W.; Brinckman, F. Anal. Chem. 1977, 49, 378.
- 37. Seger, D. Anal. Lett. 1974, 7, 89.
- 38. Andree, M.O. Anal. Chem. 1977, 49, 820.
- 39. Wolf, W. J. Chrom. 1977, 134, 159.
- 40. Dumarey, R.; Dens, R.; Sandra, P. <u>J. High Resolut. Chrom.</u> 1982, 5, 687-689.
- 41. Chau, Y.K.; Wong, P.T.S.; Saitoh, H. J. Chrom. Sci. 1977, 14.
- 42. Wolf, W.R. Anal. Chem. 1976, 48, 1717.
- 43. Harnly, J.M.; O'Haver, T.C.; Golden, B.; Wolf, W. Anal. Chem. 1979, 51, 2007.
- 44. Harnly, J.M.; Patterson, K.Y.; Wolf, W.R.; O'Haver, T.C. Anal. Chem. 1983, 55, 1417.
- 45. Eckhoff, M.A.; McCarthy, J.P.; Caruso, J.A. Anal. Chem. 1982, 54, 165-168.
- 46. Risby, T.H.; Talmi, Y. <u>CRC Crit. Rev. Anal. Chem.</u> 1983, 14(3), 231-265.
- 47. Chau, Y.K.; Wong, P.T.S.; Bengert, G.A. Anal. Chem. 1982, 54, 246.
- 48. Robinson, J.W.; Kiesel, E.L.; Bliss, R. Anal. Chim. Acta 1977, 92, 321.
- 49. Yamagisawa, M.; Suzuki, H.; Kitigawa, K.; Tange, S. <u>Spectrochim.</u>
 Acta Part B 1983, 38, 1143-1149.
- 50. McCormack, A.J.; Tong, S.C.; Cooke, W.D. Anal. Chem. 1965, 37, 1470.
- 51. Qing-Yu, O.; Guo-Chuen, W.; Ke-Wei, Z.; Wei-Lu, Y. Spectrochim.

 Acta Part B 1983, 38, 419-425.
- 52. Fehsenfeld, F.C.; Evenson, K.M.; Broida, H.P. <u>Rev. Sci. Instr.</u> 1965, 36, 294.

- 53. Greenfield, S.; McGeachin, H.; Smith, P.B. Talanta 1975, 22, 553.
- 54. Van Dalen, J.; Sezenne-Coulancki, A.; Galan, L. Anal. Chim. Acta 1977, 94, 1.
- 55. Serravallo, F.; Risby, T. Anal. Chem. 1975, 47, 2141.
- 56. Beenaker, C.I.M. Spectrochim. Acta Part B 1976, 31, 483.
- 57. Beenaker, C.I.M. Spectrochim. Acta Part B 1977, 32, 173.
- 58. Beenaker, C.I.M. Spectrochim. Acta Part B 1978, 33, 53.
- 59. Reamer, D.C.; Zoeller, W.H.; O'Haver, T.C. Anal. Chem. 1978, 50, 1449.
- 60. Quimby, B.D.; Delaney, M.F.; Uden, P.C.; Barnes, R.M. Anal. Chem., 1979, 51, 875.
- 61. Carnahan, J.A.; Mulligan, K.J.; Caruso, J.A. Anal. Chim. Acta 1981, 130, 227.
- 62. Mulligan, K.J.; Zerezhgi, M.; Caruso, J.A. Spectrochim. Acta Part B 1983, 38, 369-375.
- 63. Tanabe, K.; Haraguchi, H.; Fuwa, K. Spectrochim. Acta Part B 1981, 36, 633-639.
- 64. Uden, P.C.; Barnes, R.M.; Des Sanzo, F. Anal. Chem. 1978, 50, 852-855.
- 65. Lloyd, R.J.; Barnes, R.M.; Uden, P.C.; Elliot, W.G. Anal. Chem. 1978, 50, 2025-2029.
- 66. Quimby, B.D.; Uden, P.C.; Barnes, R.M. Anal. Chem. 1978, 50, 2112-2118.
- 67. Windsor, D.L.; Denton, M.P. Appl. Spectros. 1978, 32, 366-371.
- 68. Zerezghi, M.; Mulligan, K.J.; Caruso, J.A. <u>J. Chrom. Sci.</u> 1984, 22, 348-352.
- 69. Morita, M.; Uehiro, T.; Fuwa, K. Anal. Chem. 1980, 52, 349-351.
- 70. Hausler, D.W.; Taylor, L.T. Anal. Chem. 1981, 53, 1223-1227.

- 71. Eckhoff, M.A.; Ridgway, T.H.; Caruso, J.A. Anal. Chem. 1983, 55, 1004-1009.
- 72. Estes, S.A.; Uden, P.C.; Barnes, R.M. Anal. Chem. 1981, 53, 1829.
- 73. Holland, J.F.; Enke, C.G.; Allison, J.A.; Stults, J.T.; Pinkston, J.D.; Newcome, B.; Watson, J.T. Anal. Chem. 1983, 55, 997A.
- 74. Steiglitz, L.; Zwick, G. Anal. Org. Micropollut. Water 1982, 105, 112.
- 75. Uden, P.C.; Bigley, I.E. Anal. Chim. Acta 1977, 94, 29.
- 76. Decker, R.J. Spectrochim. Acta Part B 1980, 35, 19.
- 77. McLean, W.R.; Stanton, D.L.; Penketh, G.G. Analyst 1973, 98, 432.
- 78. Brenner, K.S. J. Chrom. 1978, 167, 365.
- 79. Dingham, H.P.; DeJong, H.J. <u>Spectrochim. Acta Part B</u> 1981, 36, 325.
- 80. Van Loon, J.C. Can. J. Spectros. 1981, 26(4), 22A-32A.
- 81. Fraley, D.M.: Yates, D.A.; Manahan, S.E. App. Spectros. 1981, 35, 525.
- 82. Irgolic, K.J.; Stockton, R.A.; Chakraborti, D.; Beyer, W. Spectrochim.

 Acta Part B 1983, 437-445.
- 83. Brown, R.M.; Fry, R.C. Anal. Chem. 1981, 53, 532-538.
- 84. Brown, R.M.; Northway, S.J.; Fry, R.C. Anal. Chem. 1981, 53, 934-936.
- 85. Sommer, D.; Ohls, K. Z. Anal. Chem. 1979, 295, 337.
- 86. Hughes, S.K.; Fry, R.C. Anal. Chem. 1983, 53, 1111.
- 87. Sinclair, D.A.; Whitten, R.N. Spectrochim. Acta 1960, 16, 760.
- 88. Nakajima, T.; Kawaguchi, H. Spectrochim. Acta 1962, 18, 201.
- 89. Walters, J.P. Anal. Chem. 1968, 40, 1540.
- 90. "Ceramic Metal Grounded Grid Thyratrons Data Sheet H5003C-1", EG&G Electro-Optics: Salem, MA 1977.

- 91. Coleman, D.M.; Walters, J.P. Spectrochim. Acta Part B 1976, 31, 547-587.
- 92. Black, M.S.; Browner, R.F. Anal. Chem. 1981, 53, 249.
- 93. "Ultrasonic Nebulizing System Model UNS-1", Plasmatherm: Kresson, NJ 1979.
- 94. Donahue, D.L.; Carter, J.A. Anal. Chem. 1978, 50, 686.
- 95. "Gas Chromatography Catalog #6", Ansepc Co.: Ann Arbor, MI 1983, pp. 26,44.
- 96. "Insulation and Operation Instructions for On-Column Injector", SGE
 Co.: Austin, TX 1980.
- 97. Newcome, B.H. "Ph.D. Thesis", Michigan State University: East Lansing, MI 1983.
- 98. "Floppy Disk Drive FDD 100-8 Technical Manual", Siemens Inc.:
 Anaheim, CA 1980; pp. 1-1, 1-16.
- 99. "Technical Data for AD574 A/D Converter", Analog Devices Inc.:
 Norwood, MA 1981.
- 100. "700 Systems Instruction Manual Model EU-700-32 Controller", GCA/McPherson Inc.: Acton, MA 1975, pp. 7-10, 7-24.
- 101. Gregg, H.L. Ph.D. research in progress, East Lansing, MI 1984.
- 102. Brodie, L. "Starting FORTH", Prentice-Hall Inc.: Englewood Cliffs, NJ 1981.
- 103. Atkinson, T.V.; Gregg, H.L. "MULPLT: A Multiple Data Set, File-Based Data Plotting Program", East Lansing, MI 1982.
- 104. Walters, J.P.; Coleman, D.M. <u>Spectrochim. Acta Part B</u> 1976, 31, 547.
- 105. Nasser, E. "Fundamentals of Gaseous Ionization and Plasma Electronics", Wiley & Sons., Inc.: New York, NY 1971, pp. 219-297.

- 106. Zynger, J. "Ph.D. Thesis", Michigan State University: East Lansing, MI 1973.
- 107. Seng, G.T. "Ph.D. Thesis", Michigan State University, East Lansing, MI 1978.
- 108. "General Catalog 92", Scientific Gas Products, Inc.: South Plainsfield, NJ 1983, p. 7.
- 109. Pearse, R.W.B.; Gaydon, A.G. "The Identification of Molecular Spectra 4th Ed.", Wiley & Sons: New York, NY 1976.
- 110. Rief, I.; Fassel, V.A.; Kniseley, R.N. Spectrochim. Acta Part B 1973, 28, 105.
- 111. Knopp, C.F.; Gottschlich, C.F.; Cambel, A.B. <u>J. Quant. Spectry.</u>
 Radiative Transfer 1962, 2, 297.
- 112. Tourin, R.H. J. Quant. Spectry. Radiative Transfer 1963, 3, 89.
- 113. Wiese, W.L.; Smith, M.W.; Miles, B.M. "Atomic Transition Probabilities",U.S. Government Printing Office: Washington, DC 1969.
- 114. Taylor, H.E.; Gibson, J.H.; Skogerboe, R.K. Anal. Chem. 1970, 42, 1569.
- 115. Fallgatter, K.; Svoboda, V.; Winefordner, J.D. Appl. Spectrosc. 1971, 25, 347.
- 116. Griem, H.R. "Plasma Spectroscopy", McGraw-Hill: New York, NY 1964.
- 117. Kolb, A.C.; Griem, H.R. Phys. Rev. 1958, 111, 514.
- 118. Malone, B.S.; Corcoran, W.H. J. Quant. Spectry. Radiative Transfer 1966, 6, 443.
- 119. Boumans, P.W.J.M. "Theory of Spectrochemical Excitation", Plenum Press: New York, NY 1966.

- 120. Corliss, C.H.; Bozman, W.R. "Experimental Transition Probabilities for Spectral Lines of Seventy Elements, NBS. Monograph 53", U.S. Government Printing Office: Washington, DC 1962.
- 121. Zaidel', A.N.; Prokof'ev, V.K.; Raiskii, S.M.; Slavnyi, V.A.; Shreider, E.Y. "Tables of Spectral Lines", Plenum Press: New York, NY 1970.
- 122. Kirkland, J.J.; Snyder, L.R. "Introduction to Modern Liquid Chromatography, 2nd Ed.", Wiley & Sons: New York, NY 1979, pp. 34-36.
- 123. "Annual Book of ASTM Standards", Am. Soc. For Testing Materials: Philadelphia, PA 1973, p. D3237.
- 124. Scott, D.R.; Holboke, L.E.; Hadeishi, T. Anal. Chem. 1983, 55, 2006.
- 125. "Certificate of Analysis for Standard Reference Material Lead in Reference Fuel", U.S. Dept. of Commerce, NBS: Washington, DC 1980.
- 126. Koizumi, H.; McLaughlin, R.D.; Hadeishi, T. Anal. Chem. 1979, 51, 387.
- 127. Ng, K.C.; Caurso, J.A. Anal. Chem. 1983, 55, 2032.
- 128. Walters, J.P.; Goldstein, S.A. "ASTM Special Technical Publication # 540", Am. Soc. For Testing Material: Philadelphia, PA 1973.
- 129. Hieftje, G.M.; Malmstadt, H.V. Anal. Chem. 1968, 40, 1860-1867.
- 130. Wiegand, P.M. Ph.D. research in progress, East Lansing, MI 1984.
- 131. "Optical Multichannel Averager III Technical Bulletin", Princeton Applied Research: Princeton, NJ 1984.